Solenoidal Fields for Ion Beam Transport and Focusing

Edward Lee and Matthaeus Leitner
Lawrence Berkeley National Laboratory
November 2007

1. Introduction and Contents

In this report we calculate time-independent fields of solenoidal magnets that are suitable for ion beam transport and focusing.

Electricity and Magnetism Textbooks present the formalism for magnetic field calculations and apply it to simple geometries [1-1], but they do not include enough relevant detail to be very useful for designing a charged particle transport system. This requires accurate estimates of fringe field aberrations, misaligned and tilted fields, peak fields in coils and iron, external fields, and more. Specialized books on magnet design, technology, and numerical computations [1-2] contain relevant detail of this type, and some of that is presented here. The AIP Conference Proceedings of the US Particle Accelerator Schools [1-3] contain extensive discussions of design and technology of magnets for ion beams – except for solenoids. This lack may be due to the fact that solenoids have been used primarily to transport and focus particles of relatively low momentum, e.g. electrons of less than 50 MeV and protons or H^- of less than 1.0 MeV, although this situation may be changing with the commercial availability of superconducting solenoids with up to 20T bore field [1-4]. Internal reports from federal laboratories and industry treat solenoid design in detail for specific applications. The present report is intended to be a resource for the design of ion beam drivers for Inertial Fusion Energy [1-5] and Warm Dense Matter experiments [1-6], although it should also be useful for a wider range of applications.

The field produced by specified currents and magnetized materials can always be evaluated by solving Maxwell's equations numerically, but it is also desirable to have reasonably accurate, simple formulas for system design and fast-running beam dynamics codes, as well as for general understanding. Most of this report is devoted to such formulas, but an introduction to the Tosca© code [1-7] and some numerical results obtained with it are also presented. Details of design, fabrication, installation, and operation of real magnet systems are not included. Mathematical derivations are presented with a moderate amount of detail. While there is no claim of originality, except for various numerical approximations and an induction module design in section 20, many of the results and discussions are hard to find elsewhere.

Our primary topic is axisymmetric solenoidal systems with no magnetic materials. These simplifying features allow useful analytical calculations, which occupy sections 2-13. Deviations from axisymmetry are considered in sections 14, 15, 21, and 22, and the effects of magnetic materials are treated in sections 16-20. Since magnetic aberrations are mixed with geometric aberrations in computing ion orbits, section 22 on the ion equations of motion is included.

Contents

1. Introduction and Contents
2. Solenoid Basics
    - 2.1 Model assumptions and equations
    - 2.2 Simple field estimate
    - 2.3 Current layers, global picture, and moments
    - 2.4 Vector potential and flux lines
    - 2.5 Stress and energy
3. Near-Axis Field
    - 3.1 On-axis field and near-axis expansion
    - 3.2 Useful integrals
4. Design Formulas for the On-Axis Field
    - 4.1 Simple cases
    - 4.2 Thick wire layer
    - 4.3 Uniform fields
5. Vector and Scalar Potentials
    - 5.1 Vector potential
    - 5.2 Scalar potential
    - 5.3 Global scalar potential
6. Green Function Solutions
    - 6.1 Green function formalism
    - 6.2 Explicit field expressions
7. Approximation of Green Function Integrals
8. Thin Wire Layer
    - 8.1 Semi-infinite layer
    - 8.2 Wire end divergence
    - 8.3 Finite length lens
    - 8.4 Stored energy
9. Thick Wire Layer
    - 9.1 Uniform thick layer
    - 9.2 Approximation by a thin layer
    - 9.3 General thick layer
10. Periodic Thin Wire Layer
11. Far Field and External Field
    - 11.1 Far field expansion
    - 11.2 External field expansion
12. Field in the Wire Layer
13. Current to Produce a Given Field
14. Misaligned and Tilted Solenoid
15. Multiple Channels – Cross Talk

16. Magnetic Materials Basics
    - 16.1 Ferromagnetism
    - 16.2 Magnetization formalism
    - 16.3 B-H relations and jump conditions
    - 16.4 Magnetization curve
    - 16.5 Permanent magnet solenoid
17. Wire Layer Embedded in a Highly Permeable Yoke
18. Periodic Thin Wire Layer with a Highly Permeable Yoke
19. Tosca© Model
    - 19.1 General solution strategy in 3D
    - 19.2 Solution strategy in 2D
    - 19.3 Example
20. Application of Tosca© to Induction Linac Design
21. Biot-Savart Formula
    - 21.1 General formula
    - 21.2 Straight wire segment field
    - 21.3 Helix field
22. Single Particle Equations of Motion in an Arbitrary field
    - 22.1 Time as the independent variable
    - 22.2 Longitudinal distance as the independent variable
    - 22.3 Paraxial approximation

References

1-1 Jackson, J.D., Classical Electrodynamics. 2nd or 3rd Edition, Wiley, New York, (1975 or 1999), chap.5.

Feyman, R., Leighton, R., and Sands, M., The Feyman Lectures on Physics, Vol. II, Chs. 13, 14, 15, 36, 37, Addison – Wesley, 1962.

Panofsky, W.K.H., and Phillips, M., Classical Electricity and Magnetism, 2nd edition, Addison-Wesley, Reading, Mass. (1962), chaps. 7 & 8.

Smythe, W.R., Static and Dynamical Electricity, 3rd edition, McGraw-Hill, New York (1969), chap. 7.

1-2 Wilson, M.N., Superconducting Magnets, Clarendon Press, Oxford (1983).

1-3 Magnet calculations are presented in many volumes of the AIP Proceedings for The US Particle Accelerator Schools (http://uspas.fnal.gov); one example is:

Willen, E., Dahl, P. and Herrera, J., Superconducting Magnets, AIP Conference Proceedings 153, pg 1228, American Institute of Physics, New York (1987).

1-4 For example: American Magnetics, Inc., 112 Flint Rd., Oakridge, TN 37831, www.americanmagnetics.com

1-5 Lee, E., Solenoidal Transport for Heavy Ion Fusion, Nuclear Instruments and Methods in Physics Research, Volume 544, Issues 1-2, 2005, 187.

1-6 Barnard, J.J., et al., Accelerator and Ion Beam Tradeoffs for Studies of Warm Dense Matter, Proceedings of the 2005 Particle Accelerator Conference, Knoxville TN, 05/16-20/2005.

1-7 Tosca© is commercially available. Contact: Vector Fields Inc., 1700 N. Farnsworth Avenue, Aurora, IL 60505, USA, http://www.vectorfields.com.

Another code widely used for magnet computations is Poisson Superfish, which is available from the Los Alamos Accelerator code group:

Halback, K. and Holsinger, R.F. "SUPERFISH-A Computer Program for Evaluation of RF Cavities with Cylindrical Symmetry", Particle Accelerators, 7 213 (1976), and "Poisson Superfish Documentation" by James H. Billen and Lloyd M. Young, Los Alamos National Laboratory Report # LA-UR-96-1834. The software can be downloaded at http://laacg1.lanl.gov.

Acknowledgements

The authors thank Ms. Lynn Heimbucher for her great effort and patience over several years in shepherding this report through its many revisions. Helpful discussions were held with Shlomo Caspi, Andy Faltens, Alex Friedman, Enrique Henestroza, Steven Lund, and William Waldron.

This work was supported by the Director, Office of Science, and Office of Fusion Energy Sciences, of the U.S. Department of Energy under Contract No. DE-AC02-05CH11231.

2. Solenoid Basics

2.1 Model assumptions and equations

We wish to calculate the field of a system of solenoidal magnets suitable for the transport and focusing of ion beams. Generally such a field will be very strong, in the range 2-20 T in the magnet bore and current-carrying wire. In this report we treat fields that are constant in time and have strict solenoidal symmetry around the z-axis (except in sections 14, 15, 21 and 22). Cylindrical coordinates (r,θ,z) are used for the general position vector $\vec{r}$ unless indicated otherwise. The only component of wire current density is then $J_\theta(r,z)$, which is the source of the two field components $B_r(r,z)$ and $B_z(r,z)$. This is true even when magnetic materials are present since they have only a current density $J_\theta^{mag}(r,z)$ equal to the curl of the magnetization density ($M_r(r,z)$, $M_z(r,z)$). Axisymmetric induction cores, with idealized current and field components $(J_r, J_z, B_\theta, M_\theta)$, are therefore not treated here.

In general the magnetization density is not independent of wire current except for the case of stiff permanent magnet material; this feature (permeability) greatly increases the complexity of the analysis and makes it necessary to use codes such as Poisson and Tosca© [1-7] in all but the simplest situations. Consideration of magnetic material properties is delayed until section 16. In the absence of permeable magnetic materials, solenoid fields may be treated analytically or with elementary codes.

Wire leads and windings are assumed to be paired such that field aberrations due to deviations from solenoidal symmetry are cancelled down to a negligible level. This includes cancellation of the small z component of current that is present in a single (helical) coil of wire by returning the current in a second coil on top of it. Also, the small-scale variations of field inside and close to individual wire or cable sections are ignored, i.e. a smoothed model for $J_\theta(r,z)$ is adopted. In effect, the dominant, collective field from the current density is calculated here, without any distinction between wire and cable, and the small-scale variations are left to detailed magnet computations. However, one must be careful when representing the actual currents by a smoothed $J_\theta(r,z)$. For example the effective length and dipole moment of a magnet (see eqns. 2.11-2.14) should be incorporated into the smoothed model.

SI units (Tesla, Ampere, meter) are used throughout this report. The relevant Maxwell's equations in the absence of magnetic materials are

$$\vec{\nabla} x \vec{B} = \mu_0 \vec{J}, \qquad \vec{\nabla} \cdot \vec{B} = 0, \tag{2.1a,b}$$

where $\mu_0 = 4\pi x 10^{-7} T-m/A$. To convert any equation to Gaussian (cgs) form, substitute $\mu_0 \to 4\pi/c$. Unit conversion factors are 1.0 Tesla=10^4 Gauss, 1.0 Ampere = 2.99792…$x10^9$ statampere, and 1.0m=10^2 cm.

Since the variable r denotes distance from the z-axis, $|\vec{r}| = \sqrt{r^2 + z^2}$ is the distance from the coordinate origin. Assuming solenoidal symmetry, eqns. (2.1 a,b) become

$$\frac{\partial B_r}{\partial \mathrm{z}} - \frac{\partial B_\mathrm{z}}{\partial r} = \mu_0 J_\theta , \quad \frac{1}{r}\frac{\partial}{\partial r} r B_r + \frac{\partial B_\mathrm{z}}{\partial \mathrm{z}} = 0 . \tag{2.2a,b}$$

From these coupled first-order equations one can derive the decoupled second-order equations:

$$\frac{1}{r}\frac{\partial}{\partial r} r \frac{\partial B_\mathrm{z}}{\partial r} + \frac{\partial^2 B_\mathrm{z}}{\partial \mathrm{z}^2} = -\mu_0 \frac{1}{r}\frac{\partial}{\partial r} r J_\theta , \tag{2.3a}$$

$$\frac{\partial}{\partial r}\frac{1}{r}\frac{\partial}{\partial r} r B_r + \frac{\partial^2 B_r}{\partial \mathrm{z}^2} = \mu_0 \frac{\partial J_\theta}{\partial \mathrm{z}} . \tag{2.3b}$$

The operator acting on B_z in eqns. (2.3a,b) is the scalar Laplacian in cylindrical coordinates with $\partial/\partial\theta = 0$, while the operator acting on B_r is not quite of this standard form. In general the field equations can be solved using the Green function for the Laplacian operator. This may seem unnecessarily complicated since integrations are over all three spatial variables $(\mathrm{r}, \theta, \mathrm{z})$ to obtain functions of only the two variables (r,z). However for the case of greatest interest, the thin wire layer, integrations can be easily reduced to the single variable θ, and the analysis is not much more complicated than the textbook case of a single wire loop. It may seem simpler to use the Biot-Savart formula (also a Green function solution), which yields $\vec{B}$ from a single integration along the wire path - see section 21, but this is somewhat misleading because the path may be very long and must be specified by a more complicated formula than is used for the smoothed J_θ (r,z). On the other hand, the Biot-Savart formula gives fine-scale detail of the field around the wire that is missed by the Green function approach using smoothed sources, and is therefore useful for detailed design. We also employ Fourier and Bessel series and transformations, several types of magnetic potential, and for really complicated cases a finite element code.

If cartesian components and coordinates are used then eqns. (2.3 a,b) are replaced by the compact vector form

$$\nabla^2 \vec{B} = -\mu_0 \vec{\nabla} x \vec{J} , \tag{2.3c}$$

which can be immediately integrated using the Green function for the Laplacian operator. It is then necessary to project B_r from $\vec{B}$; this is only a minor complication, and is essentially equivalent to the direct solution of eqn. (2.3b) given in section 6.

2.2 Simple field estimate

Generally we assume $J_\theta = 0$ at large $|\vec{r}|$. However, to make a rough estimate of field strength we examine the infinite, uniform, thin-current layer carrying S Amperes/m:

$$J_\theta(r,z) = S\delta(r-R) \qquad \text{all z,} \tag{2.4}$$

where $\delta(x)$ is the Dirac delta function. Eqns. (2.2 a,b) then give

$$B_z = \mu_0 SH(R-r), \qquad B_r = 0. \tag{2.5a,b}$$

Here H(x) denotes a positive unit step at x=0, with dH(x)/dx = $\delta(x)$:

$$H(x) = \begin{cases} 1, & x > 0, \\ 0, & x < 0. \end{cases}$$

For a bore field of 1.0T we need

$$S = \frac{B_z}{\mu_0} = \frac{1.0}{4\pi x 10^{-7}} = 795.8\frac{kA}{m}. \tag{2.6}$$

In round numbers S=.80 MA/m for 1.0T (or 800 A/cm for 1.0 kG) for a long magnet, but S must be somewhat higher for short magnets. Superconducting wire or cable can carry very high current densities at high fields, so a high field magnet can be made with a relatively thin current layer. Examples of "engineering-averaged critical current density" (see section 20) are:

critical fields and current density at 4.2K

superconductor	wire field	peak J
Nb - Ti	6.0T	$5x10^8$ A/m^2
Nb_3Sn	10.0T	$7.5x10^8$ A/m^2
Nb_3Sn	15.0T	$4.8x10^8$ A/m^2

These current densities take into account space for Cu stabilizer, insulation, and small gaps as well as actual superconductor. They are lower than the critical current densities for the pure superconductor by factors of 3 -10. For example, a bore field of 10.0T may

require $S \approx 10$MA/m, which can be made (in principle) using Nb_3Sn with current layer thickness $= S/J = 10^7/7.5x10^8 = .0133$m. When the radial distance from the magnet axis out to the superconducting wire is greater than a few times the total layer thickness, we can model the current density as an annulus of infinitesimal thickness for the purpose of computing the field in the magnet bore. However, high field solenoids, especially those using normal conductor, often have total current layer thickness comparable to the bore radius or greater. This more complicated geometry is analyzed in section 9.

2.3 Current layers, global picture, and moments

For a current layer of finite thickness it is useful to define the cumulative current layer density

$$S(r,z) \equiv \int_r^\infty dr' J_\theta(r',z), \tag{2.7}$$

with net current layer density $S(z) = S(r=0,z)$. If S(r,z) varys slowly with z then eqns. (2.2a,b) suggest the approximate solution

$$B_z \approx \mu_0 S(r,z), \tag{2.8a}$$

$$B_r \approx -\frac{\mu_0}{r}\int_0^r dr' r' \frac{\partial S(r',z)}{\partial z}. \tag{2.8b}$$

However, most solenoids have abrupt wire layer ends, so eqns. (2.8a,b) give only a rough approximation inside the magnet bore and wire, and they are completely incorrect at large r. Sections 3-12 are devoted to obtaining accurate formulas for all ranges of (r,z).

To avoid confusion over notation we mention here that the symbol S, which denotes current layer density and is always a radial integration of J_θ, appears in four related forms depending on context: a simple scale value S, the cumulative density $S(r,z)$, the net value $S(z)$, and the cumulative density $S(r)$ which is present when $S(r,z)$ is uniform in z between specified magnet layer ends. Simple solenoids composed of uniform thick or thin layers produce fields which are suitable for beam transport. However, there are some applications that require a more complicated layer function $S(r,z)$ within a single magnet, for example to create a very uniform bore field. Such cases can usually be constructed by superimposing the fields of several simple layers. The symbol I denotes either current in a wire or total azimuthal current in a magnet, depending on context. In the latter case $I = \int dz\ S(z)$.

Since $\vec{\nabla}\cdot\vec{B} = 0$ and $\vec{B}$ vanishes at large $|\vec{r}|$ (at least as fast as $|\vec{r}|^{-3}$), there must be a "return flux". The total flux through any plane with fixed coordinate z is

$$\int_0^\infty dr 2\pi r B_z(r,z) = 0. \tag{2.9}$$

All flux lines form closed loops at fixed values of θ. For a very long system the far field (i.e. the field at large $|\vec{r}|$ greater than the system length) gets mixed up with the Earth's field or the fields from other sources, so the concept of return flux is actually somewhat ambiguous. However, the external field produced close to the magnet system, usually with the sign of B_z reversed from the adjacent bore field, is of great interest – see the figure below. For example, it may interfere with the functioning of induction cores in a linac or with nearby instrumentation. This topic is treated in several sections – especially section 11.

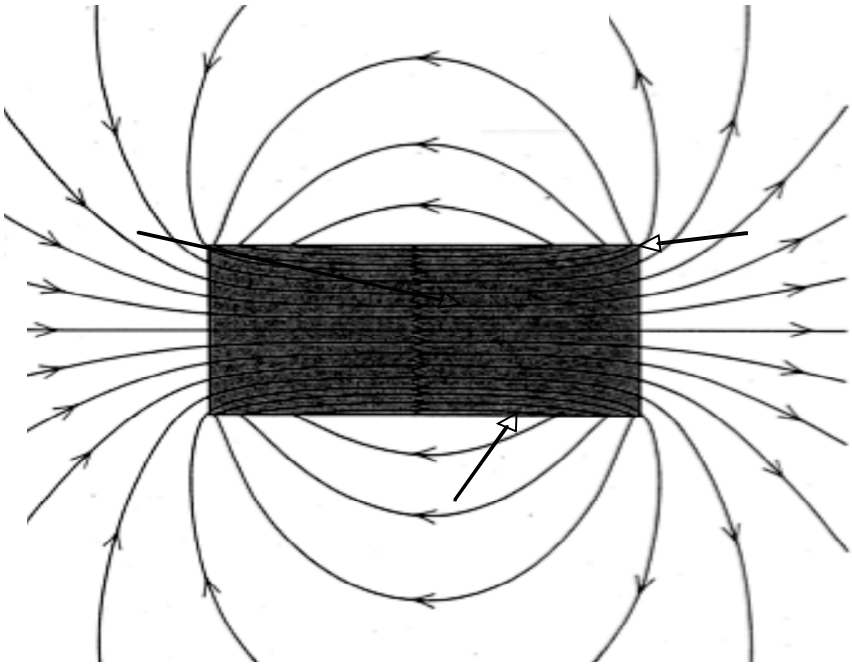

One rather expensive way to reduce or eliminate the far field is to place an additional current layer with reverse polarity at larger radius than the primary layer. For example a very long thin current layer of density S placed at radius R can be surrounded by a second layer of density $-S/4$ at $2R$, resulting in zero net flux in the region $r < 2R$. This causes a reduction of the bore field to $.75\ \mu_0 S$. A permeable annular yoke can also be used to confine the return flux and reduce the external field, without any reduction of the bore field – see section 18.

For visualizing and calculating the field outside the magnet bore it is useful to define "direct" and "residual" fields:

$$\vec{B}^{\text{direct}} \equiv \mu_0 S(r,z)\hat{e}_z, \tag{2.10a}$$

$$\vec{B}^{\text{residual}} \equiv \vec{B} - \vec{B}^{\text{direct}}. \tag{2.10b}$$

A "direct flux" is defined as

$$F^{direct}(z) = \int_0^\infty dr 2\pi r \mu_0 S(r,z) = \int_0^\infty dr \pi r^2 \mu_0 J_\theta(r,z), \tag{2.11}$$

where we integrated by parts to obtain the last expression.

A single loop of wire of radius R and carrying azimuthal current I has magnetic dipole moment $\pi R^2 I$. Magnetic moments add for a system with solenoidal symmetry, so we have for the system's total magnetic dipole moment m_1:

$$\begin{aligned} m_1 &= \int_{-\infty}^{+\infty} dz \int_0^\infty dr \pi r^2 J_\theta = \int_{-\infty}^{+\infty} dz \frac{F^{direct}(z)}{\mu_0} \\ &= 2\pi \int_{-\infty}^{+\infty} dz \int_0^\infty dr r S(r,z) \quad . \end{aligned} \tag{2.12}$$

Assuming m_1 is non-zero, the field at very large $|\vec{r}|$, i.e. the far field (see section 11), is

$$B_r = \frac{\mu_0 m_1}{4\pi} \frac{3rz}{\sqrt{r^2+z^2}^5}, \tag{2.13a}$$

$$B_z = \frac{\mu_0 m_1}{4\pi} \frac{2z^2 - r^2}{\sqrt{r^2+z^2}^5} \quad . \tag{2.13b}$$

Higher order moments, which generate field components that fall off more rapidly with $|\vec{r}|$, are also present. The coordinate origin can usually be positioned such that the magnetic quadrupole moment $\left(m_2 \sim \int dz \int dr r^2 z J_\theta\right)$ vanishes, but higher moments are always present.

So far we have made use of two radial moments of J_θ:

$$S(z) = \int_0^\infty dr \;\; J_\theta(r,z), \tag{2.14a}$$

$$S(z)\overline{r^2}(z) = \int_0^\infty dr \;\; r^2 J_\theta(r,z) = 2\int_0^\infty dr r \;\; S(r,z) \; . \tag{2.14b}$$

Additional radial moments weighted by J_θ such as $S\overline{r^4}, S\overline{r^6}$, … will be used in section (11) to evaluate the external field. Note that $\overline{r^2}$, $\overline{r^4}$, etc. can actually be negative if J_θ reverses sign as a function of r, so they are not true mean values.

As mentioned, care is needed when representing a magnet by a smooth current distribution. Consider a simple wire coil of n turns at radius R with center-to-center longitudinal spacing δ. If the wire current is I then the net azimuthal current is nI and the net magnetic moment is $m_1 = \pi R^2 nI$. However, the effective coil length is $\ell = n\delta$, not $(n-1)\delta$, since each loop would be centered in a strip of length δ for an accurate finite element calculation. The correct current layer density is $S = nI/\ell = I/\delta$, which is consistent with the value $m_1 = \ell\pi R^2 S$ obtained from eqn. (2.12). The physical length of the coil alone, taking into account that it is actually a helix, is also ℓ (plus one wire thickness). The longitudinal current of the coil is I, which would be the source of an azimuthal field for $r > R$. However, this is assumed to be cancelled by a second coil at slightly larger radius.

2.4 Vector potential and flux lines

It is often helpful to work with one of five different magnetic potentials – see sections 5 and 20. Here we only mention the vector potential $\vec{A}$, with $\vec{B} = \vec{\nabla} x \vec{A}$, which for a solenoid may be reduced to the single component A_θ (r,z):

$$B_r = -\frac{\partial A_\theta}{\partial z}, \quad B_z = \frac{1}{r}\frac{\partial}{\partial r} r A_\theta . \tag{2.15a,b}$$

A flux surface is given by

$$rA_\theta(r,z) = \text{ constant.} \tag{2.16}$$

This is easily shown by considering any flux line that lies on a particular flux surface. The line has constant θ and it is only necessary to show that rA_θ is constant along it. Since by definition the flux line element $d\vec{r}$ is parallel to $\vec{B}$, the differential of rA_θ along the line is

$$d(rA_\theta) = (\frac{\partial}{\partial r} rA_\theta)dr + (\frac{\partial rA_\theta}{\partial z})dz = r(B_z dr - B_r dz) = r\hat{e}_\theta \cdot (\vec{B} x \vec{dr}) = 0 . \tag{2.17}$$

If adjacent flux surfaces have constants $rA_\theta = C_1$ and C_2, then the magnetic flux contained between the two surfaces is $2\pi(C_2 - C_1)$. The mean field strength midway between the two flux surfaces is approximately

$$\langle B \rangle = \frac{C_2 - C_1}{\Delta \cdot r}, \tag{2.18}$$

where Δ is the local normal distance between the surfaces and r is the radial distance to the midpoint between the surfaces. Due to the factor of r^{-1} in eqn. (2.18), the magnitude of $\vec{B}$ is not simply proportional to the inverse spacing between flux surfaces $\left(\Delta^{-1}\right)$ as is sometimes assumed, although this can be a useful visual aid in a region where r is nearly constant. The local density of flux lines through any plane normal to $\vec{B}$ can be specified to be proportional to $\left|\vec{B}\right|$, however this is not always done when making flux line plots. A flux surface has the topology of a torus, and a system made of more than one magnet may have several flux surfaces corresponding to a given value of rA_θ.

Another way to generate a flux line is to solve the equation

$$\frac{d\vec{r}}{ds} = \frac{\vec{B}(\vec{r})}{\left|\vec{B}(\vec{r})\right|}, \tag{2.19}$$

starting from some point on the line of interest. Here $\vec{r}$ (s) is simply the parameterization of the line, with s denoting distance along the line. For example the starting point could be on the surface of an acceleration gap where unwanted electrons are emitted.

2.5 Stress and energy

Material stress is not the topic of this report, but it is of major concern in the design of high field magnets, so a simple estimate is presented here. The force density from the field in the current carrying wire is

$$\vec{J}x\vec{B} = \hat{e}_r J_\theta B_z - \hat{e}_z J_\theta B_r. \tag{2.20}$$

Since the wire is in mechanical equilibrium, this force density must equal the divergence of the material stress tensor, which itself is proportional to components of the gradient of the microscopic mechanical displacement field in the magnet. A detailed analysis is too complicated to summarize here (see e.g. ref [1-2]), but it is seen from eqn. (2.20) that the longitudinal magnetic force tends to compress a wire layer while the radial magnetic force pushes it outwards against a restraining collar of the magnet assembly. There can be no radial pressure in the vacuum bore, so at the collar it is approximately

$$\mathrm{P} \approx \int dr J_\theta B_z \approx \frac{B_w^2}{2\mu_0}, \tag{2.21}$$

where B_w is the longitudinal field at the inner wire edge of the coil – roughly the peak bore field. Suppose $B_w = 1.0T$, then $P \approx \left((1.0)^2 / 2x4\pi x10^{-7}\right) \approx 4x10^5 P\mathrm{a} \approx 4.0$ Bar,

which is quite modest. However a 15.0T bore field produces roughly 900 Bar, which can crush some insulation.

The external field of a solenoid without a permeable return yoke extends to a large distance compared to that of a quadrupole magnet. The estimation of stresses, wire field, etc. of a system of solenoids must therefore include the field contributions of nearby magnets as well as that of the magnet of interest. This is particularly the case for a transport lattice made of closely spaced solenoids.

Since solenoidal transport systems for energetic ions are expected to have high fields in large-bore magnets, they also have large stored field energy. In the absence of magnetic materials this is

$$W = \int d^3 r \frac{\left|\vec{B}\right|^2}{2\mu_0} \quad . \tag{2.22}$$

For example if a 1.0 m^3 volume is filled with a 15T field, then the stored energy is $15^2 / \left(2x4\pi x10^{-7}\right) \approx 90\text{MJ}$.

3. Near-Axis Field

For simulating beam dynamics it is often sufficient to accurately approximate the magnetic field near the system axis, e.g. out to 50% of the radius of the nearest wire layer. A general treatment is presented here and some useful examples of the on-axis field are given in section 4.

3.1 On-axis field and near-axis expansion

Recall eqn. (2.3a) for B_z :

$$\nabla^2 B_z = -\mu_0 \frac{1}{r}\frac{\partial}{\partial r} r J_\theta \,. \tag{3.1}$$

This may be formally integrated using the Green function for the 3-d scalar Laplacian operator (see section 6):

$$B_z = \frac{\mu_0}{4\pi} \int d^3 r' \frac{\frac{1}{r'}\frac{\partial}{\partial r'} r' J'_\theta}{\left|\vec{r}' - \vec{r}\right|} \,, \tag{3.2}$$

or explicitly in cylindrical coordinates,

$$B_z = \frac{\mu_0}{4\pi} \int_{-\infty}^{+\infty} dz' \int_0^{\infty} dr' r' \int_0^{2\pi} d\theta' \frac{\frac{1}{r'}\frac{\partial}{\partial r'} r' J_\theta(r', z')}{\sqrt{(z'-z)^2 + r'^2 + r^2 - 2r'r\cos(\theta' - \theta)}} \quad . \tag{3.3}$$

Here and in similar integrations we may set $\theta = 0$ inside the integrand since by symmetry B_z is a function only of r and z. After an integration by parts in r' we get

$$B_z(r,z) = \frac{\mu_0}{4\pi} \int_{-\infty}^{+\infty} dz' \int_0^{\infty} dr' r' J_\theta(r', z') \int_0^{2\pi} d\theta' \frac{(r' - r\cos(\theta'))}{\sqrt{(z'-z)^2 + r'^2 + r^2 - 2r'r\cos(\theta')}^3} . \tag{3.4}$$

This formula is completely general for a static solenoidal field, and it gives the right answer even when the current layer extends to infinity in z.

To get the near-axis field, inside the bore where $J_\theta = 0$, we first define the on-axis field:

$$B_0(z) \equiv B_z(r = 0, z) = \frac{\mu_0}{2} \int_{-\infty}^{+\infty} dz' \int_0^{\infty} dr' \frac{r'^2 J_\theta(r', z')}{\sqrt{(z'-z)^2 + r'^2}^3} \quad . \tag{3.5}$$

If $B_0(z)$ is accurately determined from this expression or in some other way, such as measurements on a real magnet assembly, then $B_0(z)$ may be used to generate a power series solution of eqn. (3.1), which is valid in the magnet bore. From

$$\frac{1}{r}\frac{\partial}{\partial r} r \frac{\partial B_z}{\partial r} = -\frac{\partial^2 B_z}{\partial z^2} ,$$

we get by iteration:

$$B_z(r,z) = B_0 - \frac{B_0'' r^2}{4} + \frac{B_0'''' r^4}{64} - \frac{B_0^{vi} r^6}{2304} + \ldots . \tag{3.6a}$$

The radial field component is easily obtained from $\vec{\nabla} \cdot \vec{B} = 0$ by integrating in r:

$$B_r(r,z) = -\frac{1}{r} \int_0^r dr' r' \frac{\partial B_z(r', z)}{\partial z} = -\frac{B_0' r}{2} + \frac{B_0''' r^3}{16} - \frac{B_0^{v} r^5}{384} + \frac{B_0^{vii} r^7}{18432} - \ldots . \tag{3.6b}$$

The leading term in each of the above expansions of B_z and B_r is used when computing the linearized dynamics of beam ions. Higher order (non-linear in r) terms are referred to as "fringe field aberrations" in this context. A few terms from the expansions

usually give an accurate field representation inside the vacuum bore, especially near the magnet center, but the expansion for B_z fails in the wire and beyond, where the field component generally reverses sign. The expansion for B_r often gives a fair approximation in the wire except near the magnet ends. When truncating the expansions after some power of r, B_r should be represented by one power higher than B_z in order to preserve $\vec{\nabla} \cdot \vec{B} = 0$. Crossing a thin wire layer of total surface current layer density $S(z)$, B_z jumps by $-\mu_0 S(z)$ but B_r is continuous. However B_r has logarithmic singularities at the ends of the layer – see section 8. For large $|z|$, well beyond any magnet end, the power series expansions are valid out to values of r comparable to the longitudinal distance from the magnet end. But the expansions do not correctly represent the reversal of B_z at larger values of r. Also, because of the high order derivatives, the expansions of B_r and B_z are difficult to apply using measured B_0.

By applying Stoke's theorem to $\vec{\nabla} x \vec{B} = \mu_0 \vec{J}$, we obtain the useful general result:

$$\int_{-\infty}^{+\infty} dz \; B_0(z) = \mu_0 \int_{-\infty}^{+\infty} dz \, S(z) \; . \tag{3.7}$$

This may also be derived from eqn. (3.5) using the indefinite integral (3.10a) given at the end of this section.

For the thin semi-infinite wire layer,

$$J_\theta = SH(-z)\delta(r - R) \; , \tag{3.8}$$

we get from eqn. (3.5) - see section 4**:**

$$B_0(z) = \frac{\mu_0 S}{2}\left(1 - \frac{z}{\sqrt{z^2 + R^2}}\right). \tag{3.9}$$

In this representative case fringe field aberrations are maximum at z=0 for B_r and at $z \approx \pm .5R$ for B_z. Approximating the fields by only two terms works well for r<.5R, but for r=.8R (the largest value one would consider for beam transport) the convergence is slow, as shown in the following tables. Note that the approximated B_z oscillates as higher order terms are added.

Number of expansion terms	$B_z / \mu_0 S$ at r=.8R, z=.5R	$B_r / \mu_0 S$ at r=.8R, z=0
1	.276393	.200000
2	.207701	.248000
3	.190116	.267200
4	.189066	.276160
5	.190881	.280676
exact.	.191960	.286062

Number of expansion terms	$B_z / \mu_0 S$ at r=.5R, z=.5R	$B_r / \mu_0 S$ at r=.5R, z=0
1	.276393	.125000
2	.249560	.136719
3	.246877	.138550
4	.246814	.138884
5	.246857	.138949
exact.	.246867	.138967

3.2 Useful integrals

The following (easily verified) indefinite integrals are of use in subsequent sections:

$$\int \frac{dx}{\sqrt{x^2+a^2}^3} = \frac{x}{a^2\sqrt{x^2+a^2}}, \tag{3.10a}$$

$$\int \frac{dx}{\sqrt{x^2+a^2}} = Log\left(\frac{x+\sqrt{x^2+a^2}}{a}\right) = \sinh^{-1}(x/a)\ , \tag{3.10b}$$

$$\int \frac{dx}{x^2-a^2} = -\frac{1}{a}\tanh^{-1}\left(\frac{x}{a}\right), \tag{3.10c}$$

$$\int \frac{dx}{\left(ax^2+b\right)\sqrt{fx^2+g}} = \frac{1}{\sqrt{b\left(ag-bf\right)}} \tan^{-1}\left(\frac{x\sqrt{ag-bf}}{\sqrt{b\left(fx^2+g\right)}} \right) \ , \qquad (3.10d)$$

[for $a,b,f,g>0$ and $ag-bf>0$].

The surprising integral (3.10d) is used in section 9 (along with 3.10b and 3.10c) to evaluate $B_z(r,z)$ for a uniform, thick current layer.

4. Design Formulas for the On-Axis Field

4.1 Simple cases

To calculate the on-axis field $B_0(z)$ we may replace a moderately thick, uniform wire layer with a thin layer at its average radius (R) with surprisingly little error – see section 9. Making this approximation results in a number of very simple formulas. The current density has the simple form:

$$J_\theta(r,z) = S(z)\delta(r-R) \ , \qquad (4.1)$$

and eqn. (3.5) becomes

$$B_0(z) = \frac{\mu_0}{2}\int_{-\infty}^{+\infty} dz' \frac{R^2 S(z')}{\sqrt{(z'-z)^2+R^2}^3} \ . \qquad (4.2)$$

Case 1 Constant $S(z)=S$ for all z:

Using the integral (3.10a) we recover eqn. (2.5a),

$$B_0 = \frac{\mu_0 S}{2} \frac{(z'-z)}{\sqrt{(z'-z)^2+R^2}} \Big|_{-\infty}^{+\infty} = \mu_0 S \ . \qquad (4.3)$$

Case 2 Semi-infinite Layer:

$$S(z) = \begin{cases} S, & -\infty < z < z_0 \\ 0, & z_0 < z < \infty \end{cases} \ , \qquad (4.4)$$

A very useful formula is derived by changing the upper limit of integration over z' to z_0 in eqn. (4.3):

$$B_0(z) = \frac{\mu_0 S}{2} \frac{(z'-z)}{\sqrt{(z'-z)^2 + R^2}} \Bigg|_{-\infty}^{z_0} = \frac{\mu_0 S}{2} \left[1 - \frac{(z-z_0)}{\sqrt{(z-z_0)^2 + R^2}} \right] . \tag{4.5}$$

Note the symmetry around z_0, with $B_0(z_0) = \mu_0 S/2$. We may build up many other cases of interest by superposition using this result.

Case 3 Lens of wire layer length ℓ, centered at $z = 0$:

We apply eqn. (4.5) with positive and negative current layers ending respectively at $\ell/2$ and $-\ell/2$:

$$B_0^{lens}(z) = \frac{\mu_0 S}{2} \left[\frac{(z+\ell/2)}{\sqrt{(z+\ell/2)^2 + R^2}} - \frac{(z-\ell/2)}{\sqrt{(z-\ell/2)^2 + R^2}} \right] . \tag{4.6}$$

This formula is equivalent to the well-known textbook result [4-1]:

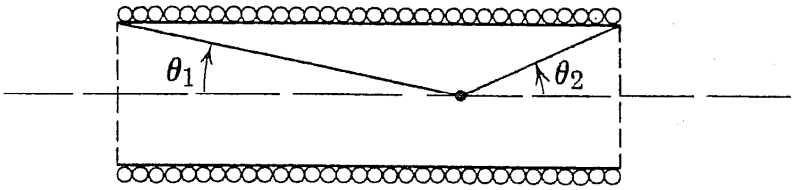

$$B_0 = \frac{\mu_0 NI}{2} \left[\cos(\theta_1) + \cos(\theta_2) \right] , \tag{4.7}$$

where N is the number of wire loops per meter, each carrying current I, and the angles are to points at the wire layer ends drawn from the point of interest on the z axis (see figure). The field at the lens midpoint $(r = 0, z = 0)$ is

$$B_0^{lens}(0) = \frac{\mu_0 S}{\sqrt{1 + 4R^2/\ell^2}} , \tag{4.8}$$

so a lens of length $\ell = 2R$ has peak field on axis reduced to $\mu_0 S/\sqrt{2} = .7071\mu_0 S$. For $|z|$ large, the leading order expansion term of eqn. (4.6) is

$$B_0 \to \frac{\mu_0 S R^2 \ell}{2|z|^3} \quad , \tag{4.9}$$

consistent with eqn. (2.13b). The on-axis field of a short lens $(\mu_0 S = 1.0\,\mathrm{T},\ \mathrm{R} = .25\,\mathrm{m},\ \ell = 1.0\,\mathrm{m})$is displayed below.

```
In[57]:= (*on-axis field of a short lens*)

         mu0S = 1.0;
         R = .25;
         l = 1.0;

         B0[z_] = mu0S / 2 * ((z + l / 2) / ((z + l / 2) ^ 2 + R ^ 2) ^ .5 - (z - l / 2) / ((z - l / 2) ^ 2 + R ^ 2) ^ .5);

         Plot[{B0[z], If[-l / 2 ≤ z ≤ l / 2, 1, 0]}, {z, -2 * l, 2 * l}];
```

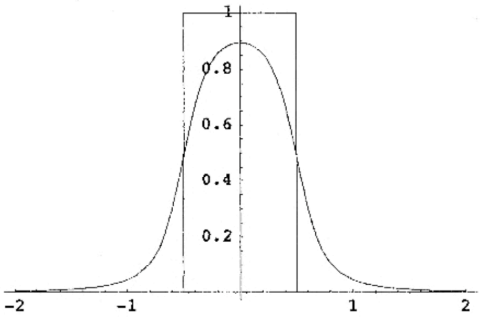


```
In[62]:= {B0[0], B0[.5 * l], B0[l], B0[1.5 * l]}

Out[62]= {0.894427, 0.485071, 0.0459834, 0.0110677}
```

Case 4 Periodic system of lenses of wire layer length ℓ, gap length g, and period P=ℓ+g:

$$B_0(z) = \sum_{n=-\infty}^{\infty} B_0^{\mathrm{lens}}(z - nP) \tag{4.10}$$

Case 5 Gap of length g, centered at z=0, between long solenoids:

We subtract a lens of length g from an infinitely long solenoid;

$$B_0^{\mathrm{gap}}(z) = \mu_0 S - B_0^{\mathrm{lens}}(z) \ . \tag{4.11}$$

At the center of the gap

$$B_0^{\text{gap}}(0) = \mu_0 S\left(1 - \frac{1}{\sqrt{1+4R^2/g^2}}\right). \tag{4.12}$$

For g=2R, the field at the gap center is reduced to $\left(1-1/\sqrt{2}\right)\mu_0 S = .2929\mu_0 S$. To prevent large variations of B_0 with z in a periodic system, the gaps must be very short compared with 2R. However, this is not generally necessary for the design of a good transport system if the ion betatron wavelength is longer than 2P.

Case 6 Current ring of radius R:

$$J_\theta = I\delta(r-R)\delta(z)\ . \tag{4.13}$$

From eqn. (3.5) or eqn. (4.2) we get

$$B_0^{ring}(z) = \frac{\mu_0 I R^2}{2\sqrt{z^2+R^2}^3}\ . \tag{4.14}$$

4.2 Thick wire layer

The on-axis field of a uniform, thick wire layer can be computed from any of the thin layer cases by a simple average over the radial position R:

$$B_0^{\text{thick}} = \int_{R_1}^{R_2} \frac{dR}{R_2 - R_1}\ B_0^{\text{thin}}(z;R)\ , \tag{4-15}$$

where R_1 and R_2 are the inner and outer radii of the layer. For example eqn. (4.6) for a simple lens of length ℓ gives, using the integral eqn. (3.10b):

$$\begin{aligned} B_0(z) &= \int_{R_1}^{R_2} \frac{dR}{R_2 - R_1}\ \frac{\mu_0 S}{2}\left\{\frac{(z+\ell/2)}{\sqrt{(z+\ell/2)^2+R^2}} - \frac{(z-\ell/2)}{\sqrt{(z-\ell/2)^2+R^2}}\right\} \\ &= \frac{\mu_0 S}{2(R_2-R_1)}\left\{(z+\ell/2)\text{Log}\left[\frac{R_2+\sqrt{(z+\ell/2)^2+R_2^2}}{R_1+\sqrt{(z+\ell/2)^2+R_1^2}}\right] - \right. \\ &\left. -(z-\ell/2)\text{Log}\left[\frac{R_2+\sqrt{(z-\ell/2)^2+R_2^2}}{R_1+\sqrt{(z-\ell/2)^2+R_1^2}}\right]\right\}. \end{aligned} \tag{4.16}$$

4.3 Uniform fields

Case 1 Helmholtz coil:

Two rings, each of radius R and current I, which are separated by distance L, have on-axis field, from eqn. (4.14):

$$B_0(z) = \frac{\mu_0 I R^2}{2}\left[\frac{1}{\sqrt{\left(z - L/2\right)^2 + R^2}^{\,3}} + \frac{1}{\sqrt{\left(z + L/2\right)^2 + R^2}^{\,3}}\right] . \tag{4.17}$$

If $L = R$ then $B_0''(0) = 0$. This is a simple way to make a uniform field close to the coil center, but it is not generally useful for beam focusing since the field strength in the wire is much larger than at the center.

Case 2 Nearly uniform field in a long solenoid:

A large volume of strong uniform field can be made by superposing simple solenoids of various lengths, radii and current layer densities. A mathematically simple (but unphysical) version consists of a pair of thin-layer lenses [see eqn. (4.6)] placed symmetrically around $z = 0$ at the same radius R, but with unequal lengths (ℓ_1, ℓ_2) and layer densities (S_1, S_2). The derivatives $B_0''(0)$ and B_0^{iv} both vanish if we set

$$\frac{\ell_2}{2R} = \sqrt{\frac{3(\ell_1/2R)^2 + 10}{4(\ell_1/2R)^2 - 3}} , \tag{4.18}$$

$$S_2 = -S_1\left(\frac{\ell_1}{\ell_2}\right)\sqrt{\frac{1 + (\ell_2/2R)^2}{1 + (\ell_1/2R)^2}}^{\,5} . \tag{4.19}$$

Layer #2 is shorter than #1 if $\ell_1/2R > \sqrt{2.5}$, and has a reversed current. Both layers must have $\ell/2R > \sqrt{.75}$. The combined layers produce a somewhat lower field strength than that of layer #1 alone:

$$B_0(0) = \frac{\mu_0 S_1 \ell_1/2}{\sqrt{(\ell_1/2)^2 + R^2}} + \frac{\mu_0 S_2 \ell_2/2}{\sqrt{(\ell_2/2)^2 + R^2}} . \tag{4.20}$$

For example, taking $\mu_0 S_1 = 10.0\text{T}$ and $\ell_1 = 4.0R$, we get $\mu_0 S_2 = -3.27097\text{T}$, and $\ell_2 = 2.60177R$, producing $B_0(0) = 6.35096T$. The #1 solenoid alone would produce $B_0(0) = 8.94427\text{T}$. On-axis fields for the double layer at representative points are

z/R	0	±.2	±.4	±.6	±.8	±1.0
B_0	6.35096	6.35096	6.35083	6.34929	6.34063	6.30777

There is essentially no variation over 25% of the bore length in this example and only .7% variation over 50% of the bore length. Transverse variation is similarly small in these zones.

Case 3 Uniform field inside an ellipsoidal shell:

Although this is not particularly useful for beam transport, it is worth mentioning that an ellipsoidal shell of constant current per meter (in z) produces an exactly constant field inside the enclosed volume. Denoting the cumulative current layer density

$$S(r,z) = S \cdot H\left(1 - \frac{r^2}{a^2} - \frac{z^2}{b^2}\right), \tag{4.21}$$

where a and b are ellipse radii, then

$$J_\theta = -\frac{\partial S(r,z)}{\partial r} = \frac{2r}{a^2} S \;\; \delta\left(1 - \frac{r^2}{a^2} - \frac{z^2}{b^2}\right). \tag{4.22}$$

This current pattern can be created with closely spaced wire loops each carrying current $I = S\Delta$, where Δ is the constant longitudinal separation between loops.

Eqn. (3.5) yields

$$B_0(z) = \frac{\mu_0 S a^2}{2} \int_{-b}^{b} dz' \frac{\left(1 - z'^{\,2}/b^2\right)}{\sqrt{\left(z' - z\right)^2 + a^2\left(1 - z'^{\,2}/b^2\right)}^3}, \tag{4.23}$$

from which it may be numerically verified that $B_0(z)$ is actually constant for $|z| < b$. B_z is therefore also independent of r inside the ellipsoid, and we may write

$$B_z^{\text{inside}} = \mu_0 S f(a/b), \tag{4.24}$$

$$f(a/b) = \frac{a^2}{b^2}\int_0^1 \frac{dy\left(1-y^2\right)}{\sqrt{y^2 + \frac{a^2}{b^2}\left(1-y^2\right)}^3} \ . \tag{4.25}$$

a/b	0	.25	.50	1.0	2.0	4.0	∞
f	1.00000	.924593	.826436	.666667	.472800	.296359	.000000

A proof that B_z is constant is mathematically related to the solution for the gravitational potential of an ellipsoid of constant density, obtained in the Eighteenth Century [4-2]. It is found by elementary integration that for $a/b \equiv x < 1$

$$f(x) = \frac{1}{1-x^2}\left[1 - \frac{x^2}{\sqrt{1-x^2}}\text{Log}\left(\frac{1+\sqrt{1-\text{x}^2}}{\text{x}}\right)\right], \tag{4.26a}$$

and for $a/b = x > 1$,

$$f(x) = \frac{1}{x^2-1}\left[\frac{x^2}{\sqrt{x^2-1}}\sin^{-1}\left(\frac{\sqrt{\text{x}^2-1}}{\text{x}}\right) - 1\right]. \tag{4.26b}$$

If several elliptical shells of the form (4.21 – 4.22) are superposed and all have the same ratio a/b, then the interior field is still given by (4.24), but with $S = \sum\ S_i$.

References

4-1 See e.g. Reference [1-1], J.D. Jackson, pg. 225.

4-2 Chandrasekhar, S., Ellipoidal Figures of Equilibrium, Chapter 3, Dover Publications, New York, 1969.

5. <u>Vector and Scalar Potentials</u>

The vector potential A_θ and four scalar potentials, denoted here by ϕ, φ, Φ and Ψ, are of use in calculating and visualizing solenoidal fields. Each potential has features that make it useful for some applications and a poor choice for others. The scalar potentials ϕ and φ are defined below, while Φ and Ψ are special potentials used in Tosca© and described in section 19.

5.1 Vector potential (A_θ)

As discussed in section 2, the vector potential is useful for defining and plotting flux surfaces. Another property of A_θ is that the field components

$$B_r = -\frac{\partial A_\theta}{\partial z}, \qquad B_z = \frac{1}{r}\frac{\partial}{\partial r} r A_\theta \ , \tag{5.1 a,b}$$

automatically satisfy $\vec{\nabla} \cdot \vec{B} = 0$. This is an advantage in beam dynamics applications, where the conservation of canonical angular momentum

$$P_\theta = r\left(\gamma M v_\theta + qeA_\theta\right) \tag{5.2}$$

for an ion of $\theta-$ momentum $\gamma M v_\theta$ and charge qe, might otherwise be violated by an approximate representation of the field; e.g. constant P_θ can be used as an equation of motion.

Unlike the scalar potential ϕ described below, the vector potential provides a complete (or "global") characterization of the magnetic field, which is valid everywhere. Its source is J_θ , and if a magnetization current density J_θ^{mag} is present, it simply adds to the current density of the wire layer. The second order equation for A_θ is

$$\frac{\partial}{\partial r}\frac{1}{r}\frac{\partial}{\partial r} r A_\theta + \frac{\partial^2 A_\theta}{\partial z^2} = \frac{\partial B_z}{\partial r} - \frac{\partial B_r}{\partial z} = -\mu_0 J_\theta \ . \tag{5.3}$$

As with eqn. (2.3b) for B_r **,** the operator acting on A_θ is not quite the scalar Laplacian, but this does not cause a serious problem in obtaining a Green function solution – see section 6.

One drawback in using A_θ (or the scalar potentials) to calculate $\vec{B}$ is that it must be differentiated, which is an extra operation that can produce unnecessarily complicated expressions. Also, derivatives generate extra errors in discretized, numerical models. Another drawback is that A_θ is the azimuthal component of a vector field and must therefore be handled carefully when transforming from a tilted magnet.

5.2 Magnetic scalar potential (ϕ)

The field in the bore of a magnetic dipole, quadrupole, or higher order magnetic beam line element is often characterized by a magnetic scalar potential ϕ. For a connected region of vacuum, where $\vec{\nabla} x \vec{B} = 0$, we can set

$$\vec{B} = \mu_0 \vec{\nabla}\phi, \qquad \nabla^2\phi = \vec{\nabla} \cdot \vec{B} / \mu_0 = 0 \ , \tag{5.4 a,b}$$

where the permeability of vacuum μ_0 is inserted to be consistent with standard convention. This is an attractive, compact formalism for aberrations, which are represented as higher order multipoles, e.g. $\phi \sim \phi_n(r,z)\cos(n\theta)$, as well as fringe field terms. A magnetic scalar potential may also be used to characterize the bore field in a solenoidal system.

By itself ϕ cannot be a global solution. It is necessary to connect ϕ to its current source through boundary conditions or an already known component of $\vec{B}$. For example ϕ may be assumed constant on the surface of a highly permeable material if the magnetic field is well below saturation, e.g. $B \le 1.0T$ for magnetically soft iron. In fact this formalism is most useful when magnetic materials are present, with $\vec{H} = \vec{\nabla}\phi$ everywhere outside the wire and $\vec{B} = \mu_0 \vec{H}$ in vacuum –see sections 16 and 17. Another difficulty with ϕ is that it is usually multi-valued. This follows from $\oint \vec{B} \cdot \vec{dr} \neq 0$ integrated around any loop that encloses a current layer. The idea is to position the discontinuity (if any) somewhere such that a single branch of ϕ can be applied in the region of interest.

Surfaces with ϕ = constant have perpendicular intersections with surfaces with rA_θ = constant. The constant ϕ surfaces may be specified such that their separation is inversely proportional to $\left|\vec{B}\right|$ throughout the vacuum region where a scalar potential is valid.

5.3 Global scalar potential (φ)

The limitations of the magnetic scalar potential may be circumvented for a solenoid by defining a global scalar potential φ. Let

$$\vec{B} = \mu_0 S(r,z)\hat{e}_z + \vec{\nabla}\varphi, \tag{5.5}$$

where $S(r,z)$ is the cumulative current layer density defined in section 2 and $\vec{J}^{\,\mathrm{mag}} = 0$. This formula for $\vec{B}$ satisfies $\vec{\nabla} x \vec{B} = \mu_0 \vec{J}$. To make $\vec{\nabla} \cdot \vec{B} = 0$ we set

$$\nabla^2\varphi = -\frac{\partial}{\partial z}\mu_0 S(r,z) \ . \tag{5.6}$$

The term $\mu_0 S(r,z)\hat{e}_z$ in eqn. (5.5) is just the previously defined direct field of the system (see section 2), and $\vec{\nabla}\varphi$ is the residual field (i.e. fringe field, external field, etc.). It is clear from eqn. (5.5) that φ is single valued since $\vec{B} - \mu_0 S(r,z)\hat{e}_z$ has vanishing curl. Also, φ is a global solution since eqn. (5.6) is valid over all space. In principle a global scalar potential can be defined for any configuration of currents, but it is not useful unless $\vec{\nabla} x \vec{B} = \mu_0 \vec{J}$ has a simple solution, as is the case for a solenoidal system.

Note that $\vec{\nabla}\varphi$ is discontinuous at the ends of a magnet bore and it generally subtracts from the direct field inside the bore. This is a very awkward way to treat the field close to the axis, where it is used for beam dynamics calculations, and continuity may be important. However, φ gives an intuitively appealing picture of the external field by an analogy with electrostatics, where the source on the rhs of eqn. (5.6) acts like a charge density proportional to $\partial S(r,z)/\partial z$. For a thin current layer at radius R, this source is a pair of disks of opposite magnetic charge $\left(\pm\pi R^2 \mu_0 S\right)$ at the solenoid ends. In section 11 the global scalar potential will be used to approximate the external field, which will in turn be used to calculate the interference of fields among off-axis solenoids in section 15.

6. Green Function Solutions

6.1 Green function formalism

Any equation of the form (in 3-d)

$$\nabla^2 f = g\left(\vec{r}\right), \tag{6.1}$$

with $g\left(\vec{r}\right) = 0$ at large $\left|\vec{r}\right|$, may be formally integrated using the Green function

$$G\left(\vec{r},\vec{r'}\right) = \frac{-1}{4\pi\left|\vec{r'} - \vec{r}\right|}\ ; \tag{6.2}$$

$$f\left(\vec{r}\right) = \int d^3 r' G\left(\vec{r},\vec{r'}\right) g\left(\vec{r'}\right). \tag{6.3}$$

This works because

$$\nabla^2 G = \nabla'^2 G = \delta\left(\vec{r'} - \vec{r}\right), \tag{6.4}$$

where $\delta\left(\vec{x}\right)$ denotes the 3-d Dirac delta function.

We have already used $G\left(\vec{r},\vec{r'}\right)$ to solve for B_z in section (3):

$$B_z = \frac{\mu_0}{4\pi}\int d^3r'\left(\frac{1}{r'}\frac{\partial}{\partial r'}r'J'_\theta\right)\frac{1}{\left|\vec{r'}-\vec{r}\right|} = \frac{\mu_0}{4\pi}\int d^3r' J'_\theta \frac{r'-r\cos(\theta'-\theta)}{\left|\vec{r'}-\vec{r}\right|^3}. \qquad (6.5)$$

Equation (5.6) for the gobal scalar potential φ is also of the proper form for application of the Green function:

$$\varphi = \frac{\mu_0}{4\pi}\int d^3r'\left(\frac{\partial S'}{\partial z'}\right)\frac{1}{\left|\vec{r'}-\vec{r}\right|} \quad . \qquad (6.6)$$

Equations (2.3b) for B_r and (5.3) for A_θ do not have the Laplacian operator, but they may be converted to the desired form by multiplying both sides by $\cos\theta$, i.e.

$$\nabla^2\left(B_r\cos\theta\right) = \left(\frac{\partial}{\partial r}\frac{1}{r}\frac{\partial}{\partial r}rB_r + \frac{\partial^2 B_r}{\partial z^2}\right)\cos\theta = \mu_0\frac{J_\theta}{\partial z}\cos\theta \quad . \qquad (6.7)$$

This yields

$$B_r = -\frac{\mu_0}{4\pi}\int d^3r'\left(\frac{\partial J'_\theta}{\partial z'}\right)\frac{\cos(\theta'-\theta)}{\left|\vec{r'}-\vec{r}\right|} \ , \qquad (6.8)$$

where we have used the identity

$$\cos(\theta') = \cos(\theta)\cos(\theta'-\theta) - \sin(\theta)\sin(\theta'-\theta)$$

inside the Green function integral. In similar fashion we get

$$A_\theta = \frac{\mu_0}{4\pi}\int d^3r' J_\theta{}' \frac{\cos(\theta'-\theta)}{\left|\vec{r'}-\vec{r}\right|} \quad . \qquad (6.9)$$

The four Green function solutions given above all have denominators that are odd powers of the function

$$\left|\vec{r'}-\vec{r}\right| = \left[(z'-z)^2 + r'^2 + r^2 - 2r'r\ \cos(\theta'-\theta)\right]^{1/2}. \qquad (6.10)$$

Several simplifications can be made. First, by symmetry, we may let $\theta'-\theta \to \theta'$ everywhere in an integrand. Second, if a derivative with respect to z or z' appears in the integrand, we may use the identity

$$\frac{\partial}{\partial z}\frac{1}{\left|\vec{r}'-\vec{r}\right|}=-\frac{\partial}{\partial z'}\frac{1}{\left|\vec{r}'-\vec{r}\right|}\ , \tag{6.11}$$

integrate by parts, and sometimes get a simplification. For example, a unit step-function of z' can be turned into a delta function of z'.

6.2 Explicit field expressions

Writing everything explicitly, we have

$$B_z=\frac{\mu_0}{4\pi}\int_{-\infty}^{+\infty}dz'\int_0^{\infty}dr'r'J_\theta\left(r',z'\right)\int_0^{2\pi}d\theta'\frac{\left(r'-r\cos\left(\theta'\right)\right)}{\sqrt{\left(z'-z\right)^2+r'+r^2-2r'r\cos\left(\theta'\right)}^3}\ . \tag{6.12}$$

Denoting the denominator in eqn. (6.12) by $\sqrt{.....}^3$ we get for the other fields

$$B_r=-\frac{\mu_0}{4\pi}\int_{-\infty}^{+\infty}dz'\int_0^{\infty}dr'r'\frac{\partial J_\theta\left(r',z'\right)}{\partial z'}\int_0^{2\pi}d\theta'\frac{\cos\left(\theta'\right)}{\sqrt{.....}}\ , \tag{6.13}$$

$$A_\theta=\frac{\mu_0}{4\pi}\int_{-\infty}^{+\infty}dz'\int_0^{\infty}dr'r'J_\theta\left(r',z'\right)\int_0^{2\pi}d\theta'\frac{\cos\left(\theta'\right)}{\sqrt{.....}}\ , \tag{6.14}$$

$$\varphi=\frac{\mu_0}{4\pi}\int_{-\infty}^{+\infty}dz'\int_0^{\infty}dr'r'\frac{\partial S\left(r',z'\right)}{\partial z'}\int_0^{2\pi}d\theta'\frac{1}{\sqrt{.....}}\ . \tag{6.15}$$

It is clear that if we derive $B_r=-\partial A_\theta/\partial z$ from eqn. (6.14) we will simply recover the result obtained by direct integration, eqn. (6.13). We may also derive $B_z=\frac{1}{r}\frac{\partial}{\partial r}rA_\theta$ using eqn. (6.14). This procedure is clearly correct, but it is not obvious from inspection that the result is actually equivalent to the direct integration, eqn. (6.12). We therefore have the alternative form:

$$\begin{aligned}B_z&=\frac{1}{r}\frac{\partial}{\partial r}rA_\theta=\frac{\mu_0}{4\pi}\int_{-\infty}^{+\infty}dz'\int_0^{\infty}dr'r'J_\theta\left(r',z'\right)\\&\cdot\int_0^{2\pi}d\theta'\cos\left(\theta'\right)\left[\frac{1}{r\sqrt{.....}}-\frac{r-r'\cos\left(\theta'\right)}{\sqrt{.....}^3}\right].\end{aligned} \tag{6.16}$$

It may be verified from numerical examples that the two formulas for B_z are the same. Mathematically, their equivalence can be reduced to the identity

$$\int_0^{2\pi} d\theta \sqrt{1-a\cos(\theta)} = \left(1-a^2\right) \int_0^{2\pi} d\theta \frac{1}{\sqrt{1-a\cos(\theta)}^3} , \tag{6.17}$$

which is also not obvious. However it can be shown that the two sides of eqn. (6.17) have the same expansion coefficients multiplying all powers of a^2. This identity will be used in section 7 and below in eqn. (6.25d).

Not surprisingly, there is also a second integral expression for A_θ, which can be derived from eqns. (6.5) and (6.9):

$$A_\theta = rB_z - r\frac{\partial A_\theta}{\partial r} \tag{6.18}$$

$$= \frac{\mu_0}{4\pi} \int d^3r' \frac{J'_\theta \; r'r\sin^2(\theta'-\theta)}{\left|\vec{r'}-\vec{r}\right|^3} \tag{6.19}$$

$$= \frac{\mu_0}{4\pi} \int_{-\infty}^{+\infty} dz' \int_0^{\infty} dr' r'^2 r J_\theta(r',z') \int_0^{2\pi} d\theta' \frac{\sin^2(\theta')}{\sqrt{.....}^3} . \tag{6.20}$$

Similar to eqn. (6.17), the equivalence of this expression and eqn. (6.14) implies a non-trival identity:

$$\int_0^{2\pi} d\theta \frac{\sin^2(\theta)}{\sqrt{1-a\cos(\theta)}^3} = \frac{2}{a} \int_0^{2\pi} d\theta \frac{\cos(\theta)}{\sqrt{1-a\cos(\theta)}} . \tag{6.21}$$

Numerical integration of the Green function solutions is greatly simplified when the integrals over θ' are worked in advance, leaving only integrations over r' and z'. This can be done exactly using the complete elliptic integrals E and K, or in an accurate approximation using analytical fits – see section 7. First we isolate the essential θ' integrations; denote

$$a(r,z,r',z') \equiv \frac{2rr'}{(z'-z)^2 + r^2 + r'^2} , \tag{6.22}$$

which has range $0 \le a \le 1$, and define five functions:

$$f_0(a) = \int_0^{2\pi} \frac{d\theta}{2\pi} \sqrt{1-a\cos(\theta)} , \tag{6.23a}$$

$$f_1(a) = \int_0^{2\pi} \frac{d\theta}{2\pi} \frac{\cos(\theta)}{\sqrt{1-a\cos(\theta)}} , \tag{6.23b}$$

$$f_2(a) = \int_0^{2\pi} \frac{d\theta}{2\pi} \frac{1}{\sqrt{1 - a\cos(\theta)}} \ , \tag{6.23c}$$

$$f_3(a) = \int_0^{2\pi} \frac{d\theta}{2\pi} \frac{\cos(\theta)}{\sqrt{1 - a\cos(\theta)}^3} \ , \tag{6.23d}$$

$$f_4(a) = \int_0^{2\pi} \frac{d\theta}{2\pi} \frac{1}{\sqrt{1 - a\cos(\theta)}^3} \ . \tag{6.23e}$$

We express f_0 and f_2 in terms of E and K; the standard definitions [6-1] are

$$E(x) = \int_0^{\pi/2} dy \sqrt{1 - x\sin^2(y)} \ , \tag{6.24a}$$

$$K(x) = \int_0^{\pi/2} dy \frac{1}{\sqrt{1 - x\sin^2(y)}} \ . \tag{6.24b}$$

[Warning: these definitions of $\mathrm{E}(x)$ and $K(x)$ are used in Mathematica® [6-2], but in some texts x^2 appears in the integrands instead of x.] Using these expressions and a change of variable, we have

$$f_0(a) = \frac{2\sqrt{1+a}}{\pi} E\left(\frac{2a}{1+a}\right) , \tag{6.25a}$$

$$f_2(a) = \frac{2}{\pi\sqrt{1+a}} K\left(\frac{2a}{1+a}\right) , \tag{6.25b}$$

and the remaining $f_i(a)$ are found from f_0 and f_2 using the relations

$$f_1(a) = \frac{1}{a}\left(f_2(a) - f_0(a)\right) , \tag{6.25c}$$

$$f_4(a) = \frac{f_0(a)}{1 - a^2} \ , \tag{6.25d}$$

$$f_3(a) = \frac{1}{a}\left(\frac{f_0(a)}{1 - a^2} - f_2(a)\right) . \tag{6.25e}$$

The four Green function solutions, eqns. (6.12-6.15), are reduced to

$$B_z = \frac{\mu_0}{2} \int_{-\infty}^{+\infty} dz' \int_0^{\infty} dr' r'^2 J_\theta(r', z') \sqrt{\frac{a}{2rr'}}^3 \left[f_4(a) - \frac{r}{r'} f_3(a) \right] , \tag{6.26}$$

$$B_r = \frac{-\mu_0}{2}\int_{-\infty}^{+\infty} dz' \int_0^{\infty} dr' r' \frac{\partial J_\theta(r',z')}{\partial z'} \sqrt{\frac{a}{2rr'}} f_1(a) \ , \tag{6.27}$$

$$A_\theta = \frac{\mu_0}{2}\int_{-\infty}^{+\infty} dz' \int_0^{\infty} dr' r' J_\theta(r',z') \sqrt{\frac{a}{2rr'}} f_1(a) \ , \tag{6.28}$$

$$\varphi = \frac{\mu_0}{2}\int_{-\infty}^{+\infty} dz' \int_0^{\infty} dr' r' \frac{\partial S(r',z')}{\partial z'} \sqrt{\frac{a}{2rr'}} f_2(a) \ . \tag{6.29}$$

References

6-1 Abramowitz, M. and Stegun, I.A., Handbook of Mathematical Functions, Dover, New York (1965).

6-2 Wolfram, S., The Mathematica® Book, 3rd edition, Cambridge University Press (1991).

7. Approximation of the Green Function Integrals

The complete elliptic integrals E and K, defined in section 6, may be used to accurately evaluate the functions $f_i(a)$ that appear in the general Green function solutions for B_z, B_r, A_θ and φ. However, the resulting formulas are complicated and not very revealing. One might just as well evaluate the $f_i(a)$ numerically from their defining integrals (see plots of $f_i(a)$ below). Except for f_0, which is defined to help evaluate the other integrals, all of the f_i diverge as $a \to 1$, so their Taylor series expansions are of limited value. However, since

$$a \equiv \frac{2rr'}{(z'-z)^2 + r'^2 + r^2} \tag{7.1}$$

is small when r is either large or small, these expansions may be used to evaluate both the near-axis field and far field. Expanding $\sqrt{1 - a\cos(\theta)}$ in the integrands and calculating the resulting elementary integrals yields:

$$f_0(a) = \int_0^{2\pi} \frac{d\theta}{2\pi} \sqrt{1 - a\cos(\theta)} = \left(1 - \frac{1}{16}a^2 - \frac{15}{1024}a^4 - \frac{105}{16384}a^6 \cdots\right) , \tag{7.2a}$$

$$f_1(a) = \int_0^{2\pi} \frac{d\theta}{2\pi} \frac{\cos(\theta)}{\sqrt{1 - a\cos(\theta)}} = \frac{a}{4}\left(1 + \frac{15}{32}a^2 + \frac{315}{1024}a^4 \cdots\right) , \tag{7.2b}$$

$$f_2(a)=\int_0^{2\pi}\frac{d\theta}{2\pi}\frac{1}{\sqrt{1-a\cos(\theta)}}=\left(1+\frac{3}{16}a^2+\frac{105}{1024}a^4+\frac{1155}{16384}a^6+\cdots\right), \tag{7.2c}$$

$$f_3(a)=\int_0^{2\pi}\frac{d\theta}{2\pi}\frac{\cos(\theta)}{\sqrt{1-a\cos(\theta)}^3}=\frac{3a}{4}\left(1+\frac{35}{32}a^2+\frac{1155}{1024}a^4+\cdots\right), \tag{7.2d}$$

$$f_4(a)=\int_0^{2\pi}\frac{d\theta}{2\pi}\frac{1}{\sqrt{1-a\cos(\theta)}^3}=\left(1+\frac{15}{16}a^2+\frac{945}{1024}a^4+\frac{15015}{16384}a^6\cdots\right). \tag{7.2e}$$

These expansions suggest that f_1 and f_2 diverge as Log $\left(1-a^2\right)$, while f_3 and f_4 diverge as $1/\left(1-a^2\right)$. This behavior is quantified below and accurate approximate formulas are found that are valid through the entire range $0\le a\le 1$.

8. Thin Wire Layer – Complete Solution

8.1 Semi-infinite layer

In section 4 we derived the on-axis field for a thin semi-infinite wire layer, which was then used to build up more complex layouts by shifting, i.e. $z\to z-z_0$, and adding layers:

$$J_\theta(r,z)=S\delta(r-R)H(-z), \tag{8.1}$$

$$B_0(z)=\frac{\mu_0 S}{2}\left(1-\frac{z}{\sqrt{z^2+R^2}}\right). \tag{8.2}$$

Near-axis field components, including the lowest order fringe field aberration, are

$$\begin{aligned}B_z&\approx B_0-\frac{B_0''r^2}{4}+\ldots\\&=\frac{\mu_0 S}{2}\left[1-\frac{z}{\sqrt{z^2+R^2}}-\frac{3}{4}\frac{R^2zr^2}{\sqrt{z^2+R^2}^5}+\ldots\right],\end{aligned} \tag{8.3a}$$

$$\begin{aligned}B_r&=-\frac{B_0'r}{2}+\frac{B_0'''r^3}{16}-\ldots\\&=\frac{\mu_0 S}{4}\left[\frac{R^2r}{\sqrt{z^2+R^2}^3}+\frac{3}{8}\frac{R^2\left(R^2-4z^2\right)r^3}{\sqrt{z^2+R^2}^7}+\ldots\right].\end{aligned} \tag{8.3b}$$

The near-axis results may be extended to any value of r using the Green function solutions. The resulting expressions involve only an integration over θ because the integrations over r' and z' are elementary. We have from eqns. (6.12) and (6.13):

$$B_z = \frac{\mu_0}{4\pi}\int_{-\infty}^{+\infty} dz' \int_0^{\infty} dr' r' \left[S\delta(r'-R)H(-z') \right] \int_0^{2\pi} d\theta \frac{r' - r\ \cos(\theta)}{\sqrt{(z'-z)^2 + r'^2 + r^2 - 2r'r\cos(\theta)}^3}$$

$$= \frac{\mu_0 S}{2}\int_0^{2\pi} \frac{d\theta}{2\pi} \int_{-\infty}^{0} dz' \frac{R^2 - Rr\ \cos(\theta)}{\sqrt{(z'-z)^2 + R^2 + r^2 - 2Rr\cos(\theta)}^3}$$

$$= \frac{\mu_0 S}{2}\int_0^{2\pi} \frac{d\theta}{2\pi} \left(\frac{R^2 - Rr\ \cos\theta}{R^2 + r^2 - 2Rr\cos\theta} \right) \left[1 - \frac{z}{\sqrt{z^2 + R^2 + r^2 - 2Rr\cos(\theta)}} \right] , \qquad (8.4a)$$

$$B_r = \frac{-\mu_0}{4\pi}\int_{-\infty}^{\infty} dz' \int_0^{\infty} dr' r' \left[\frac{\partial}{\partial z'} S\delta(r'-R)H(-z') \right] \int_0^{2\pi} d\theta \frac{\cos(\theta)}{\sqrt{(z'-z)^2 + r'^2 + r^2 - 2r'r\cos(\theta)}}$$

$$= \frac{\mu_0 S}{2}\int_0^{2\pi} \frac{d\theta}{2\pi} \frac{R\ \cos(\theta)}{\sqrt{z^2 + R^2 + r^2 - 2Rr\cos(\theta)}} \ . \qquad (8.4b)$$

The first integral in eqn. (8.4a) for B_z is simply

$$\int_0^{2\pi} \frac{d\theta}{2\pi} \ \frac{R^2 - Rr\ \cos(\theta)}{R^2 + r^2 - 2Rr\cos(\theta)} = H(R-r) \ , \qquad (8.5)$$

so we find the expected limits

$$B_z \to \begin{cases} \mu_0 S H(R-r) & z \to -\infty \\ 0 & z \to +\infty \end{cases} , \qquad (8.6)$$

while at $z = 0$ there is the simple result

$$B_z = \frac{\mu_0 S}{2} H(R-r) \ . \qquad (8.7)$$

Equation (8.2) for $B_0(z)$ is recovered from eqn. (8.4a) by setting $r = 0$. For general (r,z) B_z does not appear to be expressible in terms of commonly used functions, but if we insert $r = R$, then we obtain simply

$$B_z(R,z) = \frac{\mu_0 S}{4}\left[1 - \frac{z f_2\left(2R^2/\left(z^2+2R^2\right)\right)}{\sqrt{z^2+2R^2}}\right] . \qquad (8.8)$$

For $z<0$ this is the longitudinal field along the <u>center</u> of the thin wire layer. The longitudinal field immediately inside or outside the layer (denoted $r = R\pm$) is therefore

$$B_z(R\pm, z<0) = \frac{\mu_0 S}{4}\left[1 - \frac{z f_2\left(2R^2/\left(z^2+R^2\right)\right)}{\sqrt{z^2+2R^2}}\right] \mp \frac{\mu_0 S}{2} \quad , \qquad (8.9)$$

with f_2 defined in section (7):

$$f_2(a) = \int_0^{2\pi} \frac{d\theta}{2\pi} \frac{1}{\sqrt{1-a\cos(\theta)}} \ .$$

8.2 Wire end divergence

From equations (8.8) and (8.9) follows that very close to the wire layer ends $(r = R\pm, z = 0\pm)$, B_z is discontinuous as:

r	z	$B_z/\mu_0 S$
$R-$	$0-$	$3/4$
$R-$	$0+$	$1/4$
$R+$	$0-$	$-1/4$
$R+$	$0+$	$1/4$

This seemingly peculiar behavior is easily seen by a numerical evaluation of expression (8.4a) near the wire layer end. It can also be deduced from the behavior of B_r (see below) using the Maxwell equation $\vec{\nabla}\cdot\vec{B} = 0$.

Expression (8.4b) for B_r can be written in the compact form

$$B_r = \frac{\mu_0 S}{2} \ \frac{R}{\sqrt{z^2+r^2+R^2}} \ f_1(b) \ , \qquad (8.10)$$

with $b \equiv 2Rr/\left(z^2+r^2+R^2\right)$, and $f_1(b)$ defined in section 7 as:

$$f_1(b) = \int_0^{2\pi} \frac{d\theta}{2\pi} \frac{\cos(\theta)}{\sqrt{1 - b\cos(\theta)}} \quad . \tag{8.11}$$

Recall that as $b \to 1$,

$$f_1(b) \to \frac{C}{4b}\left[D - \mathrm{Log}\left(1 - b^2\right)\right], \tag{8.12}$$

where $C = 2\sqrt{2}/\pi$ and $D = \left(6\mathrm{Log}(2) - 4\right)$. It is apparent that B_r is weakly divergent at the wire layer end $(r = R, z = 0)$. Explicitly, using eqns. (8.10, 8.12),

$$B_r \to \frac{\mu_0 S}{4\pi}\left\{D - \mathrm{Log}\left[\frac{z^2 + (r-R)^2}{R^2}\right]\right\} . \tag{8.13}$$

Although B_r becomes infinite for an infinitesimally thin current layer, it is finite for a layer of finite thickness. In fact in a thin layer B_r exceeds the scale field strength $(\mu_0 S)$ only when $\sqrt{z^2 + (r-R)^2} \le R/400$. For thickness greater than $R/20$ the divergent behavior of the thin layer is not representative. Interestingly, the logarithmic divergence does have an effect in permanent magnets, which have essentially infinitesimal surface current layer thickness, which causes a partial demagnetization at magnet corners due to the non-ideal magnetization properties of the material.

For $|\vec{r}| >> R$, eqns. (8.4a,b) may be expanded in inverse powers of $|\vec{r}|$ to yield in leading order

$$\vec{B} \approx \mu_0 S H(R - r) H(-z)\hat{e}_z + \frac{\mu_0 S R^2 \vec{r}}{4|\vec{r}|^3} . \tag{8.14}$$

This is just a uniform direct field that terminates at $z = 0$ plus a residual "magnetic monopole field" with net flux $\pi R^2 \mu_0 S$ centered at $\vec{r} = 0$. A generalization of this result is presented in section 11.

8.3 Finite length lense

For a solenoid of finite length ℓ and wire radius R, centered at $z = 0$, equations (8.4a,b) give by translation and superposition

$$B_z = \frac{\mu_0 S}{2}\int_0^{2\pi}\frac{d\theta}{2\pi}\left[\frac{R^2 - Rr\ \cos(\theta)}{R^2 + r^2 - 2Rr\ \cos(\theta)}\right]$$

$$\bullet\ \left[\frac{(z+\ell/2)}{\sqrt{(z+\ell/2)^2 + r^2 + R^2 - 2Rr\ \cos(\theta)}} - \frac{(z-\ell/2)}{\sqrt{(z-\ell/2)^2 + r^2 + R^2 - 2Rr\cos(\theta)}}\right], \tag{8.15a}$$

$$B_r = \frac{\mu_0 S}{2}\int_0^{2\pi}\frac{d\theta}{2\pi}$$

$$\bullet\ \left[\frac{R\ \cos(\theta)}{\sqrt{(z-\ell/2)^2 + r^2 + R^2 - 2Rr\ \cos(\theta)}} - \frac{R\ \cos(\theta)}{\sqrt{(z+\ell/2)^2 + r^2 + R^2 - 2Rr\cos(\theta)}}\right]. \tag{8.15b}$$

Plots of B_z and B_r for several values of r are displayed below for a lense of length $\ell = 4.0\text{m}$ and wire radius $R = 1.0\text{m}$.

```
(*Field of a thin layer solenoid*)

(*mu0S = (4*Pi*10^-7)*(current layer density),
 R= radius to wire layer, l=wire layer length*)

mu0S = 1.0;
R = 1;
l = 4;

Bz[r_, z_] := mu0S / 2 * NIntegrate[l / 2 / Pi * (R^2 - R*r*Cos[x]) / (R^2 + r^2 - 2*R*r*Cos[x])
     ((z + l / 2) / ((z + l / 2)^2 + R^2 + r^2 - 2*R*r*Cos[x])^.5 -
       (z - l / 2) / ((z - l / 2)^2 + R^2 + r^2 - 2*R*r*Cos[x])^.5), {x, 0, 2*Pi}]

Br[r_, z_] :=
 mu0S / 2 * NIntegrate[l / 2 / Pi * (R*Cos[x] / ((z - l / 2)^2 + R^2 + r^2 - 2*R*r*Cos[x])^.5 -
      R*Cos[x] / ((z + l / 2)^2 + R^2 + r^2 - 2*R*r*Cos[x])^.5), {x, 0, 2*Pi}]
```

```
In[66]:= Plot[
          {Bz[0, z], Bz[.5*R, z], Bz[.9*R, z], Bz[1.1*R, z], Bz[1.5*R, z], Bz[2*R, z]}, {z, -l,
```

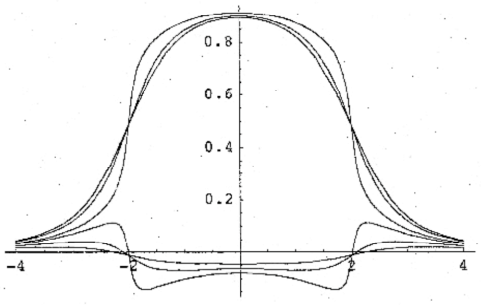


```
In[67]:= Plot[{Bz[.5*R, z], Bz[.9*R, z], Bz[1.1*R, z], Bz[1.5*R, z], Bz[2*R, z]}, {z, -l, l}];
```

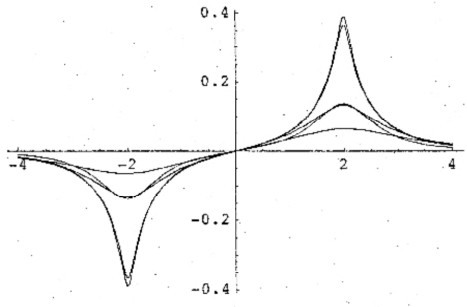

The vector potential of a finite length solenoid can also be expressed by a single integral over θ using the Green function (6.14):

$$A_\theta = \frac{\mu_0}{4\pi}\int d^3r' \frac{J_\theta{}' \cos(\theta' - \theta)}{\left|\vec{r'} - \vec{r}\right|}$$

$$= \frac{\mu_0 SR}{4\pi}\int_0^{2\pi} d\theta \ \cos(\theta)\int_{-\ell/2}^{\ell/2} dz' \frac{1}{\sqrt{(z'-z)^2 + r^2 + R^2 - 2Rr\cos(\theta)}}$$

$$= \frac{\mu_0 SR}{2}\int_0^{2\pi} \frac{d\theta}{2\pi} \ \cos(\theta)\mathrm{Log}\left[\frac{\sqrt{(z-\ell/2)^2 + R^2 + r^2 - 2Rr\ \cos(\theta)} - (z-\ell/2)}{\sqrt{(z+\ell/2)^2 + R^2 + r^2 - 2Rr\ \cos(\theta)} - (z+\ell/2)}\right] . \quad (8.16)$$

Equation (6.20) gives the alternative, equivalent form

$$A_\theta = \frac{\mu_0 SR^2 r}{2}\int_0^{2\pi} \frac{d\theta}{2\pi} \frac{\sin^2(\theta)}{R^2 + r^2 - 2Rr\cos(\theta)}$$

$$\cdot\left[\frac{(z+\ell/2)}{\sqrt{(z+\ell/2)^2 + R^2 + r^2 - 2Rr\cos(\theta)}} - \frac{(z-\ell/2)}{\sqrt{(z-\ell/2)^2 + R^2 + r^2 - 2Rr\cos(\theta)}}\right] . \quad (8.17)$$

8.4 Stored energy

The magnetic field energy of a thin-layer lens is easily evaluated. In the absence of permeable materials we have in general,

$$W = \int d^3r \frac{\left|\vec{B}\right|^2}{2\mu_0} = \int d^3r \frac{\vec{B}\bullet\vec{\nabla}x\vec{A}}{2\mu_0} = \int d^3r \frac{\vec{A}\bullet\vec{\nabla}x\vec{B}}{2\mu_0} = \int d^3r \frac{\vec{A}\bullet\vec{J}}{2} \ . \quad (8.18)$$

For $J_\theta = S(z)\delta(r-R)$, eqn. (8.18) gives

$$W = \pi R\int dz \ S(z)A_\theta(R,z). \quad (8.19)$$

Inserting expression (8.17) for A_θ and working the elementary integrations in z gives for a lens of length ℓ:

$$W = \frac{\pi R^2 \ell (\mu_0 S)^2}{2\mu_0} \mathrm{f}(x) \ , \tag{8.20}$$

where $x = \ell^2 / 2R^2$ and

$$\mathrm{f}(x) = \frac{1}{\sqrt{x}} \int_0^{2\pi} \frac{d\theta}{2\pi} (1 + \cos(\theta)) \left[\sqrt{x + 1 - \cos(\theta)} - \sqrt{1 - \cos(\theta)} \right]. \tag{8.21}$$

This function can be expressed using the previously defined f_0 and f_3 (section 7):

$$f(x) = \sqrt{\frac{x+1}{x}} \left[f_0\left(\frac{1}{1+x}\right) - \frac{1}{3}\left(1 - \frac{1}{(1+x)^2}\right) f_3\left(\frac{1}{1+x}\right) \right] - \frac{2}{3}\frac{C}{\sqrt{x}} \ , \tag{8.22}$$

which slowly approaches unity for large x:

$$f(x) \to 1 - \frac{2}{3}\frac{C}{\sqrt{x}} + \frac{1}{4x} \ . \tag{8.23}$$

For very large $x >> 1$, i.e. $\ell >> \sqrt{2}R$, $\mathrm{f}(x) \to 1$ and expression (8.20) is just the energy one gets using only the direct field of the magnet bore. For $x > .2$, which covers all cases of practical interest,

$$\mathrm{f}(x) \approx \frac{1}{1 + \frac{.63}{\sqrt{x}}} \ , \tag{8.24}$$

with error less that 1%, so we have in general for the thin layer lens

$$W \approx \frac{\pi R^2 \ell (\mu_0 S)^2}{2\mu_0} \ \frac{1}{1 + .89\, R/\ell} \ . \tag{8.25}$$

It is somewhat surprising that the actual value of W for the finite-length lens is smaller than the approximate value found using only the direct field.

Suppose the current layer is made of n turns of wire carrying current I. Then $S = n\mathrm{I}/\ell$ and the magnet's inductance is

$$L = \frac{2W}{\mathrm{I}^2} \approx \frac{\mu_0 n^2 \pi R^2 / \ell}{1 + .89\, R/\ell} \ .$$

(8.26)

```
In[77]:= (*plots of fi[a]*)

         f0[a_] := NIntegrate[1 / 2 / Pi * (1 - a * Cos[x]) ^ .5, {x, 0, 2 * Pi}]
         f1[a_] := NIntegrate[1 / 2 / Pi * Cos[x] / (1 - a * Cos[x]) ^ .5, {x, 0, 2 * Pi}]
         f2[a_] := NIntegrate[1 / 2 / Pi / (1 - a * Cos[x]) ^ .5, {x, 0, 2 * Pi}]
         f3[a_] := NIntegrate[1 / 2 / Pi * Cos[x] / (1 - a * Cos[x]) ^ 1.5, {x, 0, 2 * Pi}]
         f4[a_] := NIntegrate[1 / 2 / Pi / (1 - a * Cos[x]) ^ 1.5, {x, 0, 2 * Pi}]

In[76]:= Plot[f0[a], {a, 0, 1}, PlotPoints → 200];
```

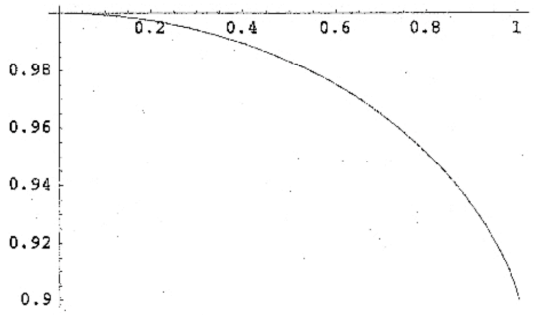


```
In[75]:= Plot[{f1[a], f2[a]}, {a, 0, .9995}, PlotPoints → 200];
```

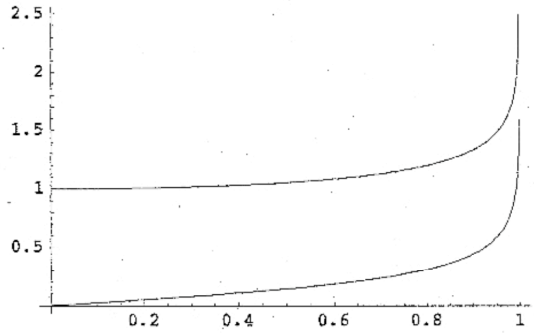


```
In[74]:= Plot[{f3[a], f4[a]}, {a, 0, .95}, PlotPoints → 200];
```

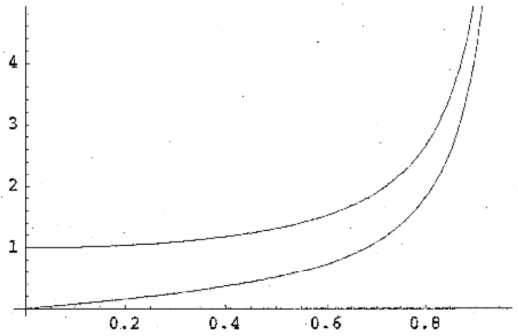

9. Thick Wire Layer

9.1 Uniform thick layer

While the thin wire layer formulas are sufficient for most beam dynamics applications, thick layer results are needed for precise near-axis fields, external fields, field in the wire, and mechanical stress. We first treat the case of radially uniform current density

$$J_\theta = \frac{S(z)}{R_2 - R_1} \qquad (R_1 < r < R_2) \ . \tag{9.1}$$

As in section 4, it is usually sufficient to derive the field for a semi-infinite thick layer, $S(z) = SH(-z)$, and any system of lenses may be built up from this by offsets $(z \to z - z_0)$ and super-position.

Recall from section 8 the semi-infinite thin layer field $\left[J_\theta = SH(-z)\delta(r-R)\right]$:

$$B_z^{\text{thin}} = \frac{\mu_0 S}{2}\int_0^{2\pi}\frac{d\theta}{2\pi}\frac{R^2 - Rr\cos(\theta)}{R^2 + r^2 - 2Rr\cos(\theta)}\left[1 - \frac{z}{\sqrt{z^2 + R^2 + r^2 - 2Rr\cos(\theta)}}\right], \tag{9.2a}$$

$$B_r^{\text{thin}} = \frac{\mu_0 S}{2}\int_0^{2\pi}\frac{d\theta}{2\pi}\frac{R\cos(\theta)}{\sqrt{z^2 + R^2 + r^2 - 2Rr\cos(\theta)}}. \tag{9.2b}$$

For the thick, uniform, semi-infinite layer we simply compute a radial superposition of these thin layer fields:

$$(B_z, B_r)^{\text{thick}} = \int_{R_1}^{R_2}\frac{dR}{R_2 - R_1}(B_z, B_r)^{thin} \ . \tag{9.3}$$

The on-axis field of the semi-infinite thick layer is

$$\begin{aligned} B_0^{\text{thick}}(z) &= \int_{R_1}^{R_2}\frac{dR}{R_2 - R_1}\ \frac{\mu_0 S}{2}\left(1 - \frac{z}{\sqrt{z^2 + R^2}}\right) \\ &= \frac{\mu_0 S}{2}\left[1 - \frac{z}{R_2 - R_1}\text{Log}\left(\frac{R_2 + \sqrt{z^2 + R_2^2}}{R_1 + \sqrt{z^2 + R_1^2}}\right)\right] \ . \end{aligned} \tag{9.4}$$

As mentioned in section 4, for a thick-layer lens of length ℓ centered at $z = 0$, the on-axis field is

$$B_0^{\text{Lens}}(z) = \frac{\mu_0 S}{2(R_2 - R_1)}\left\{\left(\frac{\ell}{2} + z\right)\text{Log}\left[\frac{R_2 + \sqrt{\left(\frac{\ell}{2} + z\right)^2 + R_2^2}}{R_1 + \sqrt{\left(\frac{\ell}{2} + z\right)^2 + R_1^2}}\right]\right.$$
$$\left. + \left(\frac{\ell}{2} - z\right)\text{Log}\left[\frac{R_2 + \sqrt{\left(\frac{\ell}{2} - z\right)^2 + R_2^2}}{R_1 + \sqrt{\left(\frac{\ell}{2} - z\right)^2 + R_1^2}}\right]\right\} . \tag{9.5}$$

Near-axis values of B_z and B_r can then be obtained using these results and the radial expansions of section 3. For the field at the magnet center $(z = 0)$, eqn. (9.5) reduces to

$$B_0^{\text{Lens}}(0) = \frac{\mu_0 S \ell}{2(R_2 - R_1)}\text{Log}\left(\frac{R_2 + \sqrt{\ell^2/4 + R_2^2}}{R_1 + \sqrt{\ell^2/4 + R_1^2}}\right) . \tag{9.6}$$

The semi-infinite, thick-layer formulas for B_z and B_r at general (r,z) can also be written in terms of integrations over θ. The integrals over R in eqn. (9.3) can actually be evaluated in terms of elementary functions, although the results are somewhat messy. First we define

$$u(r,\theta) = R_1 - r\ \cos(\theta),\ \ v(r,\theta) = R_2 - r\ \cos(\theta) . \tag{9.7a,b}$$

Then, using the integrals given at the end of section 3 and omitting some intermediate steps, we get from eqns. (9.2, 9.3):

$$B_r^{\text{thick}} = \frac{\mu_0 S}{2(R_2 - R_1)}\int_0^{2\pi}\frac{d\theta}{2\pi}\cos(\theta)\left\{\sqrt{v^2 + z^2 + r^2\sin^2(\theta)}\right.$$
$$\left. - \sqrt{u^2 + z^2 + r^2\sin^2(\theta)} + r\cos(\theta)Log\left[\frac{v + \sqrt{v^2 + z^2 + r^2\sin^2(\theta)}}{u + \sqrt{u^2 + z^2 + r^2\sin^2(\theta)}}\right]\right\} , \tag{9.8}$$

$$B_z^{\text{thick}} = \frac{\mu_0 S(r)}{2} - \frac{\mu_0 S z}{2(R_2 - R_1)} \int_0^{2\pi} \frac{d\theta}{2\pi} \left\{ Log\left[\frac{v + \sqrt{v^2 + z^2 + r^2 \sin^2(\theta)}}{u + \sqrt{u^2 + z^2 + r^2 + \sin^2(\theta)}} \right] \right.$$

$$- \left(\frac{r \cos(\theta)}{z} \right) \left[\tanh^{-1} \left(\frac{\sqrt{v^2 + z^2 + r^2 \sin^2(\theta)}}{z} \right) - \tanh^{-1} \left(\frac{\sqrt{u^2 + z^2 + r^2 \sin^2(\theta)}}{z} \right) \right]$$

$$\left. - \left(\frac{r \sin(\theta)}{z} \right) \left[\tan^{-1} \left(\frac{z}{r \sin(\theta)} \frac{v}{\sqrt{v^2 + z^2 + r^2 \sin^2(\theta)}} \right) - \tan^{-1} \left(\frac{z}{r \sin(\theta)} \frac{u}{\sqrt{u^2 + z^2 + r^2 \sin^2(\theta)}} \right) \right] \right\}. \tag{9.9}$$

Here we have used

$$S(r) = \begin{cases} S & 0 < r < R_1 \\ S \dfrac{R_2 - r}{R_2 - R_1} & R_1 < r < R_2 \\ 0 & R_2 < r \quad . \end{cases} \tag{9.10}$$

9.2 Approximation by a thin layer

It was asserted in section 4 that the on-axis field of a thin layer magnet, with small error could replace the on-axis field of a uniform thick layer magnet. There are many ways to select the three parameters (S, R, ℓ) of the thin layer. Here we use the same S and ℓ as the thick layer and set R to give the correct net magnetic dipole moment by requiring

$$\mathrm{SR}^2 = \int_0^\infty dr J_\theta r^2 = \int_{R_1}^{R_2} dr \frac{S}{R_2 - R_1} r^2 = \frac{S}{3} \left(R_2^2 + R_2 R_1 + R_1^2 \right). \tag{9.11}$$

Defining a thickness parameter

$$\Delta \equiv (R_2 - R_1)/R \ , \tag{9.12}$$

we have from eqn. (9.11)

$$R_1 = R\left(\sqrt{1 - \frac{\Delta^2}{12}} - \frac{\Delta}{2} \right), \ R_2 = R\left(\sqrt{1 - \frac{\Delta^2}{12}} + \frac{\Delta}{2} \right). \tag{9.13a,b}$$

We require that $\Delta < \sqrt{3}$ to prevent $R_1 < 0$. A somewhat different formula for R is obtained if we equate the focal lengths of the magnets $\left(f^{-1} \sim \int dz B_0^2(z)\right)$. The following table gives the maximum ratio of on-axis fields for the thin layer eqn. (4.6), relative to the equivalent thick layer eqn. (9.5), for various values of Δ and ℓ/R. Except for very small ℓ/R this maximum occurs in the fringe at $z \approx \pm(\ell/2 + .8R)$.

ℓ/R	B_0^{thin}/B_0^{thick} $\Delta = .1$	$\Delta = .2$	$\Delta = .5$	$\Delta = 1.0$
1	1.00094	1.0038	1.024	1.101
2	1.00088	1.0035	1.023	1.094
4	1.00082	1.0033	1.021	1.087
8	1.00079	1.0032	1.020	1.084
16	1.00078	1.0031	1.020	1.083

9.3 General thick layer

Finally we treat the thick wire layer with specified ends and general current density profile $J_\theta(r) = -dS(r)/dr$ between the ends. The Green function solutions of section 6 can be used for this, as can simple averages of eqns. (9.2). However, more useful expressions can be derived using the Bessel transform. First, the semi-infinite layer $J_\theta = J_\theta(r)H(-z)$ has $B_z(r, z \to -\infty) = \mu_0 S(r)$, and by symmetry

$$B_z(r, z = 0) = \frac{\mu_0 S(r)}{2} \ . \tag{9.14}$$

For $z > 0$,

$$B_z \sim J_0(kr)e^{-kz} \ , \tag{9.15}$$

with $k > 0$ is a valid solution of $\nabla^2 B_z = 0$, except for the boundary condition (9.14). The correct solution for $z \geq 0$ is given by the Bessel transform:

$$B_z(r, z \geq 0) = \frac{\mu_0}{2}\int_0^\infty dk \ \ kJ_0(kr)e^{-kz}\tilde{S}(k), \tag{9.16}$$

$$\tilde{S}(k) = \int_0^\infty dr \ \ rJ_0(kr)S(r) \ . \tag{9.17}$$

We denote the nth ordinary Bessel function by $J_n(x)$. A similar calculation gives

$$B_z(r, z \leq 0) = \mu_0 S(r) - \frac{\mu_0}{2}\int_0^\infty dk \ \ kJ_0(kr)e^{+kz}\tilde{S}(k) \ . \tag{9.18}$$

Combining these results we have for the entire semi-infinite layer:

$$B_z = \mu_0 S(r) H(-z) + \frac{z}{|z|}\frac{\mu_0}{2}\int_0^\infty dk \;\; k J_0(kr) e^{-k|z|}\tilde{S}(k) \; . \tag{9.19}$$

$\vec{B}$ can also be derived from the modified scalar potential (see section 5):

$$B_z(r,z) = \mu_0 S(r) H(-z) + \partial\varphi/\partial z \; . \tag{9.20}$$

Equation (9.19) then gives for φ and B_r:

$$\varphi(r,z) = -\frac{\mu_0}{2}\int_0^\infty dk \;\; J_0(kr) e^{-k|z|}\tilde{S}(k) \; , \tag{9.21}$$

$$B_r(r,z) = \frac{\partial\varphi}{\partial r} = \frac{\mu_0}{2}\int_0^\infty dk \;\; k J_1(kr) e^{-k|z|}\tilde{S}(k) \; . \tag{9.22}$$

Using superposition, a lens of length ℓ, centered at $z = 0$ is seen to have fields

$$\begin{aligned} B_z(r,z) &= \mu_0 S(r)\left[H(-z+\ell/2) - H(-z-\ell/2)\right] \\ &+ \frac{\mu_0}{2}\int_0^\infty dk \;\; k J_0(kr)\tilde{S}(k)\left[\frac{(z-\ell/2)}{|z-\ell/2|}e^{-k|z-\ell/2|} - \frac{(z+\ell/2)}{|z+\ell/2|}e^{-k|z+\ell/2|}\right] \; , \end{aligned} \tag{9.23}$$

$$B_r(r,z) = \frac{\mu_0}{2}\int_0^\infty dk \;\; k J_1(kr)\tilde{S}(k)\left[e^{-k|z-\ell/2|} - e^{-k|z+\ell/2|}\right] . \tag{9.24}$$

It remains to evaluate $\tilde{S}(k)$. First we integrate by parts in eqn. (9.17) using $J_\theta = -dS(r)/dr$:

$$\tilde{S}(k) = \int_0^\infty dr S(r)\frac{\partial}{\partial r}\frac{rJ_1(kr)}{k} = \int_0^\infty dr J_\theta(r)\frac{rJ_1(kr)}{k} \; . \tag{9.25}$$

<u>Case 1</u> (thin layer):

$$J_\theta(r) = S\delta(r-R) \; , \tag{9.26}$$

$$\tilde{S} = \frac{RSJ_1(kR)}{k} \; . \tag{9.27}$$

<u>Case 2</u> (J_θ decreasing with r):

$$J_\theta(r) = \frac{S}{r \;\; \mathrm{Log}(R_2/R_1)} \qquad R_1 < r < R_2 \; , \tag{9.28}$$

$$\tilde{S}(k) = \frac{S}{k^2 \ \mathrm{Log}(R_2/R_1)}\left[J_0(kR_1) - J_0(kR_2)\right] . \tag{9.29}$$

Case 3 (uniform thick layer):

$$J_\theta = \frac{S}{R_2 - R_1} \qquad R_1 < r < R_2 , \tag{9.30}$$

$$\tilde{S}(k) = \frac{S}{k^3(R_2 - R_1)} \int_{kR_1}^{kR_2} dy y J_1(y) \ . \tag{9.31}$$

The integration over y, although not elementary, can be expressed as a hypergeometric function:

$$\int_0^x dy y J_1(y) = \frac{x^3}{6} {}_1F_2\left(\frac{3}{2};2,\frac{5}{2};-x^2/4\right) \ . \tag{9.32}$$

In Mathematica® notation

$${}_1F_2(a;b,c;z) = \text{Hypergeometic PFQ}\left[\{\text{a}\},\{b,c\},z\right] \tag{9.33}$$

$$= 1 + \frac{a}{bc}\frac{z}{1!} + \frac{a(a+1)}{b(b+1)c(c+1)}\frac{z^2}{2!} + \ldots . \tag{9.34}$$

Equation (9.31) becomes

$$\tilde{S}(k) = \frac{S}{6(R_2 - R_1)} \left[R_2^3 \ {}_1F_2\left(\frac{3}{2};2,\frac{5}{2};-\frac{k^2R_2^2}{4}\right) - R_1^3 \ {}_1F_2\left(\frac{3}{2};2,\frac{5}{2};\frac{-k^2R_1^2}{4}\right)\right] . \tag{9.35}$$

10. Periodic Thin Wire Layer

The field of an infinite, periodic wire layer is of interest for beam transport. Its external field is very different from that of an isolated magnet, particularly at large r, where it falls off exponentially rather than as r^{-3}. The return flux is diluted to zero intensity in this case.

Let ℓ denote an individual solenoid's wire layer length and g denote gap lengths between adjacent wire layers. Assuming the solenoids all have the same polarity, the lattice period length is $P = \ell + g$. For one magnet of the lattice we set

$$J_\theta = S\delta(r - R) \qquad \text{for} \quad -\frac{\ell}{2} < z < \frac{\ell}{2} \ , \tag{10.1}$$

and extend this layer periodically. Then the Fourier expansion of $S(z)$ with period P is

$$S(z) = \frac{S\ell}{P} + \sum_{n=1}^{\infty} S_n \cos\left(\frac{2\pi n z}{P}\right) , \tag{10.2}$$

with

$$S_n = \frac{2S}{\pi n}\sin\left(\frac{\pi n \ell}{P}\right) . \tag{10.3}$$

The longitudinal field can be similarly expanded:

$$B_z = \mu_0 S \frac{\ell}{P} H(R - r) + \sum_{n=1}^{\infty} B_n(r)\cos\left(\frac{2\pi n z}{P}\right) , \tag{10.4}$$

with

$$B_n(r) = (\mu_0 S)\sin\left(\frac{\pi n \ell}{P}\right)\left(\frac{4R}{P}\right)K_1\left(\frac{2\pi n R}{P}\right)I_0\left(\frac{2\pi n r}{P}\right) \qquad 0 < r < R \ , \tag{10.5a}$$

$$B_n(r) = -(\mu_0 S)\sin\left(\frac{\pi n \ell}{P}\right)\left(\frac{4R}{P}\right)I_1\left(\frac{2\pi n R}{P}\right)K_0\left(\frac{2\pi n r}{P}\right) \qquad R < r < \infty \ , \tag{10.5b}$$

where I_n and K_n are modified Bessel functions of the first and second kind. The functions $B_n(r)$ satisfy

$$\frac{1}{r}\frac{\partial}{\partial r} r \frac{\partial B_n}{\partial r} - \left(\frac{2\pi n}{P}\right)^2 B_n = -\mu_0 S_n \frac{1}{r}\frac{\partial}{\partial r} r\delta(r - R) \ . \tag{10.6}$$

We have used the jump conditions for $B_n(r)$ at R, which may be derived from eqn. (10.6):

$$B_n(R+) - B_n(R-) = -\mu_0 S_n \ , \tag{10.7a}$$

$$\frac{\partial B_n}{\partial r}(R+) - \frac{\partial B_n}{\partial r}(R-) = 0\,, \tag{10.7b}$$

and the Wronskian identity,

$$I_0(x)K_1(x) + I_1(x)K_0(x) = \frac{1}{x}\,.$$

In similar fashion we find

$$B_r = \sum_{n=1}^{\infty} C_n(r)\sin\left(\frac{2\pi n z}{P}\right)\,, \tag{10.8}$$

$$C_n(r) = (\mu_0 S)\sin\left(\frac{\pi n \ell}{P}\right)\left(\frac{4R}{P}\right)K_1\left(\frac{2\pi n R}{P}\right)I_1\left(\frac{2\pi n r}{P}\right) \qquad 0 < r < R\,, \tag{10.9a}$$

$$C_n(r) = (\mu_0 S)\sin\left(\frac{\pi n \ell}{P}\right)\left(\frac{4R}{P}\right)I_1\left(\frac{2\pi n R}{P}\right)K_1\left(\frac{2\pi n r}{P}\right) \qquad R < r < \infty\,. \tag{10.9b}$$

This solves $\vec{\nabla}\cdot\vec{B} = 0$ with B_z given above. The components $C_n(r)$ are continuous at $r = R$.

At large r the asymptotic expansion of $K_0\left(2\pi n\, r/P\right)$ yields

$$B_n \sim \frac{\exp\left(-2\pi n\, r/P\right)}{\sqrt{r}}\,, \tag{10.10}$$

showing the asserted exponential decrease of field strength outside the wire. However, the calculated net flux in this example is $\mu_0 S\pi R^2\, \ell/P$, so the return flux must be regarded as being diluted to zero magnitude. Plots of B_z and B_r at various r are presented below for the parameters:

$$\mu_0 S\frac{\ell}{P} = 10.0\text{T},\ \ R = .2\text{m},\ \ \ell = .8\text{m},\ \ g = .2\text{m},\ \ P = \ell + g = 1.0\text{m}.$$

A total of 200 terms are used in the Fourier expansion. Note that while B_z reaches ~7.0T in the gaps, it drops to less than 2.0T in the volume behind the wire where an induction core could be located. This calculation is modified in section 18 with the addition of a permeable yoke to reduce the external field.

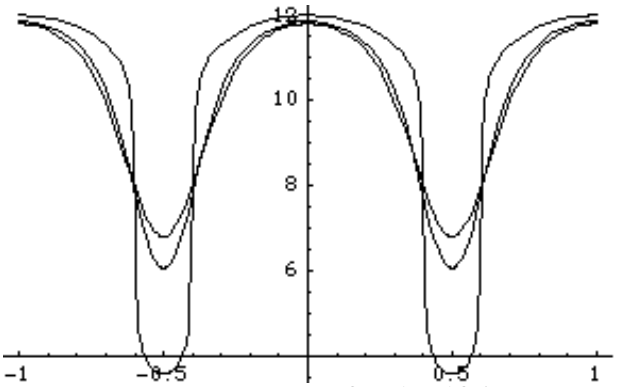

B_z vs z at $r = 0,\ .1,\ .195$

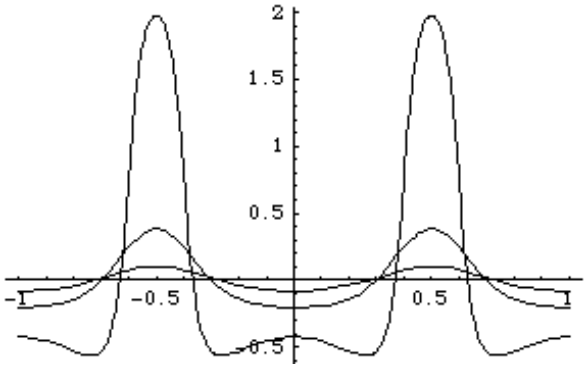

B_z vs z at $r = .25,\ .4,\ .55$

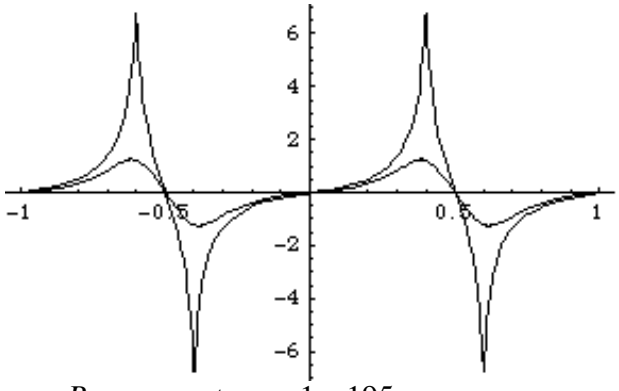

B_z vs z at $r = .1,\ .195$

11. <u>Far Field and External Field</u>

Because a solenoid system may have a large dipole moment, its field can interfere with nearby experiments and the operation of accelerator components. A short magnetic bend, which resembles a solenoid turned on its side, also has a net dipole moment, but a

permeable yoke is usually used to confine its return flux. This technique is not as effective for transport solenoids because the yoke must not block the vacuum bore. Also, if annular yokes are used in an induction linac they may considerably increase the diameter of adjacent induction cores and thereby increase the overall cost. It is possible to greatly reduce the far field by alternating the polarity of solenoid lenses, but this reduces their effectiveness for beam transport and actually increases the external field (just outside the wire). We are therefore motivated to evaluate the far and external fields in the absence of return flux confinement.

The far field and external field can be approximated using two different series expansions of the global potential φ. Both expansions may have contributions from several or many individual magnets, so it may be misleading to consider only one magnet at a time. Recall from section 5,

$$\vec{B} = \mu_0 S(r,z)\hat{e}_z + \vec{\nabla}\varphi, \tag{11.1}$$

where S(r,z) is the cumulative surface current density:

$$S(r,z) = \int_r^\infty dr' J_\theta(r',z). \tag{11.2}$$

The Green function solution for φ is, from section (6):

$$\varphi = \frac{\mu_0}{4\pi}\int_{-\infty}^{+\infty} dz' \int_0^\infty dr' r' \int_0^{2\pi} d\theta' \frac{\partial S'}{\partial z'} \frac{1}{\sqrt{(z'-z)^2 + r'^2 + r^2 - 2r'r\cos(\theta'-\theta)}}. \tag{11.3}$$

11.1 Far field expansion

Consider first the far field expansion in inverse powers of $|\vec{r}| = (r^2 + z^2)^{1/2}$, with r and z both considered to be large of order $|\vec{r}|$, which is larger than $|\vec{r'}|$. We could laboriously expand $|\vec{r'} - \vec{r}|^{-1}$ in inverse powers of $|\vec{r}|$, work the elementary integrals over θ', and gather terms of the same order. Fortunately this task has already been done for us in texts that treat electrostatics using spherical harmonics. For $|\vec{r}| > |\vec{r'}|$,

$$\int_0^{2\pi} \frac{d\theta}{2\pi} \frac{1}{|\vec{r'} - \vec{r}|} = \sum_{n=0}^{\infty} \frac{|\vec{r'}|^n}{|\vec{r}|^{n+1}} P_n(\cos\psi) P_n(\cos\psi'), \tag{11.4}$$

where

$$\cos(\psi) \equiv \frac{z}{|\vec{r}|}, \qquad \cos(\psi') \equiv \frac{z'}{|\vec{r'}|}, \tag{11.5}$$

and the P_n are the Legendre polynomials:

$$\begin{aligned} P_0(x) &= 1, \\ P_1(x) &= x, \\ P_2(x) &= \left(3x^2 - 1\right)/2, \\ P_3(x) &= \left(5x^3 - 3x\right)/2, \\ P_4(x) &= \left(35x^4 - 30x^2 + 3\right)/8, \ \text{etc}. \end{aligned} \tag{11.6}$$

Inserting expression (11.4) into eqn. (11.3) gives

$$\varphi = \frac{\mu_0}{2}\int_{-\infty}^{+\infty} dz' \int_0^{\infty} dr' r' \frac{\partial S'}{\partial z'} \left\{ \frac{1}{\left|\vec{r}\right|} + \frac{z'z}{\left|\vec{r}\right|^3} + \frac{\left(2z^2 - r^2\right)\left(2z'^2 - r'^2\right)}{4\left|\vec{r}\right|^5} + \frac{\left(2z^3 - 3zr^2\right)\left(2z'^3 - 3z'r'^2\right)}{4\left|\vec{r}\right|^7} + \ldots \right\}. \tag{11.7}$$

The leading (monopole) term vanishes after integration by parts in z' unless S' does not vanish as $\left|z'\right| \to \infty$:

$$\varphi = -\frac{\mu_0}{2}\int_{-\infty}^{+\infty} dz' \int_0^{\infty} dr' r' S' \left\{ \frac{z}{\left|\vec{r}\right|^3} + \frac{\left(2z^2 - r^2\right)z'}{\left|\vec{r}\right|^5} + \frac{\left(2z^3 - 3zr^2\right)\left(6z'^2 - 3r'^2\right)}{4\left|\vec{r}\right|^7} + \ldots \right\} \tag{11.8}$$

$$= \varphi_{dipole} + \varphi_{quadrupole} + \varphi_{sextupole} + \cdots . \tag{11.9}$$

Equation (11-8) may be written in the compact form

$$\varphi = -\frac{\mu_0}{4\pi}\left[\frac{m_1 P_1(\cos\psi)}{\left|\vec{r}\right|^2} + \frac{m_2 P_2(\cos\psi)}{\left|\vec{r}\right|^3} + \frac{m_3 P_3(\cos\psi)}{\left|\vec{r}\right|^4} + \ldots \right], \tag{11.10}$$

where the m_i are the multipole moments:

$$m_1 = 2\pi\int_{-\infty}^{+\infty} dz \int_0^{\infty} dr r S(r,z) , \tag{11.11a}$$

$$m_2 = 2\pi\int_{-\infty}^{+\infty} dz \int_0^{\infty} dr r S(r,z)(2z) , \tag{11.11b}$$

$$m_3 = 2\pi\int_{-\infty}^{+\infty} dz\int_0^{\infty} drrS(r,z)\frac{3\left(2z^2 - r^2\right)}{2}\,, \tag{11.11c}$$

etc. Here m_1 is the dipole moment with the conventional definition given in section 2. The quadrupole (m_2) and sextupole (m_3) moments have been defined in a way that makes eqn. (11-10) simple in appearance. Their general tensor forms are unnecessary with solenoidal symmetry.

For the far field expansion to be useful we must specify a coordinate origin, which should be at the magnet system center in some weighted sense. For a single lens the origin would usually be at the lens center. More generally the quadrupole moment can usually be zeroed by the right choice of origin. However, if m_1 vanishes, then m_2 is independent of the coordinate origin. In this case m_3 may be made to vanish.

Using $\vec{B}^{residual} = \vec{\nabla}\varphi$, the dipole components of the far field are

$$B_r^{far} = -\frac{\partial}{\partial r}\frac{\mu_0}{4\pi}\frac{m_1 z}{\sqrt{r^2 + z^2}^3} = \frac{\mu_0}{4\pi}\frac{3m_1 zr}{\sqrt{r^2 + z^2}^5}, \tag{11.12a}$$

$$B_z^{far} = -\frac{\partial}{\partial z}\frac{\mu_0}{4\pi}\frac{m_1 z}{\sqrt{r^2 + z^2}^3} = +\frac{\mu_0}{4\pi}\frac{m_1(2z^2 - r^2)}{\sqrt{r^2 + z^2}^5}\,. \tag{11.12b}$$

11.2 External field expansion

To obtain an expansion for the external field we take $r' < r$, but make no assumption about z and z'. Then $r'r < (z'-z)^2 + r^2$ and we write equation (11.3) as

$$\varphi = \frac{\mu_0}{2}\int_{-\infty}^{+\infty} dz'\int_0^{\infty} dr'r'\frac{\partial S'}{\partial z'}\frac{1}{\sqrt{(z'-z)^2 + r^2}}\int_0^{2\pi}\frac{d\theta'}{2\pi}\frac{1}{\sqrt{1 - \left[\dfrac{2r'r\cos\theta' - r'^2}{(z'-z)^2 + r^2}\right]}} \tag{11.13}$$

$$= \frac{\mu_0}{2}\int_{-\infty}^{+\infty} dz'\int_0^{\infty} dr'r'\frac{\partial S'}{\partial z'}\frac{1}{\sqrt{(z'-z)^2 + r^2}}\int_0^{2\pi}\frac{d\theta'}{2\pi}\,\cdot$$
$$\left\{1 + \frac{1}{2}[...] + \frac{3}{8}[...]^2 + \frac{5}{16}[...]^3 + \frac{35}{128}[...]^4 + ...\right\}, \tag{11.14}$$

where $[...]$ denotes the bracketed expression in eqn. (11.13). After the integrals over θ' are worked and terms of like order in r' are grouped we have

$$\varphi = \frac{\mu_0}{2}\int_{-\infty}^{+\infty} dz' \int_0^{\infty} dr' r' \frac{\partial S'}{\partial z'} \bullet$$
$$\left\{ \frac{1}{\sqrt{(z'-z)^2 + r^2}} + r'^2 \left[-\frac{1}{2}\frac{1}{\sqrt{\ldots}^3} + \frac{3}{4}\frac{r^2}{\sqrt{\ldots}^5} \right] + r'^4 \left[\frac{3}{8}\frac{1}{\sqrt{\ldots}^5} - \frac{15}{8}\frac{r^2}{\sqrt{\ldots}^7} + \frac{105}{64}\frac{r^4}{\sqrt{\ldots}^9} \right] + \ldots \right\}. \tag{11.15}$$

The radial moments defined in section 2 may now be used:

$$S(z)\overline{r^2}(z) = 2\int dr' r' S(r', z) \ , \tag{11.16a}$$

$$S(z)\overline{r^4}(z) = 4\int dr' r'^3 S(r', z) \ , \tag{11.16b}$$

$$S(z)\overline{r^6}(z) = 6\int dr' r'^5 S(r', z) \ ; \tag{11.16c}$$

$$\varphi = \frac{\mu_0}{2}\int_{-\infty}^{+\infty} dz' \left\{ \left[\frac{\partial}{\partial z'} \frac{S(z')\overline{r^2}(z')}{2} \right] \bullet \frac{1}{\sqrt{(z'-z)^2 + r^2}} + \left[\frac{\partial}{\partial z'} \frac{S(z')\overline{r^4}(z')}{4} \right] \bullet \right.$$
$$\left. \left[-\frac{1}{2}\frac{1}{\sqrt{\ldots}^3} + \frac{3}{4}\frac{r^2}{\sqrt{\ldots}^5} \right] + \left[\frac{\partial}{\partial z'} \frac{S(z')\overline{r^6}(z')}{6} \right] \bullet \left[\frac{3}{8}\frac{1}{\sqrt{\ldots}^5} - \frac{15}{8}\frac{r^2}{\sqrt{\ldots}^7} + \frac{105}{64}\frac{r^4}{\sqrt{\ldots}^9} \right] + \ldots \right\}. \tag{11.17}$$

This series appears to be complicated, but in fact we have again generated Legendre polynomials. Let

$$\cos(\gamma) \equiv \frac{(z'-z)}{\sqrt{(z'-z)^2 + r^2}} \ . \tag{11.18}$$

Then eqn. (11.17) may be written

$$\varphi = \frac{\mu_0}{2}\int_{-\infty}^{+\infty} dz' \left\{ \frac{P_0(\cos\gamma)}{\sqrt{(z'-z)^2 + r^2}} \left[\frac{\partial}{\partial z'} \frac{S(z')\overline{r^2(z')}}{2} \right] \right.$$
$$\left. - \frac{1}{2}\frac{P_2(\cos\gamma)}{\sqrt{\ldots}^3} \left[\frac{\partial}{\partial z'} \frac{S(z')\overline{r^4(z')}}{4} \right] + \frac{3}{8}\frac{P_4(\cos\gamma)}{\sqrt{\ldots}^5} \left[\frac{\partial}{\partial z'} \frac{S(z')\overline{r^6(z')}}{6} \right] + \ldots \right\} \ . \tag{11.19}$$

We treat the semi-infinite distribution

$$S(r,z) = S(r)H(-z), \tag{11.20}$$

with $S(r=0) \equiv S$ and $|\vec{r}| \equiv \sqrt{r^2 + z^2}$; from eqn. (11.17):

$$\varphi = \frac{-\mu_0 S}{2}\left\{\frac{\overline{r^2}}{2}\frac{1}{|\vec{r}|} + \frac{\overline{r^4}}{4}\left[\frac{-1}{2|\vec{r}|^3} + \frac{3r^2}{4|\vec{r}|^5}\right] + \frac{\overline{r^6}}{6}\left[\frac{3}{8|\vec{r}|^5} - \frac{15r^2}{8|\vec{r}|^7} + \frac{105r^4}{64|\vec{r}|^9}\right] + \ldots\right\}. \tag{11.21}$$

These are monopole, quadrupole, octopole, etc. terms. For a thin annular layer at radius R,

$$\overline{r^2} = R^2, \quad \overline{r^4} = R^4, \quad \overline{r^6} = R^6, \ldots . \tag{11.22}$$

For a uniform thick layer ($R_1 \le r \le R_2$),

$$\overline{r^2} = \frac{R_2^3 - R_1^3}{3(R_2 - R_1)}, \quad \overline{r^4} = \frac{R_2^5 - R_1^5}{5(R_2 - R_1)}, \quad \overline{r^6} = \frac{R_2^7 - R_1^7}{7(R_2 - R_1)}, \ldots . \tag{11.23}$$

The leading (monopole) term of eqn. (11.21) gives

$$\vec{B}^{ex} = \vec{\nabla}\varphi \approx \frac{\mu_0 S \overline{r^2}}{4}\frac{\vec{r}}{|\vec{r}|^3} = (\text{direct} \quad \text{flux}) \cdot \frac{\vec{r}}{4\pi|\vec{r}|^3}, \tag{11.24}$$

as expected.

11. Far Field and External Field

Because a solenoid system may have a large dipole moment, its field can interfere with nearby experiments and the operation of accelerator components. A short magnetic bend, which resembles a solenoid turned on its side, also has a net dipole moment, but a permeable yoke is usually used to confine its return flux. This technique is not as effective for transport solenoids because the yoke must not block the vacuum bore. Also, if annular yokes are used in an induction linac they may considerably increase the diameter of adjacent induction cores and thereby increase the overall cost. It is possible to greatly reduce the far field by alternating the polarity of solenoid lenses, but this reduces their effectiveness for beam transport and actually increases the external field (just outside the wire). We are therefore motivated to evaluate the far and external fields in the absence of return flux confinement.

The far field and external field can be approximated using two different series expansions of the global potential φ. Both expansions may have contributions from

several or many individual magnets, so it may be misleading to consider only one magnet at a time. Recall from section 5,

$$\vec{B} = \mu_0 S(r,z)\hat{e}_z + \vec{\nabla}\varphi, \tag{11.1}$$

where S(r,z) is the cumulative surface current density:

$$S(r,z) = \int_r^\infty dr' J_\theta(r',z). \tag{11.2}$$

The Green function solution for φ is, from section (6):

$$\varphi = \frac{\mu_0}{4\pi}\int_{-\infty}^{+\infty} dz' \int_0^\infty dr' r' \int_0^{2\pi} d\theta' \frac{\partial S'}{\partial z'} \frac{1}{\sqrt{(z'-z)^2 + r'^2 + r^2 - 2r'r\cos(\theta'-\theta)}}. \tag{11.3}$$

11.1 Far field expansion

Consider first the far field expansion in inverse powers of $|\vec{r}| = (r^2 + z^2)^{1/2}$, with r and z both considered to be large of order $|\vec{r}|$, which is larger than $|\vec{r'}|$. We could laboriously expand $|\vec{r'} - \vec{r}|^{-1}$ in inverse powers of $|\vec{r}|$, work the elementary integrals over θ', and gather terms of the same order. Fortunately this task has already been done for us in texts that treat electrostatics using spherical harmonics. For $|\vec{r}| > |\vec{r'}|$,

$$\int_0^{2\pi} \frac{d\theta}{2\pi} \frac{1}{|\vec{r'} - \vec{r}|} = \sum_{n=0}^\infty \frac{|\vec{r'}|^n}{|\vec{r}|^{n+1}} P_n(\cos\psi) P_n(\cos\psi'), \tag{11.4}$$

where

$$\cos(\psi) \equiv \frac{z}{|\vec{r}|}, \qquad \cos(\psi') \equiv \frac{z'}{|\vec{r'}|}, \tag{11.5}$$

and the P_n are the Legendre polynomials:

$$\begin{aligned} P_0(x) &= 1, \\ P_1(x) &= x, \\ P_2(x) &= (3x^2 - 1)/2, \\ P_3(x) &= (5x^3 - 3x)/2, \\ P_4(x) &= (35x^4 - 30x^2 + 3)/8, \text{ etc.} \end{aligned} \tag{11.6}$$

Inserting expression (11.4) into eqn. (11.3) gives

$$\varphi = \frac{\mu_0}{2}\int_{-\infty}^{+\infty} dz' \int_0^{\infty} dr' r' \frac{\partial S'}{\partial z'} \left\{ \frac{1}{\left|\vec{r}\right|} + \frac{z'z}{\left|\vec{r}\right|^3} + \frac{\left(2z^2 - r^2\right)\left(2z'^2 - r'^2\right)}{4\left|\vec{r}\right|^5} + \frac{\left(2z^3 - 3zr^2\right)\left(2z'^3 - 3z'r'^2\right)}{4\left|\vec{r}\right|^7} + \ldots \right\}. \tag{11.7}$$

The leading (monopole) term vanishes after integration by parts in z' unless S' does not vanish as $\left|z'\right| \to \infty$:

$$\varphi = -\frac{\mu_0}{2}\int_{-\infty}^{+\infty} dz' \int_0^{\infty} dr' r' S' \left\{ \frac{z}{\left|\vec{r}\right|^3} + \frac{\left(2z^2 - r^2\right)z'}{\left|\vec{r}\right|^5} + \frac{\left(2z^3 - 3zr^2\right)\left(6z'^2 - 3r'^2\right)}{4\left|\vec{r}\right|^7} + \ldots \right\} \tag{11.8}$$

$$= \varphi_{dipole} + \varphi_{quadrupole} + \varphi_{sextupole} + \cdots . \tag{11.9}$$

Equation (11-8) may be written in the compact form

$$\varphi = -\frac{\mu_0}{4\pi}\left[\frac{m_1 P_1(\cos\psi)}{\left|\vec{r}\right|^2} + \frac{m_2 P_2(\cos\psi)}{\left|\vec{r}\right|^3} + \frac{m_3 P_3(\cos\psi)}{\left|\vec{r}\right|^4} + \ldots \right], \tag{11.10}$$

where the m_i are the multipole moments:

$$m_1 = 2\pi\int_{-\infty}^{+\infty} dz \int_0^{\infty} dr r S(r,z) , \tag{11.11a}$$

$$m_2 = 2\pi\int_{-\infty}^{+\infty} dz \int_0^{\infty} dr r S(r,z)(2z) , \tag{11.11b}$$

$$m_3 = 2\pi\int_{-\infty}^{+\infty} dz \int_0^{\infty} dr r S(r,z)\frac{3\left(2z^2 - r^2\right)}{2} , \tag{11.11c}$$

etc. Here m_1 is the dipole moment with the conventional definition given in section 2. The quadrupole (m_2) and sextupole (m_3) moments have been defined in a way that makes eqn. (11-10) simple in appearance. Their general tensor forms are unnecessary with solenoidal symmetry.

For the far field expansion to be useful we must specify a coordinate origin, which should be at the magnet system center in some weighted sense. For a single lens

the origin would usually be at the lens center. More generally the quadrupole moment can usually be zeroed by the right choice of origin. However, if m_1 vanishes, then m_2 is independent of the coordinate origin. In this case m_3 may be made to vanish.

Using $\vec{B}^{residual} = \vec{\nabla}\varphi$, the dipole components of the far field are

$$B_r^{far} = -\frac{\partial}{\partial r}\frac{\mu_0}{4\pi}\frac{m_1 z}{\sqrt{r^2+z^2}^3} = \frac{\mu_0}{4\pi}\frac{3m_1 zr}{\sqrt{r^2+z^2}^5}, \tag{11.12a}$$

$$B_z^{far} = -\frac{\partial}{\partial z}\frac{\mu_0}{4\pi}\frac{m_1 z}{\sqrt{r^2+z^2}^3} = +\frac{\mu_0}{4\pi}\frac{m_1(2z^2-r^2)}{\sqrt{r^2+z^2}^5}\ . \tag{11.12b}$$

11.2 External field expansion

To obtain an expansion for the external field we take $r' < r$, but make no assumption about z and z'. Then $r'r < (z'-z)^2 + r^2$ and we write equation (11.3) as

$$\varphi = \frac{\mu_0}{2}\int_{-\infty}^{+\infty} dz' \int_0^{\infty} dr' r' \frac{\partial S'}{\partial z'} \frac{1}{\sqrt{(z'-z)^2+r^2}} \int_0^{2\pi} \frac{d\theta'}{2\pi} \frac{1}{\sqrt{1-\left[\dfrac{2r'r\cos\theta' - r'^2}{(z'-z)^2+r^2}\right]}} \tag{11.13}$$

$$= \frac{\mu_0}{2}\int_{-\infty}^{+\infty} dz' \int_0^{\infty} dr' r' \frac{\partial S'}{\partial z'} \frac{1}{\sqrt{(z'-z)^2+r^2}} \int_0^{2\pi} \frac{d\theta'}{2\pi}\ \cdot$$
$$\left\{1 + \frac{1}{2}[...] + \frac{3}{8}[...]^2 + \frac{5}{16}[...]^3 + \frac{35}{128}[...]^4 + ...\right\}, \tag{11.14}$$

where $[...]$ denotes the bracketed expression in eqn. (11.13). After the integrals over θ' are worked and terms of like order in r' are grouped we have

$$\varphi = \frac{\mu_0}{2}\int_{-\infty}^{+\infty} dz' \int_0^{\infty} dr' r' \frac{\partial S'}{\partial z'} \bullet$$
$$\left\{\frac{1}{\sqrt{(z'-z)^2+r^2}} + r'^2\left[-\frac{1}{2}\frac{1}{\sqrt{...}^3} + \frac{3}{4}\frac{r^2}{\sqrt{...}^5}\right] + r'^4\left[\frac{3}{8}\frac{1}{\sqrt{...}^5} - \frac{15}{8}\frac{r^2}{\sqrt{...}^7} + \frac{105}{64}\frac{r^4}{\sqrt{...}^9}\right] + ...\right\}. \tag{11.15}$$

The radial moments defined in section 2 may now be used:

$$S(z)\overline{r^2}(z) = 2\int dr' r' S(r', z)\ , \tag{11.16a}$$

$$S(z)\overline{r^4}(z) = 4\int dr' r'^3 S(r',z)\ , \tag{11.16b}$$

$$S(z)\overline{r^6}(z) = 6\int dr' r'^5 S(r',z)\ ; \tag{11.16c}$$

$$\varphi = \frac{\mu_0}{2}\int_{-\infty}^{+\infty} dz' \left\{ \left[\frac{\partial}{\partial z'} \frac{S(z')\overline{r^2}(z')}{2} \right] \bullet \frac{1}{\sqrt{(z'-z)^2 + r^2}} + \left[\frac{\partial}{\partial z'} \frac{S(z')\overline{r^4}(z')}{4} \right] \bullet \right.$$
$$\left. \left[-\frac{1}{2}\frac{1}{\sqrt{\ldots}^3} + \frac{3}{4}\frac{r^2}{\sqrt{\ldots}^5} \right] + \left[\frac{\partial}{\partial z'} \frac{S(z')\overline{r^6}(z')}{6} \right] \bullet \left[\frac{3}{8}\frac{1}{\sqrt{\ldots}^5} - \frac{15}{8}\frac{r^2}{\sqrt{\ldots}^7} + \frac{105}{64}\frac{r^4}{\sqrt{\ldots}^9} \right] + \ldots \right\}. \tag{11.17}$$

This series appears to be complicated, but in fact we have again generated Legendre polynomials. Let

$$\cos(\gamma) \equiv \frac{(z'-z)}{\sqrt{(z'-z)^2 + r^2}}\ . \tag{11.18}$$

Then eqn. (11.17) may be written

$$\varphi = \frac{\mu_0}{2}\int_{-\infty}^{+\infty} dz' \left\{ \frac{P_0(\cos\gamma)}{\sqrt{(z'-z)^2 + r^2}} \left[\frac{\partial}{\partial z'} \frac{S(z')\overline{r^2(z')}}{2} \right] \right.$$
$$\left. - \frac{1}{2}\frac{P_2(\cos\gamma)}{\sqrt{\ldots}^3} \left[\frac{\partial}{\partial z'} \frac{S(z')\overline{r^4(z')}}{4} \right] + \frac{3}{8}\frac{P_4(\cos\gamma)}{\sqrt{\ldots}^5} \left[\frac{\partial}{\partial z'} \frac{S(z')\overline{r^6(z')}}{6} \right] + \ldots \right\}\ . \tag{11.19}$$

We treat the semi-infinite distribution

$$S(r,z) = S(r)H(-z), \tag{11.20}$$

with $S(r=0) \equiv S$ and $|\vec{r}| \equiv \sqrt{r^2 + z^2}$; from eqn. (11.17):

$$\varphi = \frac{-\mu_0 S}{2}\left\{ \frac{\overline{r^2}}{2}\frac{1}{|\vec{r}|} + \frac{\overline{r^4}}{4}\left[\frac{-1}{2|\vec{r}|^3} + \frac{3r^2}{4|\vec{r}|^5} \right] + \frac{\overline{r^6}}{6}\left[\frac{3}{8|\vec{r}|^5} - \frac{15r^2}{8|\vec{r}|^7} + \frac{105r^4}{64|\vec{r}|^9} \right] + \ldots \right\}. \tag{11.21}$$

These are monopole, quadrupole, octopole, etc. terms. For a thin annular layer at radius R,

$$\overline{r^2} = R^2,\ \ \overline{r^4} = R^4,\ \ \overline{r^6} = R^6,\ldots\ . \tag{11.22}$$

For a uniform thick layer ($R_1 \le r \le R_2$),

$$\overline{r^2} = \frac{R_2^3 - R_1^3}{3(R_2 - R_1)},\ \ \overline{r^4} = \frac{R_2^5 - R_1^5}{5(R_2 - R_1)},\ \ \overline{r^6} = \frac{R_2^7 - R_1^7}{7(R_2 - R_1)},\ldots\ . \tag{11.23}$$

The leading (monopole) term of eqn. (11.21) gives

$$\vec{B}^{ex} = \vec{\nabla}\varphi \approx \frac{\mu_0 S \overline{r^2}}{4}\frac{\vec{r}}{\left|\vec{r}\right|^3} = (\text{direct}\quad \text{flux})\cdot\frac{\vec{r}}{4\pi\left|\vec{r}\right|^3}\ , \tag{11.24}$$

as expected.

12. Field in the Wire Layer

We now have several ways to calculate the field within the wire layer. Near the layer ends an accurate calculation requires the general formalism of section 6 or the thick layer solution (equation (9.3)), plus the contribution from nearby magnets. Away from the wire ends the external field expansion of section 11 plus the direct field $\mu_0 S(r,z)\hat{e}_z$ is applicable.

The peak field in the wire layer is of great interest since it limits the averaged critical current density (sections 2 and 20). Usually this peak field occurs at the inner edge of the wire layer at the middle of a magnet. The logarithmic singularity of B_r at the ends of a thin layer is not representative of realistic cases. The peak field can be accurately estimated using the first two terms of the near-axis expansion if the magnet is not too short $(R/\ell \le .5)$:

$$B_z \approx B_0(z) - B_0''(z)\frac{r^2}{4}\ , \tag{12.1a}$$

$$B_r \approx -B_0'(z)\frac{r}{2} + B_0'''(z)\frac{r^3}{16}\ . \tag{12.1b}$$

We use the thick layer formula for a single magnet, eqn. (9.5), to obtain B_0 and B_0'' at the magnet center (z=0), and by symmetry B_r vanishes there. At the inner wire radius R_1 this gives for a magnet of length ℓ:

$$B_{\max} \cong B_0(0) - \frac{B_0''(0)R_1^2}{4} \ = \ \frac{\mu_0 S}{2}\frac{\ell}{R_2 - R_1}\bullet$$

$$\bullet\left\{Log\left[\frac{2R_2/\ell+\sqrt{1+(2R_2/\ell)^2}}{2R_1/\ell+\sqrt{1+(2R_1/\ell)^2}}\right]+\frac{1}{4}\left(\frac{2R_1}{\ell}\right)^2\left[\frac{(2R_2/\ell)^3}{\sqrt{1+(2R_2/\ell)^2}^3}-\frac{(2R_1/\ell)^3}{\sqrt{1+(2R_1/\ell)^2}^3}\right]\right\}. \quad (12.2)$$

This formula may be written in dimensionless form using the definitions

$$\overline{R}=\frac{R_1+R_2}{2},\ \Delta=\frac{R_2-R_1}{\overline{R}},\ \alpha=2\overline{R}/\ell\ ; \quad (12.3)$$

$$B_{\max}^{\text{approx}}\cong(\mu_0 S)\frac{1}{\alpha\Delta}\left\{Log\left[\frac{\alpha\left(1+\frac{\Delta}{2}\right)+\sqrt{1+\alpha^2\left(1+\frac{\Delta}{2}\right)^2}}{\alpha\left(1-\frac{\Delta}{2}\right)+\sqrt{1+\alpha^2\left(1-\frac{\Delta}{2}\right)^2}}\right]\right.$$
$$\left.+\frac{1}{4}\alpha^5\left(1-\frac{\Delta}{2}\right)^2\left[\frac{\left(1+\frac{\Delta}{2}\right)^3}{\sqrt{1+\alpha^2\left(1+\frac{\Delta}{2}\right)^2}^3}-\frac{\left(1-\frac{\Delta}{2}\right)^3}{\sqrt{1+\alpha^2\left(1-\frac{\Delta}{2}\right)^2}^3}\right]\right\}. \quad (12.4)$$

The degree of accuracy of eqn. (12.4) is indicated in the following table, where the ratio $B_{\max}/B_{\max}^{approx}$ is given for several values of Δ and α.

$\Delta\backslash\alpha$	1.0	.5	.25
1	.998320	.999746	.999990
.5	.992932	.998618	.999948
.25	.987348	.997435	.999904
.10	.982344	.996471	.999868
.04	.979903	.996029	.999851

The exact values of $B_{\max}/\mu_0 S$ for several values of α and Δ are computed and tabulated below from

$$B_{\max} = \frac{\mu_0 S}{R_2 - R_1}\int_{R_1}^{R_2} dR \int \frac{d\theta}{2\pi}\left[\frac{R^2 - RR_1\cos(\theta)}{R^2 + R_1^2 - 2RR_1\cos(\theta)}\right]\cdot \cdot \frac{\ell/2}{\sqrt{\ell^2/4 + R^2 + R_1^2 - 2RR_1\cos(\theta)}} \quad . \tag{12.5}$$

$\Delta \backslash \alpha$	1.0	.5	.25
1.0	.742700	.897437	.968828
.5	.776529	.907269	.971029
.25	.798374	.912353	.971858
.10	.812152	.915356	.972267
.04	.817666	.916536	.972412

13. Current to Produce a Given Field

When designing a magnet system one usually asks for the current distribution to produce a desired field. For solenoids it is clear that any on-axis field profile with $B \le 10T$ can be made with scale length variations down to a few centimeters. But for beam transport and focusing this may also require an unacceptable small inner radius for the wire layer. Increasing the wire layer radius increases the scale length of field variations.

In the present calculation we assume the current is concentrated in a thin layer of fixed radius R; $J_\theta = S(z)\delta(r - R)$. For given $B_0(z)$ it is always possible to solve for $S(z)$, but the field at the wire layer may be unacceptably large if the variations of $B_0(z)$ have scale length smaller than R. This problem may be evaded in some applications by using small radius solenoids where the beam radius is small. Recall the thin layer formula for the on-axis field (Section 3),

$$B_0(z) = \frac{\mu_0 R^2}{2}\int_{-\infty}^{+\infty} dz' \frac{S(z')}{\sqrt{(z' - z)^2 + R^2}^3} \quad .$$

(13.1)

Defining the Fourier integral transformations

$$\left[\tilde{B}_0(k), \tilde{S}(k)\right] = \int_{-\infty}^{+\infty} dz e^{-ikz}\left[B_0(z), S(z)\right] ,$$

(13.2)

we get from eqn. (13.1)

$$\tilde{B}_0(k) = \frac{\mu_0 R^2}{2}\int_{-\infty}^{+\infty} dz' S(z') \int_{-\infty}^{+\infty} dz \frac{e^{-ikz}}{\sqrt{(z'-z)^2 + R^2}^3}$$

$$= \frac{\mu_0}{2}\int_{-\infty}^{+\infty} dz' e^{-ikz'} S(z') \int_{-\infty}^{+\infty} dx \frac{e^{-ikRx}}{\sqrt{x^2+1}^3},$$

(13.3)

with $x = (z - z')/R$. Inserting the identity

$$\int_0^{\infty} dx \frac{\cos(kRx)}{\sqrt{x^2+1}^3} = |kR| K_1(|kR|)$$

(13.4)

gives the general relation

$$\tilde{B}_0(k) = \mu_0 \tilde{S}(k) |kR| K_1(|kR|) \ ,$$

(13.5)

where K_1 is the modified Bessel function. Equation (13.5) gives $\tilde{S}$ if $\tilde{B}_0$ is derived from a given field.

For the specific example,

$$B_0(z) = B_{00} e^{-z^2/L^2} \ ,$$

(13.6)

the transform of $B_0(z)$ and inversion for $S(z)$ are

$$\tilde{B}_0(k) = B_{00}\sqrt{\pi} L e^{-k^2 L^2/4} \ ,$$

(13.7)

$$\mu_0 S(z) = \int_{-\infty}^{+\infty} \frac{dk}{2\pi} \ e^{ikz} \mu_0 \tilde{S}(k) = \int_{-\infty}^{+\infty} \frac{dk}{2\pi} \ e^{ikz} \frac{B_{00}\sqrt{\pi} L e^{-k^2 L^2/4}}{(|k|R) K_1(|k|R)} \ .$$

(13.8)

Setting $y = kL$ gives the convenient form for computations:

$$\frac{\mu_0 S(z)}{B_{00}} = \frac{1}{\sqrt{\pi}} \frac{L}{R} \int_0^{\infty} dy \frac{e^{-y^2/4} \cos(y\, z/L)}{y K_1(y\, R/L)} \ .$$

(13.9)

For $R/L \to 0$ and $|z|/L$ not too large, this formula goes over to the expected form (using $xK_1(x) \to 1$),

$$\mu_0 S(z) \to \; B_{00} e^{-z^2/L^2}.$$

(13.10)

However for finite R/L, $\mu_0 S(z)$ exceeds B_{00} at $z = 0$, e.g. by a factor of 2.5 when R/L=1.0. Also, oscillations of $S(z)$ appear; these provide guidance for the layout of wire that can produce a desired on-axis field. The following figures plot $\mu_0 S(z)/B_{00}$ for various values of R, with L = 1.0.

R/L=.01

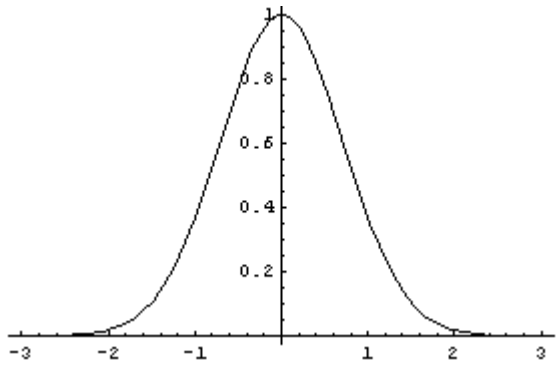

R/L=.5

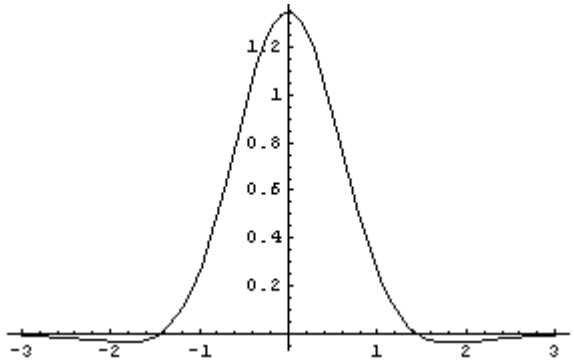

R/L=1

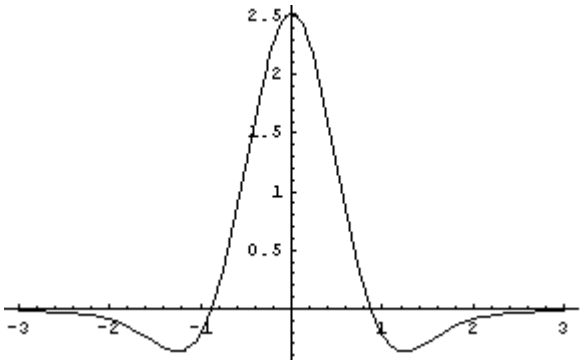

R/L=2

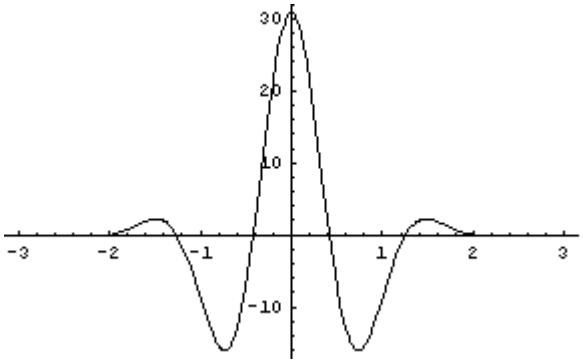

14. <u>Misaligned and Tilted Solenoid</u>

So far we have only treated axisymmetric systems, with field components $B_r(r,z)$ and $B_z(r,z)$. There are always small deviations from this convenient symmetry because of imperfections in design and manufacture, stress, and positioning errors. These imperfections can have a significant effect on a transported ion beam, so it is necessary to specify maximum allowed deviations and make precise field measurements. However, the restricted problem of the effect of positioning errors on the field can be treated analytically as presented below.

The field of a single magnet is considered to be ideal and perfectly characterized in its own coordinate frame. It greatly simplifies the formalism to use Cartesian coordinates. For example if $B_0(z)$ is the known on-axis field in the absence of a positioning error, then

$$B_z^I(x,y,z) = B_0(z) - B_0''(z)\frac{x^2+y^2}{4} + \ldots \ , \tag{14.1a}$$

$$B_x^I(x,y,z) = -\frac{B_0'(z)x}{2} + \frac{B_0'''(z)x(x^2+y^2)}{16} - \ldots \ , \tag{14.1b}$$

$$B_y^I(x,y,z) = -\frac{B_0'(z)y}{2} + \frac{B_0'''(z)y(x^2+y^2)}{16} - \ldots \tag{14.1c}$$

is the magnet's ideal near-axis field.

A misalignment is simply a translation of the magnet center by the vector

$$\vec{T} = \Delta_x \hat{e}_x + \Delta_y \hat{e}_y + \Delta_z \hat{e}_z \quad , \tag{14.2}$$

with displacements Δ_i typically less than $\pm 10^{-3} m$. The misaligned field is obtained from eqn. (14-1) simply by substituting the displacement:

$$\vec{B} = \vec{B}^{\mathrm{I}}(x-\Delta_x, y-\Delta_y, z-\Delta_z) \ . \tag{14.3}$$

A second type of positioning error is a tilt, which holds a magnet's center fixed and orients its axis at an angle α with respect to the system axis, typically with α less than 10^{-3} radians. The tilted magnet axis points in the direction of the unit vector

$$\hat{e} = \sin(\alpha)\cos(\beta)\hat{e}_x + \sin(\alpha)\sin(\beta)\hat{e}_y + \cos(\alpha)\hat{e}_z \ , \tag{14.4}$$

where β is the angle of the projection of $\hat{e}$ in the $x-y$ plane. The two angles (α,β) are the polar coordinates of $\hat{e}$, the usual symbols (θ,φ) having been used for other quantities. A net azimuthal rotation of a magnet around its own axis does not need to be considered since it does not change the field.

The coordinates of a fixed point in the system frame are denoted by (x,y,z) and in the translated and rotated magnet frame by (X,Y,Z). These coordinate sets are related by the inhomogeneous linear transformation

$$\begin{pmatrix} X \\ Y \\ Z \end{pmatrix} = \begin{pmatrix} R_{11}R_{12}R_{13} \\ R_{21}R_{22}R_{23} \\ R_{31}R_{32}R_{33} \end{pmatrix} \begin{pmatrix} x-\Delta_x \\ y-\Delta_y \\ z-\Delta_z \end{pmatrix} , \tag{14.5}$$

where (R_{ij}) is the orthogonal matrix

$$(R_{ij}) = \begin{pmatrix} \cos(\alpha)\cos^2(\beta)+\sin^2(\beta), & (\cos(\alpha)-1)\sin(\beta)\cos(\beta), & -\sin(\alpha)\cos(\beta) \\ (\cos(\alpha)-1)\sin(\beta)\cos(\beta), & \cos(\alpha)\sin^2(\beta)+\cos^2(\beta), & -\sin(\alpha)\sin(\beta) \\ \sin(\alpha)\cos(\beta), & \sin(\alpha)\sin(\beta), & \cos(\alpha) \end{pmatrix} \ . \tag{14.6}$$

Eqn. (14.6) may be derived by multiplying the matrices for successive rotations of the magnet's coordinate frame through angles β, α, and $-\beta$.

The field components of the rotated and translated magnet are then found by applying the transpose of (R_{ij}):

$$B_x(x,y,z) = R_{11}B_x^I(X,Y,Z) + R_{21}B_y^I(X,Y,Z) + R_{31}B_z^I(X,Y,Z)\ , \qquad (14.7a)$$

$$B_y(x,y,z) = R_{12}B_x^I(X,Y,Z) + R_{22}B_y^I(X,Y,Z) + R_{32}B_z^I(X,Y,Z)\ , \qquad (14.7b)$$

$$B_z(x,y,z) = R_{13}B_x^I(X,Y,Z) + R_{23}B_y^I(X,Y,Z) + R_{33}B_z^I(X,Y,Z)\ . \qquad (14.7c)$$

The rotation angles (α,β) are general, but since α is usually very small for tilt errors, the rotation matrix can be well approximated by letting $\cos(\alpha)\to 1$ and $\sin(\alpha)\to\alpha$. Defining the small tilt angles in the x and y directions:

$$\theta_x = \alpha\ \cos(\beta), \qquad \theta_y = \alpha\ \sin(\beta), \qquad (14.8a,b)$$

the approximate matrix is then

$$(R_{ij}) \approx \begin{pmatrix} 1 & 0 & -\theta_x \\ 0 & 1 & -\theta_y \\ \theta_x & \theta_y & 1 \end{pmatrix}\ . \qquad (14.9)$$

This is not quite orthogonal and leads to small violations of $\vec{\nabla}\cdot\vec{B} = 0$. Keeping only terms which are linear in $(\theta_x,\ \theta_y,\ \Delta_x,\ \Delta_y,\ x,\ y)$, we have the approximate near-axis field:

$$B_x \approx -\frac{1}{2}B_0'(z-\Delta_z)\left[(x-\Delta_x) - \theta_x(z-\Delta_z)\right] + \theta_x B_0(z-\Delta_z)\ , \qquad (14.10a)$$

$$B_y \approx -\frac{1}{2}B_0'(z-\Delta_z)\left[(y-\Delta_x) - \theta_y(z-\Delta_z)\right] + \theta_y B_0(z-\Delta_z)\ , \qquad (14.10b)$$

$$B_z \approx B_0(z-\Delta_z)\ . \qquad (14.10c)$$

15. <u>Multiple Channels – Cross Talk</u>

We have treated a system of solenoidal magnets that are centered on a single straight axis, except for misalignments and tilts, which are usually small. More

complicated systems are of interest in which solenoids are positioned along several axes, which may have differing orientations. For example a multiple-beam linac may employ parallel closely-packed solenoid channels, while a system of solenoids designed to bring multiple beams to a single focal spot may have several orientations. In such cases the problem of interference between channels (cross talk) is severe, and it is important to make good estimates of the unwanted field components. This does not mean that any significant cross talk is unacceptable. Generally the effects of unwanted fields can be greatly reduced by a symmetrical layout of channels and the addition of weak bends and quadrupoles around each channel.

We need a simple formula for the residual field of a set of solenoids with arbitrary positions and orientations. This is provided by a generalization of equation (11.21) for the global potential of a semi-infinite current layer:

$$J_\theta(r,z) = J_\theta(r)H(-z), \tag{15.1}$$

$$S = \int_0^\infty dr J_\theta(r), \tag{15.2}$$

$$\varphi \cong -\frac{\mu_0 S}{2}\left\{\frac{\overline{r^2}}{2}\frac{1}{|\vec{r}|} + \frac{\overline{r^4}}{4}\left[\frac{-1}{2|\vec{r}|^3} + \frac{3r^2}{4|\vec{r}\ |^5}\right]\right\}. \tag{15.3}$$

Here we truncated after the lowest moments:

$$S\overline{r^2} = \int_0^\infty dr r^2 J_\theta, \quad S\overline{r^4} = \int_0^\infty dr r^4 J_\theta(r). \tag{15.4}$$

For a thin current layer with radius R, we have $\overline{r^2} = R^2$ and $\overline{r^4} = R^4$. For a thick uniform current layer between R_1 and R_2:

$$\overline{r^2} = \frac{R_2^3 - R_1^3}{3(R_2 - R_1)}, \quad \overline{r^4} = \frac{R_2^5 - R_1^5}{5(R_2 - R_1)}. \tag{15.5a,b}$$

Suppose a solenoid end, denoted by subscript i, is located at $\vec{r}_i$ and has direction $\hat{e}_i$; then its global potential is obtained by substituting into eqn. (15.3) $|\vec{r}| \to |\vec{r} - \vec{r}_i|$ and

$$r^2 = \left|\vec{r}\right|^2 - z^2 = \left|\vec{r}\right|^2 - \left(\vec{r}\cdot\hat{e}_z\right)^2 \rightarrow \left|\vec{r}-\vec{r}_i\right|^2 - \left(\vec{r}\cdot\hat{e}_i - \vec{r}_i\cdot\hat{e}_i\right)^2 \ . \tag{15.6}$$

The quantities $S, \overline{r^2},$ and $\overline{r^4}$ are unchanged; since φ is a scalar quantity we have

$$\varphi_i \cong -\frac{\mu_0 S}{2}\left\{\frac{\overline{r^2}}{2}\frac{1}{\left|\vec{r}-\vec{r}_i\right|} + \frac{\overline{r^4}}{4}\left[\frac{-1}{2\left|\vec{r}-\vec{r}_i\right|^3} + \frac{3}{4}\frac{\left|\vec{r}-\vec{r}_i\right|^2 - \left(\vec{r}\cdot\hat{e}_i - \vec{r}_i\cdot\hat{e}_i\right)^2}{\left|\vec{r}-\vec{r}_i\right|^5}\right]\right\}. \tag{15.7}$$

Each magnet contributes two terms of this type. For example if the downstream end is at $\vec{r}_2$ and the magnet wire layer length is ℓ, then the upstream end is at $\vec{r}_1 = \vec{r}_2 - \ell\hat{e}$. The overall minus sign in eqn. (15.7) is changed to a plus for the upstream magnet end. The total residual field is simply

$$\vec{B}^{residual} = \vec{\nabla}\sum_i \varphi_i \ , \tag{15.8}$$

with applicable values of $\pm S, \vec{r}_i, \overline{r^2},$ and $\overline{r^4}$.

We have included only the two lowest-order terms in the expansion of φ; this should be sufficient for nearly any estimate. In fact the first (monopole) term,

$$\varphi_i \approx -\frac{\mu_0 S_i\left(\overline{r^2}\right)_i}{4\left|\vec{r}-\vec{r}_i\right|} \ , \tag{15.9}$$

should be a good rough guide. The field of the "monopole" term,

$$\vec{B}_i^{residual} = \vec{\nabla}\varphi_i \approx \frac{\mu_0 S_i\left(\overline{r^2}\right)_i\left(\vec{r}-\vec{r}_i\right)}{4\left|\vec{r}-\vec{r}_i\right|^3} \ , \tag{15.10}$$

is just a spherically symmetrical field with the same net flux as the magnet's direct field.

16. Magnetic Materials Basics

There are several reasons for placing highly permeable material around solenoidal wire layers: confining return flux, shaping fields, and reducing stored field energy. It is also possible to make a permanent magnet solenoid. Another application of magnetic materials is in the core of an induction module for acceleration, and also in limiting the high frequency impedance of an acceleration gap. The latter two examples involve time-dependent fields that do not have solenoidal symmetry and are not considered here.

16.1 Ferromagnetism

We are primarily interested in highly-permeable ferromagnetic materials, i.e. those where parallel alignment of atomic magnetic moments produces strong fields in response to weak externally-applied fields. Paramagnetic and diamagnetic materials are not of interest since their induced fields are very small. While the subject of magnetic materials is too vast (and beyond our competence) to even begin a summary here, a few remarks are made for background and clarity. For details see references [16-1, 2, 3].

At temperatures below their Curie points Fe, Co, and Ni display spontaneous magnetization, in which the atomic magnetic moments line up in parallel to minimize the local energy density, i.e. they have the maximum value for projection in a particular direction. These atomic moments are smaller by a factor of several in the ferromagnetic material than in the isolated atoms. A typical magnetic domain, in which the moments are all essentially parallel, is only microns in diameter, and a bulk material sample is usually made up of many small crystals, each containing many such domains. A macroscopic sample's total energy also includes contributions from small-scale fields around the domains as well as magnetostriction and domain wall structure. The small domain size and random orientation minimizes the total energy in the absence of an applied field. These features can be viewed as the result of a competition between atomic and macroscopic (but small scale) forces. However, the domains resist reorientation, so even a very soft (easily magnetized) material can be in a persistent magnetized state of non-minimum energy in the absence of any external excitation. The three room-temperature ferromagnetic elements are often alloyed with each other and/or other elements such as Cr, Si, Al, Mn, Cu, etc. to produce desired characteristics while retaining ferromagnetic features. A small amount of carbon is usually also present in iron as a separate phase mixed with the magnetic crystals.

Below 912^{o} C the stable phase of pure iron is a body-centered-cubic crystal with Curie point 770^{o} C. The magnetic domains are usually aligned in the directions of the three cubic axes (say $\hat{e}_x,\ \hat{e}_y,\ \hat{e}_z$) This material is often referred to as "ferrite" – not to be confused with the ferrimagnetic iron oxide ceramics of the same name, which are used in rapidly-pulsed transformer cores. Nearly pure iron with about .1% carbon (low carbon steel) has the combined properties of high permeability and high saturation field desired for application with high field solenoids. An example is 1010 steel (.08-.13% C, .3-.6% M_n), which is adopted for the linac module design presented in section 20.

When an externally-generated field is applied to a permeable material the domains tend to line up with it, again minimizing energy density. At low-to-moderate fields this happens by domain wall movement of favorably oriented domains at the expense of unfavorably oriented neighbors. For high external fields domains rotate into alignment. The process of domain growth by wall movement is resisted by internal fiction and occurs in tiny jumps with dissipation of energy as heat. For an excellent qualitative discussion of this process see reference [16-3]. Permanent magnets are manufactured with added elements that lock in an induced field along a preferred crystal axis (the easy axis) as they cool from a melt; examples are $SmCo_5$, Sm_2Co_{17}, and NdBFe. Amorphous ferromagnetic alloys such as metglas are produced as uncrystalized tape by very rapid cooling of a melt, and as such they have essentially zero anisotropy energy. Although expensive, the insulated tape has ideal characteristics for transformers and pulsed cores.

16.2 Magnetization formalism

If in a macroscopic region of a material the mean (vector) magnetic dipole moment per atom is $\vec{m}(\vec{r})$, and $n(\vec{r})$ is the atomic number density, then

$$\vec{M}(\vec{r}) = n(\vec{r})\ \ \vec{m}(\vec{r}) \tag{16.1}$$

is called the magnetization density. For a highly permeable material this is an average over many domains. We expect $|\vec{m}|$ to be less than the maximum average projected moment, which is on the order of a Bohr magneton (Fe: $2.218\, m_B$, Co: $1.714\, m_B$, Ni: $.604\, m_B$), but this limit is approached at high applied fields. It was mentioned in section (2) that for solenoidal symmetry $\vec{M}$ has the form

$$\vec{M} = M_r(r,z)\hat{e}_z + M_z(r,z)\hat{e}_z\ , \tag{16.2}$$

and that it provides a current density

$$\vec{J}^{mag} = \vec{\nabla} x \vec{M} = \hat{e}_\theta\left(\frac{\partial M_r}{\partial z} - \frac{\partial M_z}{\partial r}\right). \tag{16.3}$$

The derivation of this relation is presented in many E&M textbooks and is not repeated here. However, its plausibility is made clear by considering a cylinder of length ℓ and radius $R << \ell$, with uniform magnetization density $M\hat{e}_z$. Then eqn. (16.3) gives

$$J_\theta^{mag} = M\ \ \delta(r - R), \tag{16.4a}$$

and the total circulating current is

$$I^{mag} = \ell M \ . \tag{16.4b}$$

We verify that this gives the correct net magnetic moment:

$$\text{moment = area x current = } \left(\pi R^2\right)\left(\ell M\right) = \text{volume x} \begin{pmatrix}\text{magnetization}\\ \text{density}\end{pmatrix} = \sum_{atoms} m_z \ . \tag{16.4c}$$

Eqn. (2.1a) is now generalized to

$$\vec{\nabla} x \vec{B} = \mu_0 (\vec{J} + \vec{J}^{mag}) = \mu_0 (\vec{J} + \vec{\nabla} x \vec{M}) \ , \tag{16.5}$$

where $\vec{J}$ denotes the contribution from wire. It is convenient and conventional to define a new field:

$$\vec{H} \equiv \frac{\vec{B}}{\mu_0} - \vec{M} \ , \tag{16.6}$$

so we write eqn. (16.5) as

$$\vec{\nabla} x \vec{H} = \vec{J} \ . \tag{16.7}$$

Eqn. (2.1b), $\vec{\nabla} \cdot \vec{B} = 0$, is still true, so from eqn. (16.6) we have

$$\vec{\nabla} \cdot \vec{H} = -\vec{\nabla} \cdot \vec{M} \ . \tag{16.8}$$

Therefore $\vec{H}$ may be regarded as being generated by the combination of wire current density $\vec{J}$ and the scalar quantity $-\vec{\nabla} \cdot \vec{M}$ (sometimes called the magnetic pole density). Applying a theorem of vector calculus [16-4], $\vec{H}$ may be derived from its curl and divergence according to

$$\vec{H} = \vec{\nabla} x \int \frac{d^3 r'}{4\pi} \frac{\vec{J'}}{\left|\vec{r'} - \vec{r}\right|} + \vec{\nabla} \int \frac{d^3 r'}{4\pi} \frac{\vec{\nabla'} \cdot \vec{M'}}{\left|\vec{r'} - \vec{r}\right|} , \tag{16.9}$$

assuming the sources vanish at large $\left|\vec{r}\right|$. It is useful to think of $\vec{H}$ as the part of $\vec{B}$ that is produced by distributed sources $\vec{J}$ and $\vec{\nabla} \cdot \vec{M}$, while $\vec{M}$ is the local contribution to $\vec{B}$.

We have followed SI convention in defining $\vec{H}$, so in vacuum it differs from $\vec{B}$ by the factor μ_0^{-1}. Unfortunately this causes $\vec{B}$ and $\vec{H}$ to have different units; these are

Tesla or Webers/m^2 for $\vec{B}$ and Ampere/m for $\vec{H}$ and $\vec{M}$. If $|\vec{B}|$ is 1.0T in vacuum then $|\vec{H}|$ is 795775 Ampere/m. Sometimes $\vec{H}$ is defined as $\vec{H} = \vec{B} - \mu_0 \vec{M}$ instead of eqn. (16.6) to avoid this inconvenience. If Gaussian units are used then the factor μ_0 in eqn. (16.6) is dropped and $\vec{B}$, $\vec{H}$, and $\vec{M}$ all have units of gauss (1.0 gauss = 10^{-4}T), but for $\vec{H}$ this unit is called the oersted. Also, for Gaussian units factors of 4π and c appear as follows:

$$\vec{J}^{mag} = c\vec{\nabla} x \vec{M}, \quad \vec{H} = \vec{B} - 4\pi\vec{M},$$
$$\vec{\nabla} x \vec{H} = \frac{4\pi}{c}\vec{J}, \quad \vec{\nabla}\cdot\vec{H} = -4\pi\vec{\nabla}\cdot\vec{M}.$$

There is considerable variety in the names given for $\vec{B}$ and $\vec{H}$, although they tend to reflect their respective properties or uses. Some of these names are

$\vec{B}$: magnetic field, magnetic induction, magnetic flux density.

$\vec{H}$: magnetic field, magnetic intensity, magnetization field.

16.3 B-H relations and jump conditions

So far we have not related $\vec{H}$ to $\vec{B}$ except by its definition, eqn. (16.6). In fact for a permeable ferromagnetic material there is no completely fixed relation except

$$\left|\vec{B}/\mu_0 - \vec{H}\right| = \left|\vec{M}\right| < M_0 \ , \tag{16.10}$$

with M_0 the magnetization density within a single domain. For example, pure iron (natural isotopic mix) at 0 Kelvin has

$$\rho = 7.87x10^3\, kg/m^3, \text{ atomic mass } = 9.273x10^{-26} kg, \quad m/m_B = 2.218.$$

Inserting the natural constants

$$m_B = 9.274x10^{-24}\, Am^2, \quad \mu_0 = 4\pi x10^{-7} T - m/A,$$

We get

$$M_0 = \frac{\rho}{\text{mass}}\frac{m}{m_B} m_B = 1.746x10^6 \frac{A}{m}, \qquad \mu_0 M_0 = 2.194T.$$

Unalloyed iron with very small amounts of carbon can approach this level of magnetization. An alloy of iron and cobalt (70% Fe, 30% Co) can increase M_0 by 10%.

The value of $\vec{M}$ in a macroscopic sample actually depends on its history of exposure to externally generated fields as well as the instantaneous value of $\vec{H}$. By contrast a linear relation characterizes good permanent magnet blocks:

$$\vec{B} = \hat{e}_{II}\left(B^{rem} + \mu_0 \mu_{II}^r H_{II}\right) + \hat{e}_{\perp}\mu_0 \mu_{\perp}^r H_{\perp}, \tag{16.11}$$

where $_{II}$ and $\perp$ refer to directions along and normal to the easy axis of magnetization. Here B^{rem}, called the remenant field, is simply the "permanent" value of $\mu_0 M$ in a long sample, and the relative permeabilities μ_{II}^r and $\mu_{\perp}^r$ are constants out to large values of H and typically exceed unity by less than 10%. For very large reverse $\mu_0 H$ (depending on material but ideally of order B^{rem} or greater) a block's properties become nonlinear and change irreversibly.

It is apparent that the commonly-assumed linear, isotropic relation

$$\vec{B} = \mu \vec{H} \tag{16.12}$$

is of limited validity except for paramagnetic and diamagnetic substances at low fields. Nevertheless its use is sometimes a justifiable approximation. For example cast iron excited from an initial state of no remanant field exhibits such a linear relationship out to $\left|\vec{B}\right| \approx .3T$, with $\mu \approx 400\mu_0$. Some types of steel have μ greater than $10^4 \mu_0$. Confusing the issue, eqn. (16.12) is often regarded as a definition of μ for whatever $\vec{B}$ and $\vec{H}$ are present, as long as they are parallel. If we assume the validity of eqn. (16.12) then the following definitions are made:

$$K^m \equiv \mu^r \equiv \mu / \mu_0 \tag{16.13}$$

is the relative permeability, and

$$\chi^m = K^m - 1 \tag{16.14}$$

is the magnetic susceptibility. From the definition of $\vec{H}$ we then have

$$\vec{M} = \frac{\vec{B}}{\mu_0} - \vec{H} = K^m \vec{H} - \vec{H} = \chi^m \vec{H}. \tag{16.15}$$

An improvement on (16.12), used in some computations, is

$$\vec{B} = \vec{B}_0 + \mu\left(\vec{H} - \vec{H}_0\right), \tag{16.16}$$

where $\vec{B}_0$ and $\vec{H}_0$ are some particular values and μ is a local coefficient.

For many computations it is simply assumed that $\mu/\mu_0 \to \infty$, i.e. $\vec{H}$ vanishes in the highly permeable material. However, to compute $\vec{B}$ inside the material requires specification of details about the permeability, even though it approaches infinity – see section (18).

If $\vec{B}$ and $\vec{H}$ are to be determined by solution of the coupled underlying differential equations, then jump conditions at vacuum-material interfaces are required. From eqns. (16.7) and (2.1b) these are

$$H_t \text{ is continuous,} \tag{16.17a}$$

$$B_n \text{ is continuous,} \tag{16.17b}$$

where t and n refer to components tangential and normal to the interface.

These jump conditions suggest the utility of a highly permeable material for flux control or field shaping. Since $\mu_0\vec{H}$ can essentially vanish in the material, its tangential component on the vacuum side of the boundary also vanishes, as does the vacuum tangential component of $\vec{B}$. But the vacuum field can be derived from a scalar potential, $\vec{B} = \mu_0\vec{\nabla}\phi$, which is single valued around the material if no wire is enclosed. Therefore ϕ is constant on the material surface. By analogy with electrostatics, the material acts like a conducting surface, and strong normal fields may be localized to particular locations where the surface is strongly curved. Roughly speaking the field is channeled in and out of the material where desired, and routed away from locations (such as an induction core) where it could cause a problem. It is also apparent that stored energy might be reduced in this way since energy density in the material is roughly $BH/2 \approx 0$, although the concentration of flux in particular locations outside the material tends to increase stored energy density. The design of the poles and yoke of a cyclotron is an application of these ideas.

Field calculations for highly permeable materials are complicated by both non-linearity of $B-H$ curves and the phenomenon of hysteresis. The latter is closely related to internal dissipation of energy during excitation and de-excitation. Following the textbooks, we imagine that in a macroscopic region of material $\vec{B}$ and $\vec{H}$ are parallel (more about this assumption below) and H is increasing or decreasing slowly with time. Depending on the sign of dH/dt two different curves are generated. If H is cyclical, a closed loop in the $B-H$ plane is produced. If sufficiently large values of H are in the cycle, so that the material is pushed well into saturation, then a maximal hysteresis loop is generated, and all other loops lie somewhere inside of it. The maximal hysteresis loop is the boundary of accessible points in the $B-H$ plane under the assumptions of parallelism and slow variation. This is considerably more restrictive than the condition

(16.10). The intercepts of the maximal hysteresis curve with the B and H axes are called respectively the remanence $(\pm B_r)$ and coercive force $(\pm H_c)$. Some loops have zero bias current, i.e. no mean H, and form a nested set around the origin $(B = H = 0)$. Other (biased) loops are offset from the origin and may or may not encircle it. In this picture we assume that the magnet is excited slowly enough that eddy currents are not appreciable and that magnetic domains have time to adjust their walls or orientations. All closed loops must cycle in a counter-clockwise direction to avoid a violation of the second law of thermodynamics. To see this, note that the differential work done by an external circuit is HdB per unit volume. A clockwise loop would extract energy into the circuit and cool the material (eliminating any need for controlled fusion). Through every point (B, H) interior to the maximal loop we may draw a pair of paths, which are followed depending on whether H is increasing or decreasing. A grid of crossing paths covers the accessible $B - H$ space, and any point may be reached by traversing several paths in their allowed directions. Complete demagnetization can be done by cycling H with gradually decreasing amplitude.

16.4 Magnetization curve

Since ferromagnetic materials have a nonlinear magnetization response when driven over a large range, a generalization of eqn. (16.12) is required for computations. Usually it is assumed that a material is excited from an initially unmagnetized state and that H only increases in this process, so there is no ambiguity from hysteresis. Then B follows a known "magnetization curve", i.e. $B = F(H)$ - see the accompanying figure for examples (from Chao and Tigner, Handbook of Accelerator Physics and Engineering, World Scientific, 1999.) Computations may be made by setting

$$\vec{B} = \vec{H} F\left(\vec{r}, \left|\vec{H}\right|\right) \Big/ \left|\vec{H}\right| , \tag{16.18}$$

which assumes $\vec{B}$ and $\vec{H}$ remain parallel everywhere. This assumption works if the response is linear, i.e. $F = \mu(\vec{r})H$. To demonstrate this we write eqn. (16.9) in the form

$$H_i = H_i^J + \int \frac{d^3 r'}{4\pi} M'_j \frac{\partial^2}{\partial x_i \partial x_j} \frac{1}{\left|\vec{r'} - \vec{r}\right|} , \tag{16.19}$$

with subscripts (i, j) denoting Cartesian components with a sum over j, and $\vec{H}^J$ is the part of $\vec{H}$ produced by currents in wire. For the linear isotropic response we have

$$\vec{M}(\vec{r'}) = \chi^m(\vec{r'})\vec{H}(\vec{r'}) , \tag{16.20}$$

with $\chi^m = \mu/\mu_o - 1$, and eqn. (16.19) can be reduced to a set of coupled linear equations by dividing the entire space into small volumes (finite element method). $\vec{H}$ is then

obtained from $\vec{H}^J$ by a single matrix inversion, and the assumption of parallelism has lead to a unique solution. For a non-linear magnetization curve, we can use

$$\vec{M} = \frac{\vec{B}}{\mu_0} - \vec{H} = \left(\frac{F\left(\vec{r}, \left|\vec{H}\right|\right)}{\mu_0 \left|\vec{H}\right|} - 1 \right) \vec{H}, \tag{16.21}$$

and it is necessary to iterate to solve eqn. (16.19). Unfortunately it is not clear that this procedure leads to the physically correct solution, although this is generally assumed. Consider a system that is excited from the un-magnetized state by slowly increasing the wire current. If the material response is linear then $\vec{B}$ and $\vec{H}$ simply scale up proportional to current without changing direction. But the situation is changed when the material saturates and $\vec{B} \to \mu_0 \vec{H}$; fields then approximate a vacuum pattern determined from the wire current alone, and in general they have a different direction than when the permeable material is effective. During the current increase $\vec{B}$ and $\vec{H}$ have changed direction; but this is different from the simple experimental conditions in which magnetization curves are determined. It is conceivable that during a gradually changing direction of $\vec{H}$, that $\vec{M}$ (and therefore $\vec{B}$) stays parallel, but this is an additional material property to be determined by experiment.

A mathematical model of hysteresis has been described in an interesting series of reports - see [16-5]. Recall that every $B-H$ point inside the limiting cycle is crossed by two curves with slopes dB/dH depending on whether H is increasing or decreasing. These slopes are found to be well approximated by the assumed formula

$$\frac{dB}{dH} = \pm\alpha\left[f(H) - B \right] + g(H) , \tag{16.22}$$

where α is a constant and (f, g) are material-dependent functions with examples given in the cited report. The choice $\pm \to +$ or - depends respectively on H increasing or decreasing. A generalization that includes isotropic permanent magnets is written

$$\frac{dH}{dB} = \pm\alpha\left[\tilde{f}(B) - H \right] + \tilde{g}(B). \tag{16.23}$$

The function $\tilde{g}$ can be modified to include dependence on the rate of magnetization (dB/dt). If α, f and g are known, then the magnetization curve $F(H)$ can be found in numerical form by integrating eqn. (16.22) from the origin $(B = H = 0)$ with increasing H:

$$\frac{dB}{dH} + \alpha B = \alpha f(H) + g(H) , \tag{16.24}$$

$$F(H) = B = \int_0^H dH' \left[\alpha f(H') + g(H') \right] e^{\alpha(H'-H)} \ . \tag{16.25}$$

16.5 Permanent magnet solenoid

Finally we consider the simple permanent magnet solenoid consisting of an annulus of constant magnetization $M\hat{e}_z$ between radii R_1 and R_2 and with length ℓ, centered at $z = 0$. The magnetization currents are simply a pair of thin layers:

$$J_\theta^{\text{mag}} = -\frac{\partial M_z}{\partial r} = M\left[\delta(r - R_2) - \delta(r - R_1) \right] . \tag{16.26}$$

Applying the thin layer result, eqn. (4.5), we have the on-axis field

$$B_0(z) = \frac{\mu_0 M}{2} \left[\begin{array}{c} \dfrac{(z + \ell/2)}{\sqrt{(z + \ell/2)^2 + R_2^2}} - \dfrac{(z - \ell/2)}{\sqrt{(z - \ell/2)^2 + R_2^2}} \\ - \dfrac{(z + \ell/2)}{\sqrt{(z + \ell/2)^2 + R_1^2}} + \dfrac{(z - \ell/2)}{\sqrt{(z - \ell/2)^2 + R_1^2}} \end{array} \right] . \tag{16.27}$$

This function is plotted below for $(\mu_0 M = 1.0\text{T},\ \ R_2 = .5\text{m},\ \ R_1 = .25\text{m},\ \ \ell = 1.0\text{m})$. Note that B_0 is negative in the solenoid bore and positive outside, and its maximum absolute value is only $.19\mu_0 M$. When such a solenoid is used as a particle beam lens, its focal strength is proportional to the integral of B_0^2, so it is not a very effective use of material, although such lenses have been used to confine electron beams in Klystrons. It can be easily verified that

$$\int_{-\infty}^{+\infty} dz B_0(z) = 0 . \tag{16.28}$$

In fact this relation is true for any solenoid made only of magnetic materials since $\vec{\nabla} x \vec{H} = \vec{J}$ requires that the line integral of $\vec{H}$ around any closed loop must equal the enclosed wire current:

$$\oint d\vec{r} \cdot \vec{H} = I = 0 \ . \tag{16.29}$$

In the present case we may take the integration loop along the entire axis and return at large radius, where there is a vanishing contribution.

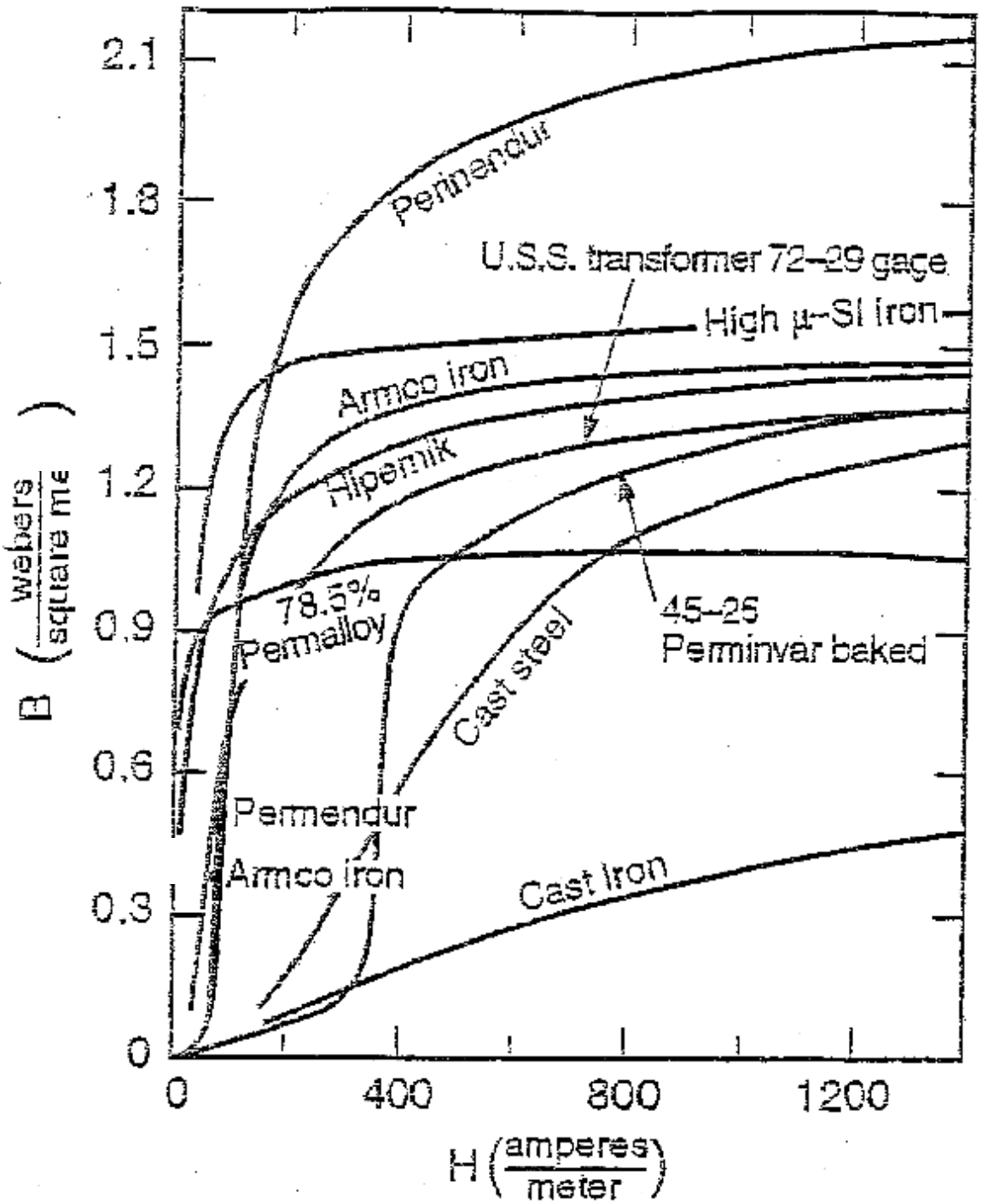
2.1
1.8
1.5
1.2
0.9
0.6
0.3
0
B (webers / square me
0
400
800
1200
H (amperes / meter)
Permendur
U.S.S. transformer 72–29 gage
High μ–Si iron
Armco iron
Hipernik
78.5% Permalloy
45–25 Perminvar baked
Cast steel
Permendur
Armco iron
Cast iron

```
mu0M = 1.0;
R2 = .5;
R1 = .25;
l = 1.0;

B0[z_] = mu0M/
      2*((z + l/2)/((z + l/2)^2 + R2^2)^.5 - (z -
            l/2)/((z - l/2)^2 + R2^2)^.5 - (z +
            l/2)/((z + l/2)^2 + R1^2)^.5 + (z -
            l/2)/((z - l/2)^2 + R1^2)^.5);

Plot[B0[z], {z, -2, 2}];
```

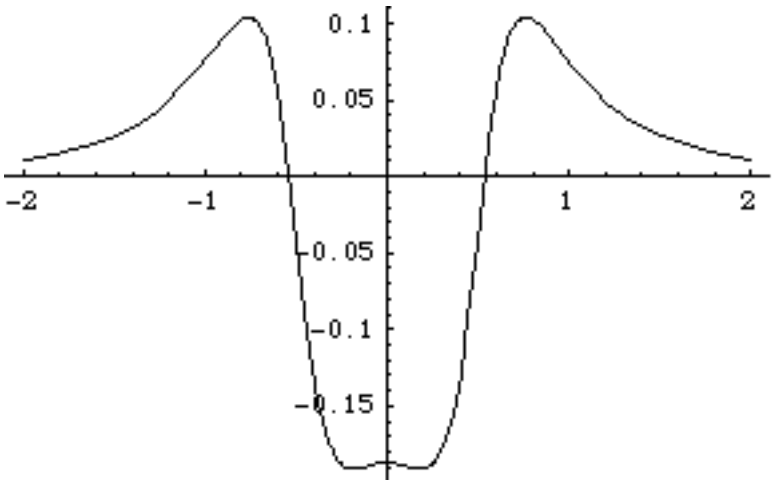

References

16-1 Bozorth, R.M., Ferromagnetism, IEEE Press, 1993.

16-2 Kittel, C., Introduction to Solid State Physics, 7th ed., ch. 15, John Wiley & Sons, 1996.

16-3 Feynman, R., Leighton, R., and Sands, M., The Feynman Lectures on Physics, Vol II, ch 37, Addison – Wesley, 1964.

16-4 Panofsky, W., and Phillips, M., Classical Electricity and Magnetism, 2nd ed., pp 2-5, Addison – Wesley, 1962.

16-5 Hodgdon, M., Applications of a Theory of Ferromagnetic Hysteresis, IEEE Transactions on Magnetics, Vol. 24, No 1, January 1988. 218-221.

17. Wire Layer Embedded in a Highly Permeable Yoke

A simple geometry that displays flux confinement is a wire layer (of any shape) that has net azimuthal current I and is embedded in a long permeable annulus with $\mu = \infty$. The inner radius of the annulus/yoke is at $r = b$, which is also the magnet's bore radius, and a narrow slot connects the wire layer to the bore at $z = 0$ (see figure).

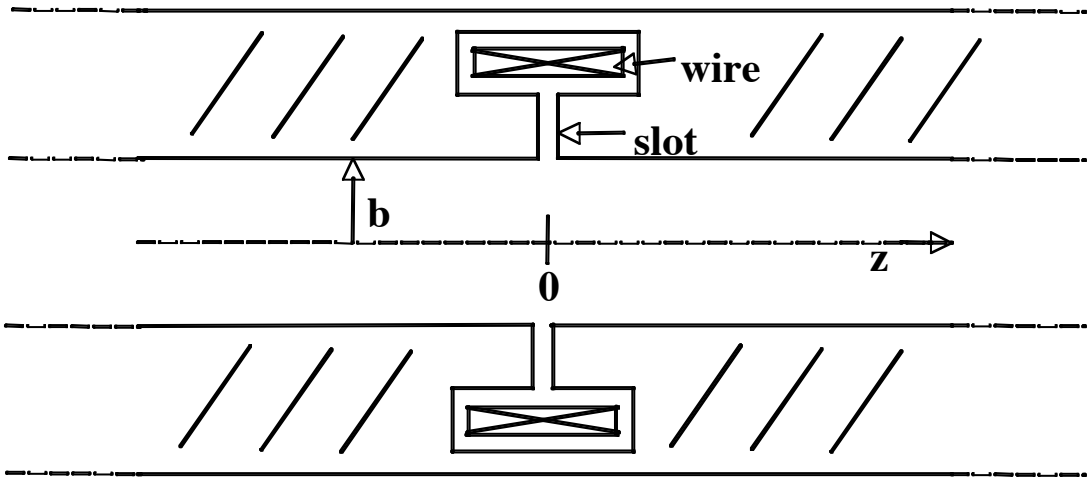

Inside the bore, where

$$\vec{H} = \frac{\vec{B}}{\mu_0} = \overrightarrow{\nabla\phi}, \qquad (17.1a,b)$$

we have

$$\nabla^2\phi = 0, \qquad \nabla^2 B_z = 0\ . \qquad (17.2a,b)$$

Along the inner surface of the annulus ϕ is constant and B_z vanishes, except at $z = 0$, where ϕ jumps and B_z is infinite:

$$\phi(b,z) = \begin{cases} -I/2 & z < 0 \\ +I/2 & z > 0, \end{cases} \qquad (17.3)$$

$$B_z(b,z) = \mu_0 I \delta(z)\ . \qquad (17.4)$$

Here the annulus is assumed to extend to $z = \pm\infty$ for computations.

To solve for B_z in the magnet bore we apply a Fourier integral transform to eqn. (17.2 b):

$$\tilde{B}_z(r,k) = \int_{-\infty}^{+\infty} dz \;\; e^{-ikz} B_z(r,z) \;, \tag{17.5}$$

$$\frac{1}{r}\frac{\partial}{\partial r} r \frac{\partial \tilde{B}_z}{\partial r} - k^2 \tilde{B}_z = 0 \;. \tag{17.6}$$

Equation (17.6) is satisfied by

$$\tilde{B}_z = f(k) I_0(|k|r) \;, \tag{17.7}$$

where I_0 is the modified Bessel function and $f(k)$ is to be determined from the boundry condition (17.4). Since we may write the delta function as

$$\delta(z) = \int_{-\infty}^{+\infty} dk \frac{e^{ikz}}{2\pi} \;, \tag{17.8}$$

we have immediately from equations (17.4) and (17.7)

$$B_z = \int_{-\infty}^{+\infty} dk \frac{e^{ikz}}{2\pi} \tilde{B}_z = \mu_0 I \int_{-\infty}^{+\infty} dk \frac{e^{ikz}}{2\pi} \frac{I_0(|k|r)}{I_0(|k|b)} \;. \tag{17.9}$$

A convenient form for computations, that displays scaling with r/b and z/b is

$$B_z = \frac{\mu_0 I}{\pi b} \int_0^{\infty} dy \frac{\cos(y\, z/b) I_0(yr/b)}{I_0(y)} \;, \tag{17.10}$$

where $y \equiv kb$. The radial field is obtained from eqn. (17.9) by integrating $\vec{\nabla} \cdot \vec{B} = 0$:

$$B_r = -\mu_0 I \int_{-\infty}^{+\infty} dk \frac{k}{|k|} i \frac{e^{ikz}}{2\pi} \frac{I_1(|k|r)}{I_0(|k|b)} \tag{17.11}$$

$$= \frac{\mu_0 I}{\pi b} \int_0^{\infty} dy \;\; \sin(yz/b) \frac{I_1(yr/b)}{I_0(y)} \;. \tag{17.12}$$

The bore field is displayed for several values of r/b at the end of this section. A strong (exponential) falloff with $|z|/b$ is apparent and contrasts sharply with the $|z|^{-3}$ fall off from a lens without a yoke. This calculation is formally equivalent to that of an electrostatic field in a conducting pipe that is split at $z = 0$ and with a potential difference applied to the two sides.

The potential ϕ can be derived from eqn. (17.9) by integration in z, however at this point it is more instructive to use an expansion in ordinary Bessel functions:

$$\phi = \frac{I}{2} + \sum_{i=1}^{\infty} A_i \;\; J_0\left(x_i \, r/b\right) e^{-x_i z/b} \;, \tag{17.13}$$

valid for $z > 0$. For $z < 0$, ϕ is determined by its antisymmetry:

$$\phi = \left(r, -z\right) = -\phi(r,z) \;, \tag{17.14}$$

so the there is exponential decay in both directions. The χ_i are the zeros of J_0, and the coefficients A_i are determined from the condition

$$0 = \phi(r,0) = \frac{I}{2} + \sum_{i=1}^{\infty} A_i J_0\left(x_i \, r/b\right) \;; \tag{17.15}$$

$$A_i = -\frac{I}{x_i J_1\left(x_i\right)} \;. \tag{17.16}$$

We have for $z > 0$,

$$\phi = \frac{I}{2} - I \sum_{i=1}^{\infty} \;\; \frac{J_0\left(x_i \, r/b\right) e^{-x_i z/b}}{x_i J_1\left(x_i\right)} \;, \tag{17.17}$$

$$B_z = \mu_0 \frac{\partial \phi}{\partial z} = \mu_0 \frac{I}{b} \sum_{i-1}^{\infty} \;\; \frac{J_0\left(x_i \, r/b\right) e^{-x_i z/b}}{J_1\left(x_i\right)} \;. \tag{17.18}$$

The first five values of x_i and $J_1\left(x_i\right)$ are tabulated to aid in computations:

i	x_i	$J_1\left(x_i\right)$
1	2.40482 55577	.51914 74973
2	5.52007 81103	-.34026 48065
3	8.65372 79129	.27145 22999
4	11.79153 44391	-.23245 98314
5	14.93091 77086	.20654 64331

The on-axis field can be calculated from either the Fourier integral or Bessel series, although the latter is poorly convergent for $|z|/b \approx 0$. The leading term of the series is a good approximation for $|z|/b \geq 1$:

$$B_0 \to \frac{\mu_0 I}{b} \frac{e^{-x_1 |z|/b}}{J_1(x_1)} , \tag{17.19}$$

but is large by a factor of 2.9 at $z = 0$. An excellent approximation for all z is

$$B_0 \approx \frac{\mu_0 I}{b} \frac{1}{J_1(x_1)} \frac{1}{\left[2\cosh\left(x_1 |z|/sb\right)\right]^s} \tag{17.20}$$

with $s = 1.538781$. This has maximum relative error of $\pm 2\text{x}10^{-4}$ at $|z|/b = (0, \pm .7b)$.

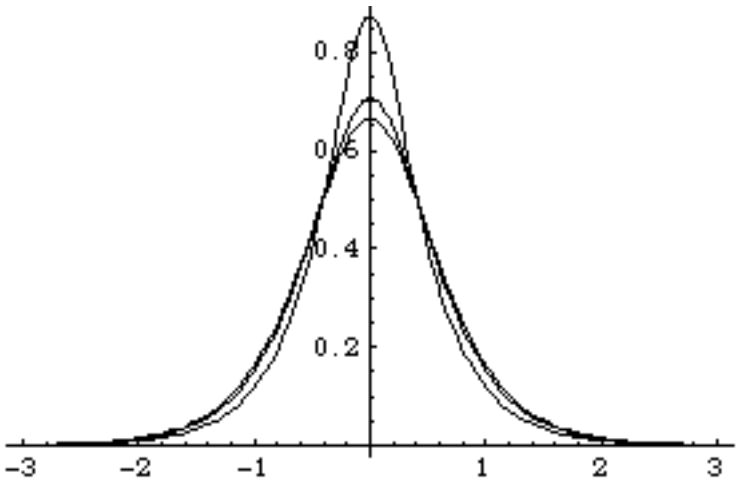

$B_z(r,z)$ for $r = (0,\ b/4, b/2)$. In this case $\mu_0 I = 1.0$ and $b = 1.0$.

18. Periodic Wire Layer with Highly a Permeable Yoke

Return flux can be channeled by a permeable annulus if the field there is kept below saturation $(B_{\text{sat}} \approx 1.0 - 2.0\text{T for iron})$. For a periodic system of solenoids all having the same polarity, the field in the annulus or yoke is roughly

$$B_{\text{yoke}} \approx -\frac{R^2 B_{\text{bore}}\, \ell/P}{R_2^2 - R_1^2} , \tag{18.1}$$

where R is the wire radius, R_1 and R_2 are the yoke radii, ℓ/P is the ratio of wire layer length to period length, and B_{bore} is the peak bore field. The volume of the yoke should be at least $B_{\text{bore}}/B_{\text{sat}}$ times the total volume of magnet bore to prevent stray flux from entering the outside world. In practice there will be gaps in the yoke, so some flux will bulge out anyway.

The field in the presence of a highly permeable yoke can be examined with the simple periodic model:

$$J_\theta = \begin{cases} S\delta(r-R) & -\ell/2 < z < \ell/2, \\ 0 & \ell/2 < |z| < P/2, \end{cases} \tag{18.2}$$

$$\mu = \begin{cases} \infty & R_1 < r < R_2, \\ 0 & \text{other } r, \end{cases} \tag{18.3}$$

with $R < R_1$ and J_θ repeating with period P. The Fourier expansion of the current density is

$$J_\theta = \delta(r-R)\left[\frac{S\ell}{P} + \sum_{n=1}^{\infty}\delta_n \cos(k_n z)\right] \equiv \delta(r-R)S(z)\ , \tag{18.4}$$

with

$$\delta_n = \frac{2S}{\pi n}\sin\left(\frac{\pi n \ell}{P}\right)\ ,\quad k_n = \frac{2\pi n}{P}\ . \tag{18.5a,b}$$

In the yoke $\vec{H} = \vec{B}/\mu \to 0$ by assumption, and since the tangential components of $\vec{H}$ at R_1 and R_2 are continuous, we conclude the $B_z = \mu_0 H_z = 0$ at $r = R_{1-}$ and $r = R_{2+}$. Since $\vec{B}$ must vanish as $r \to \infty$, it must also vanish for all $r > R_2$. For $r < R_1$ we must simply solve

$$\nabla^2 B_z = -\mu_0 \frac{1}{r}\frac{\partial}{\partial r} r J_\theta\ , \tag{18.6}$$

with the boundary condition $B_z(R_{1-}) = 0$.

The value of $\vec{B}$ inside the yoke is indeterminate unless more information is given about the permeability, which must be assumed to be not quite infinite. For example, suppose we have a non-linear magnetization curve

$$\vec{B} = \frac{\vec{H}}{\left|\vec{H}\right|} \mathrm{F}\left(\left|\vec{H}\right|\right) \quad , \tag{18.7a}$$

$$\vec{H} = \frac{\vec{B}}{\left|\vec{B}\right|} \mathrm{F}^{-1}\left(\left|\vec{B}\right|\right) . \tag{18.7b}$$

Then in the yoke we must solve $\vec{\nabla} \cdot \vec{B} = 0$ along with

$$\vec{\nabla} x \left[\frac{\vec{B}}{\left|\vec{B}\right|} \mathrm{F}^{-1}\left(\left|\vec{B}\right|\right) \right] = \vec{\nabla} x \vec{H} = 0 \ . \tag{18.8}$$

The boundary conditions for the yoke interior are that B_r be continuously joined to its vacuum values at R_1 and R_2 and that the net flux of the system vanish. For the simple assumption that μ is very large but constant, the Cartesian components of the yoke field satisfy

$$\nabla^2 \vec{B} = \cancel{\vec{\nabla}\vec{\nabla} \cdot \vec{B}} - \vec{\nabla} x \left(\vec{\nabla} x \vec{B} \right) = -\vec{\nabla} x \left(\vec{\nabla} x \mu \vec{H} \right) = 0 \ . \tag{18.9}$$

Returning to the analytical model and assuming B/H is infinite but constant in the yoke, we have inside all four radial zones

$$\nabla^2 B_z = 0 . \tag{18.10}$$

At zone boundaries $\left(R, R_1, R_2\right)$ both B_r and $\partial B_z / \partial r$ are continuous, while B_z jumps across the wire:

$$B_z\left(R_+, z\right) - B_z\left(R_-, z\right) = -\mu_0 S\left(z\right) \ . \tag{18.11}$$

At the yoke boundaries it is also found that B_z jumps from zero in vacuum to a finite value in the material that is found by solving the model equations. We proceed by solving for the field produced by individual terms of the expansion eqn. (18.4) for J_θ. First, the term $S\ell / P$ produces

$$B_z \to \begin{cases} \dfrac{\mu_0 S\ell}{P} & 0 < r < R, \\ 0 & R < r < R_1, \\ -\dfrac{R^2}{R_2^2 - R_1^2}\dfrac{\mu_0 S\ell}{P} & R_1 < r < R_2, \\ 0 & R_2 < r < \infty. \end{cases} \tag{18.12}$$

This function has net zero flux, vanishes at $r = \infty$, and has no on-axis contribution from the permeable material (as discussed in section (16)). Next consider the field from any periodic term of eqn. (18.4); this has the form

$$S(z) \to \delta_n \cos(k_n z)\,, \tag{18.13a}$$

$$B_z \to \mu_0 f_n(r)\delta_n \cos(k_n z), \tag{18.13b}$$

$$B_r \to \mu_0 g_n(r)\delta_n \sin(k_n z). \tag{18.13c}$$

Inside each zone f_n satisfies

$$\frac{1}{r}\frac{d}{dr} r \frac{df_n}{dr} - k_n{}^2 f_n = 0\,, \tag{18.14}$$

and from $\vec{\nabla} \times \vec{B} = 0$, inside any zone

$$g_n = \frac{1}{k_n}\frac{\partial f_n}{\partial r}. \tag{18.15}$$

Equation (18.14) is a modified Bessel equation, so $f_n(r)$ is a linear combination of $I_0(k_n r)$ and $K_0(k_n r)$ in every zone, and $g_n(r)$ is the combination of $I_1(k_n r)$ and $K_1(k_n r)$ determined from eqn. (18.15). Applying the various boundary and jump conditions and finiteness at $r = 0$ we find, suppressing the subscript (n):

$\underline{0 < r < R}$

$$f(r) = AI_0(kr), \tag{18.16a}$$

$$g(r) = AI_1(kr)\,, \tag{18.16b}$$

$\underline{R < r < R_1}$

$$f(r) = B\left[\frac{I_0(kr)}{I_0(kR_1)} - \frac{K_0(kr)}{K_0(kR_1)}\right], \tag{18.16c}$$

$$g(r) = B\left[\frac{I_1(kr)}{I_0(kR_1)} + \frac{K_1(kr)}{K_0(kR_1)}\right], \tag{18.16d}$$

$\underline{R_1 < r < R_2}$

$$f(r) = C\left[\frac{I_0(kr)}{I_1(kR_2)} + \frac{K_0(kr)}{K_1(kR_2)}\right], \tag{18.16e}$$

$$g(r) = C\left[\frac{I_1(kr)}{I_1(kR_2)} - \frac{K_1(kr)}{K_1(kR_2)}\right], \tag{18.16f}$$

$\underline{R_2 < r < \infty}$

$$f(r) = g(r) = 0, \tag{18.16g}$$

with coefficients

$$A = \frac{kR}{I_0(kR_1)}\left[I_1(kR)K_0(kR_1) + K_1(kR)I_0(kR_1)\right], \tag{18.17a}$$

$$B = kRI_1(kR)K_0(kR_1), \tag{18.17b}$$

$$C = B\frac{RI_1(kR)}{R_1I_0(kR_1)}\left[\frac{I_1(kR_1)}{I_1(kR_2)} - \frac{K_1(kR_1)}{K_1(kR_2)}\right]^{-1}. \tag{18.17c}$$

We have used the Bessel function identity

$$I_1(x)K_0(x) + I_0(x)K_1(x) = \frac{1}{x} \tag{18.18}$$

to simplify these expressions.

Plots. B_z vs z for various r are given below for the case $\left(R = .2,\ R_1 = .6,\ R_2 = .8,\ P = 1.0,\ \ell = .8,\ \mu_0 S\ell/P = 10.0T\right)$. The suppression of the external field in the zone $R < r < R_1$ is evident – compare section (10).

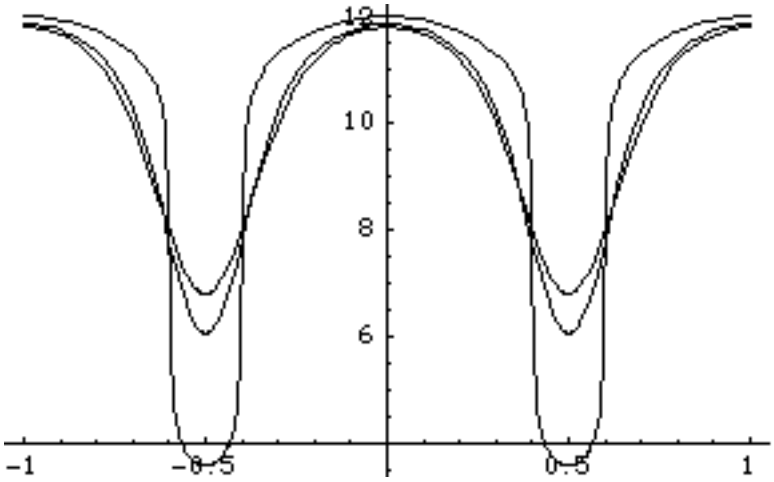

(Bore)

r	$B_z(r,0)$
.000	11.79
.100	11.85
.195	11.99

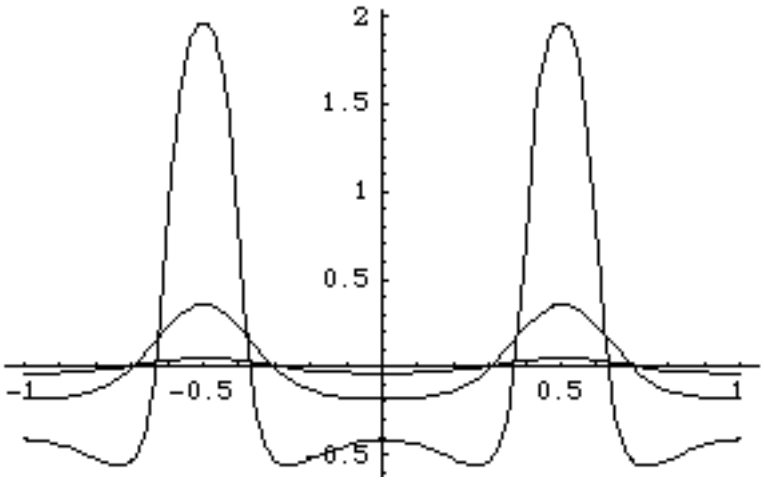

(External)

r	$B_z(r,0)$
.25	-.4135
.40	-.1006
.55	-.0323

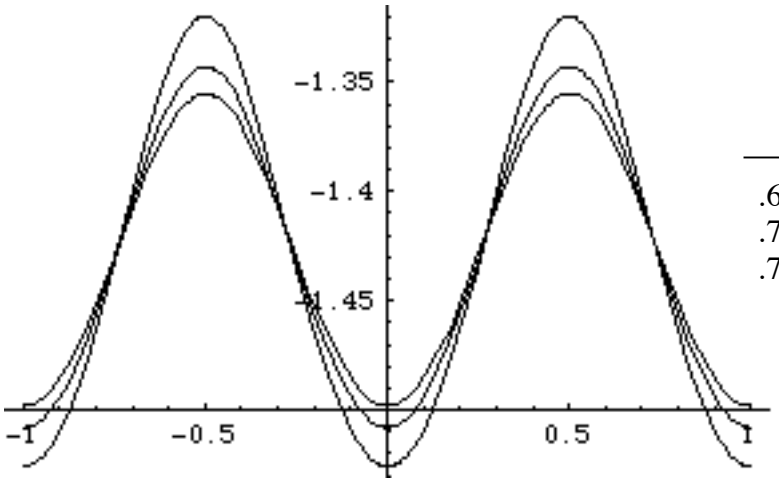

(Yoke)

r	$B_z(r,0)$
.65	-1.526
.70	-1.508
.75	-1.498

.19. Tosca© Model

Many computer programs have been written for the purpose of solving Laplace's or Poisson's equation under given boundary conditions. A number of different numerical solution methods exist for solving a system of partial differential equations; one of the most commonly applied techniques is the finite element discretization method. Finite element analysis (FEA) requires special enhancements, which are described briefly in this chapter, to make it applicable to electromagnetic field calculations.

Computer programs most widely used in the accelerator engineering community are the public domain code POISSON [[i]-7], and the commercial code Tosca© [1-7]. POISSON can simulate only 2d plane or axisymmetric geometries, whereas Tosca© allows calculations in 2D and 3D. Since today's personal computers have become sufficiently powerful, the fidelity of these codes is so superior that often simulations are used to check measurements, and large magnetic devices are designed without the need for building prototypes. For instance, a field accuracy of the order of parts in 10^6 is required for simulating shielded superconducting NMR systems. Another application is to cyclotrons with their stringent field accuracies (parts in 10^5), which can nowadays be entirely designed using Tosca© alone.

FEA codes are especially well suited for modeling magnetic field problems with non-linear materials present, e.g. magnet steel or permanent magnets. Forces on conductors and pole pieces can be easily calculated. In addition, harmonic or transient field problems with eddy currents present can be solved. Eddy current heating as well as magnetic forces can be coupled to thermal and structural FEA simulations for the engineering design.

.19.1 General solution strategy in 3D

In this section the notation for fields differs somewhat from that used in the rest of the report in order to correspond to Tosca© conventions. A detailed description of how to numerically solve Maxwell's equations is beyond the scope of this report. Nevertheless,

since the computation of magnetic fields requires a few special numeric treatments, its peculiarities are briefly mapped out here. We want to discretize Maxwell's equations:

$$\vec{\nabla} x \vec{E} = -\frac{\partial \vec{B}}{\partial t} \quad , \tag{19.1a}$$

$$\vec{\nabla} x \vec{H} = \frac{\partial \vec{D}}{\partial t} + \vec{j} \quad , \tag{19.1b}$$

$$\vec{\nabla} \cdot \vec{D} = \rho \quad , \tag{19.1c}$$

$$\vec{\nabla} \cdot \vec{B} = 0 \quad , \tag{19.1d}$$

with $\vec{D} = \varepsilon \vec{E}$, $\vec{B} = \mu \vec{H}$, and $\vec{j} = \sigma \vec{E}$ (or is specified). In these equations $\vec{E}$ and $\vec{H}$ are the electric and magnetic fields and $\vec{D}$ and $\vec{B}$ are the electric and magnetic flux densities. The current density is denoted by $\vec{j}$, and ρ denotes the charge density. The three material functions ε, μ, and σ (permittivity, permeability, and conductivity) are in general functions of the spatial coordinates and also nonlinear functions of the electromagnetic field strength, e.g. saturation effects in metal. All three material properties may be tensors, as in laminated transformer cores and permanent magnets.

The usual procedure for solving Maxwell's equations is to simplify them as far as

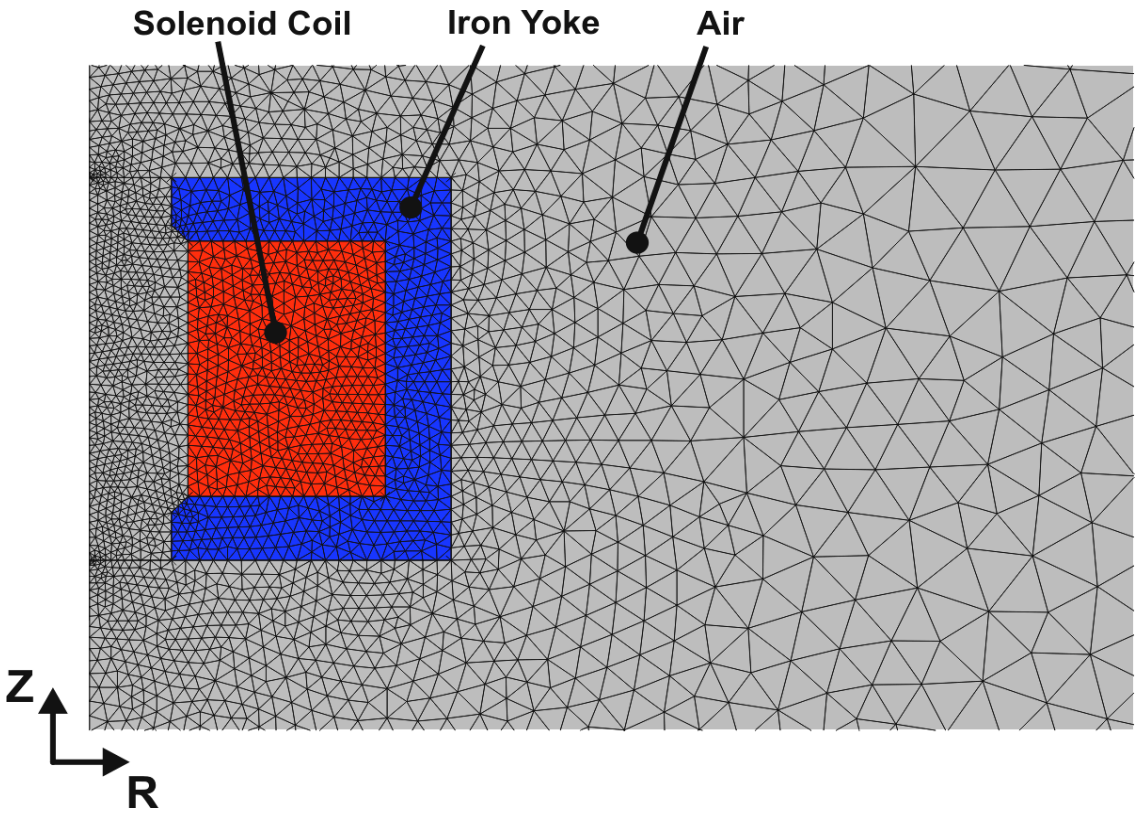

possible, first setting some of the quantities ε, μ, or σ equal to constants if possible, and then deducing a second order differential equation. This second-order differential equation for some intermediate function (typically a vector potential, scalar potential, or both) can then be discretized and numerically solved for realistically shaped structures by means of finite difference, finite element, or integral methods. The finite element method is based on division of the domain of these equations (volume of space in which the equations are satisfied) into small volumes (the finite elements) as shown in Figure 1. Within each finite element a simple polynomial is used to approximate the solution.

Consider first a Poisson equation describing an electric potential function Φ:

$$\vec{\nabla} \cdot \vec{E} = -\vec{\nabla} \cdot \vec{\nabla}\Phi = \frac{\rho}{\varepsilon_0} \quad . \tag{19.2}$$

Such an equation,

$$-\left(\frac{\partial^2}{\partial x^2}\Phi + \frac{\partial^2}{\partial y^2}\Phi + \frac{\partial^2}{\partial z^2}\Phi\right) = \frac{\rho}{\varepsilon_0} \quad , \tag{19.3}$$

can be easily discretized for computations. In order to define Φ, boundary conditions are required; these may be either assigned values of Φ or its normal derivative $\partial\Phi/\partial x$ on a surface. In all electrostatic field examples it is essential that the potential is defined at least at one point in the domain, otherwise an infinite number of solutions could be generated by adding an arbitrary constant to a particular solution.

The situation is slightly different for magnetic problems. In the magnetostatic limit, Maxwell's equations reduce to

$$\vec{\nabla} x \left(\frac{\vec{B}}{\mu}\right) = \vec{j} \quad , \tag{19.4a}$$

$$\vec{\nabla} \cdot \vec{B} = 0 \quad . \tag{19.4b}$$

Since $\vec{B}$ is not "curl free", it follows that the magnetic flux density cannot be represented by the gradient of a scalar potential as in the electrostatic case. It is convenient to split the total field into two parts, a conductor source field and a gradient of a scalar potential, in order to obtain a description of the field in terms of a simple scalar potential:

$$\vec{H} = \vec{H}_s - \vec{\nabla}\Phi \quad \text{with } \vec{\nabla} \cdot \vec{H}_s = 0 \quad . \qquad \textit{Reduced scalar potential} \tag{19.5}$$

The conductor source field intensity can be evaluated separately, for example by the Biot-Savart law

$$\vec{H}_s = \frac{1}{4\pi}\int d^3r' \frac{\vec{j}' x (\vec{r} - \vec{r}')}{\left|\vec{r} - \vec{r}'\right|^3} \quad . \tag{19.6}$$

Introducing the scalar permeability μ and combining $\vec{\nabla} \cdot \vec{B} = 0$ with the above two equations, we have the partial differential equation for Φ:

$$\vec{\nabla} \cdot \mu \vec{\nabla} \Phi - \vec{\nabla} \cdot \mu \vec{H}_s = 0 \quad , \tag{19.7}$$

with $\vec{H}_s$ calculated from eqn. (19.6).

The splitting of the magnetic field into a "curly" source part and a reduced scalar potential part has finally reduced the problem to a purely scalar one. Equation (19.7), like the Poisson equation for electrostatic fields, can be solved using the finite element method. Unfortunately, this method leads to large computational errors, especially in volumes where $\vec{H}_s$ and $\vec{\nabla}\Phi$ strongly cancel each other. This difficulty can be avoided when currents are not flowing in the magnetic materials. Exterior to the volumes where current flows the total field can be represented using the "total scalar potential" Ψ:

$$\vec{H} = -\vec{\nabla}\Psi \quad , \qquad \textit{Total scalar potential} \tag{19.8}$$

which satisfies:

$$\vec{\nabla} \cdot \mu \vec{\nabla} \Psi = 0 \quad . \tag{19.9}$$

By combining the two representations (the total and the reduced scalar potentials) cancellation difficulties can be completely avoided. Therefore, the minimal combination for magnetic field simulations consists of using the reduced potential plus $\vec{H}_s$ only inside volumes where currents flow and using the total scalar potential everywhere else. On the interface between the total and reduced potential spaces the two potentials are linked together (internally in the computer code) by applying the conditions of normal B and tangential H continuity. This procedure has important consequences for setting up the simulation model. The reduced potential volume should completely enclose any coils in such a way that it is not possible to find a closed path in total potential which encloses a non-zero current. In other words any closed contour integral of H through any total scalar region must approach zero, since otherwise the solution would be multi-valued.

.19.2 Solution strategy in 2D

In 2D simulations, using either cylindrical or rectangular coordinates, the solution strategy for Maxwell's equations can be dramatically simplified compared to the general 3D strategy outline above. Since the primary topic of this report is the calculation of axisymmetric solenoid systems, we will describe the 2D simulation method in more detail, and will give a few computation examples in the next chapter. Still, for a solenoid-based particle accelerator design, 3D simulations would be necessary in regions where several solenoid beamlines are transversely merged into a single beamline, or where solenoid lead effects become critical.

By using a vector potential, $\vec{B} = \vec{\nabla} x \vec{A}$, we can rewrite the relevant Maxwell's equation in the magnetostatic limit:

$$\vec{\nabla} x (\frac{1}{\mu} \vec{\nabla} x \vec{A}) = \vec{j} \ . \tag{19.10}$$

Imposing gauge condition $\vec{\nabla} \cdot \vec{A} = 0$, and taking into account the now two-dimensional symmetry of the physical geometry, equation (19.10) can be rewritten:

$$\frac{\partial}{\partial z} \frac{1}{\mu} \frac{\partial A}{\partial z} + \frac{\partial}{\partial r} \frac{1}{\mu} \frac{1}{r} \frac{\partial (rA)}{\partial r} = -j \ , \tag{19.11}$$

Where only the θ components (A, j) are present. In two dimensions Maxwell's equations reduce to a scalar equation, which can be easily solved by computational methods. Contrary to three-dimensional simulations where the model geometry has to be divided into regions of "total" and "reduced" scalar potentials to gain a numerical scalar potential description, the equation to be solved in 2D is automatically of an effectively scalar nature. No division into different regions has to be performed in 2D. The magnetic field components are simply

$$B_r = -\frac{\partial A}{\partial z} \ , \tag{19.12a}$$

$$B_z = \frac{1}{r} \frac{\partial (rA)}{\partial r} \ . \tag{19.12b}$$

This has an important consequence: Contrary to three dimensions, in a planar two-dimensional simulation the equipotential lines of the vector potential (which is a scalar quantity in 2D) are equal to the magnetic field lines (for axisymmetric simulations a modified scalar potential $r \cdot A$ has to be used). That fact makes two-dimensional simulations much more intuitive and accessible from a practical point of view compared to any three-dimensional simulation.

.19.3 Example

Figure (2) shows a typical axisymmetric model setup of a solenoid with an iron enclosure. Figure (3) shows the finite element mesh as generated by Tosca© -2D. The material properties have to be defined in the code. For air and the copper conductor the relative permeability is set to 1, for the return yoke a typical B-H magnetization curve for 1010 carbon steel, as shown in figure 4, is used.

As shown in figure 5, correct boundary conditions have to be set to solve the problem numerically. For axisymmetric simulations the center axis requires a "tangential field only" (Dirichlet) boundary condition. The air volume enclosing the region of interest has to be chosen as large as possible to minimize the effect of the far-end boundary conditions. It is always a good practice to check that the far-field boundaries have been placed far enough by changing the normal field to tangential field boundaries. The change in the magnetic field in the region of interest should be minimal, otherwise the outer boundaries have not been moved far enough out. In the example the current density in the coil field region has been set to $4.7x10^6$ A/m^2. All that information is stored in a binary database file which is processed by the analysis module of the Tosca© code.

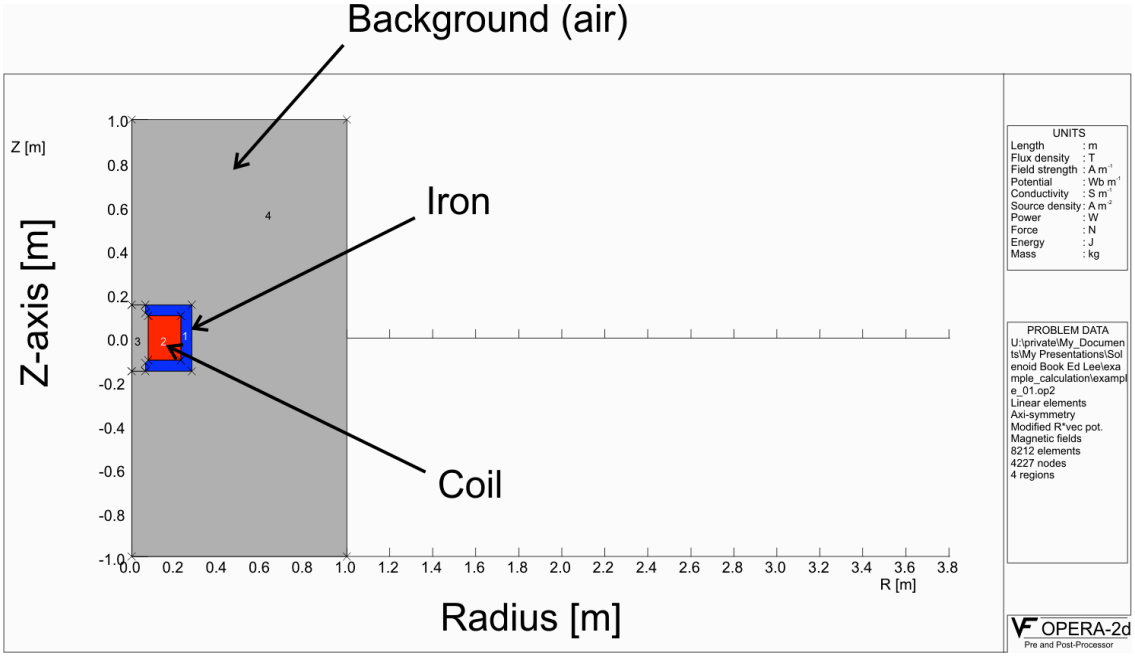
Background (air)
Iron
Coil
Z [m]
Z-axis [m]
Radius [m]
R [m]
UNITS
Length : m
Flux density : T
Field strength : A m-1
Potential : Wb m-1
Conductivity : S m-1
Source density : A m-2
Power : W
Force : N
Energy : J
Mass : kg
PROBLEM DATA
U:\private\My_Documents\My Presentations\Solenoid Book Ed Lee\example_calculation\example_01.op2
Linear elements
Axi-symmetry
Modified R*vec pot.
Magnetic fields
8212 elements
4227 nodes
4 regions
OPERA-2d
Pre and Post-Processor

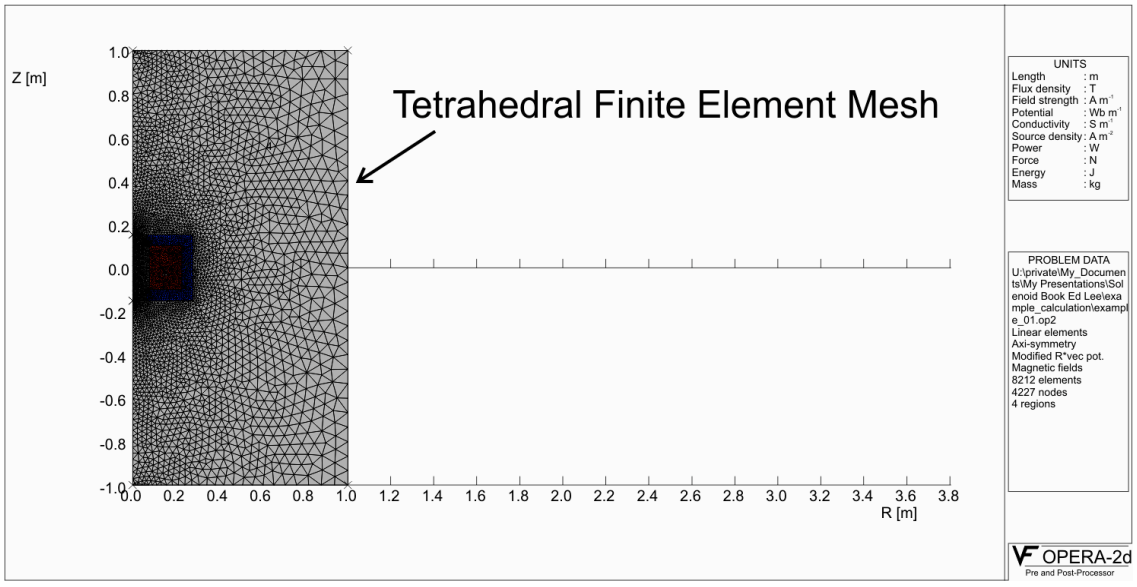
Tetrahedral Finite Element Mesh
Z [m]
R [m]
UNITS
Length : m
Flux density : T
Field strength : A m-1
Potential : Wb m-1
Conductivity : S m-1
Source density : A m-2
Power : W
Force : N
Energy : J
Mass : kg
PROBLEM DATA
U:\private\My_Documents\My Presentations\Solenoid Book Ed Lee\example_calculation\example_01.op2
Linear elements
Axi-symmetry
Modified R*vec pot.
Magnetic fields
8212 elements
4227 nodes
4 regions
OPERA-2d
Pre and Post-Processor

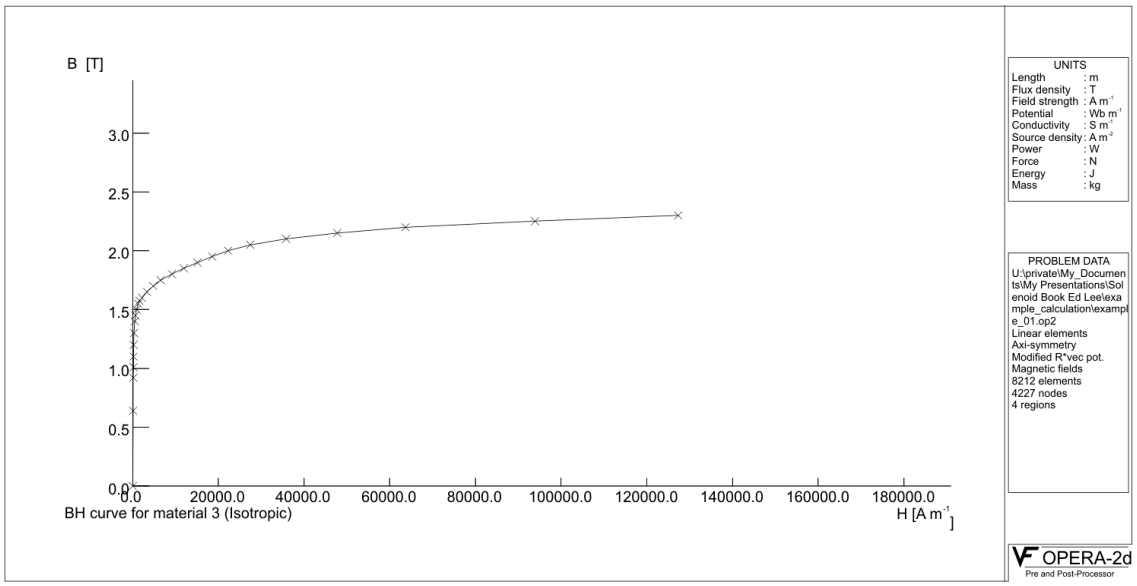
B [T]
3.0
2.5
2.0
1.5
1.0
0.5
0.0
0.0
20000.0
40000.0
60000.0
80000.0
100000.0
120000.0
140000.0
160000.0
180000.0
BH curve for material 3 (Isotropic)
H [A m-1]
UNITS
Length : m
Flux density : T
Field strength : A m-1
Potential : Wb m-1
Conductivity : S m-1
Source density : A m-2
Power : W
Force : N
Energy : J
Mass : kg
PROBLEM DATA
U:\private\My_Documents\My Presentations\Solenoid Book Ed Lee\example_calculation\example_01.op2
Linear elements
Axi-symmetry
Modified R*vec pot.
Magnetic fields
8212 elements
4227 nodes
4 regions
OPERA-2d
Pre and Post-Processor

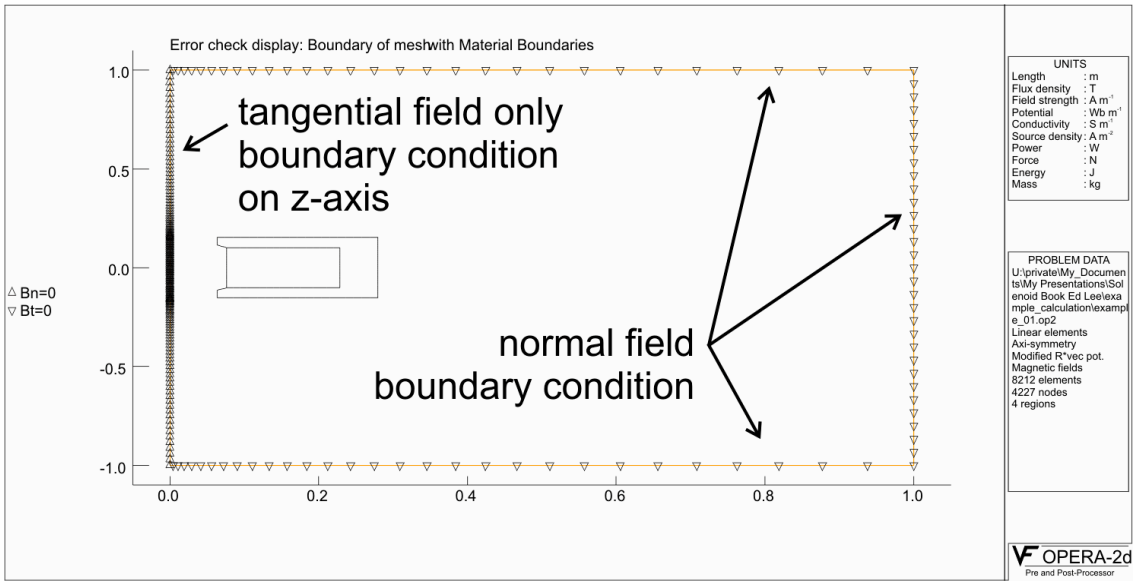
Error check display: Boundary of meshwith Material Boundaries
△ Bn=0
▽ Bt=0
tangential field only
boundary condition
on z-axis
normal field
boundary condition
1.0
0.5
0.0
-0.5
-1.0
0.0
0.2
0.4
0.6
0.8
1.0
UNITS
Length : m
Flux density : T
Field strength : A m-1
Potential : Wb m-1
Conductivity : S m-1
Source density : A m-2
Power : W
Force : N
Energy : J
Mass : kg
PROBLEM DATA
U:\private\My_Documents\My Presentations\Solenoid Book Ed Lee\example_calculation\example_01.op2
Linear elements
Axi-symmetry
Modified R*vec pot.
Magnetic fields
8212 elements
4227 nodes
4 regions
OPERA-2d
Pre and Post-Processor

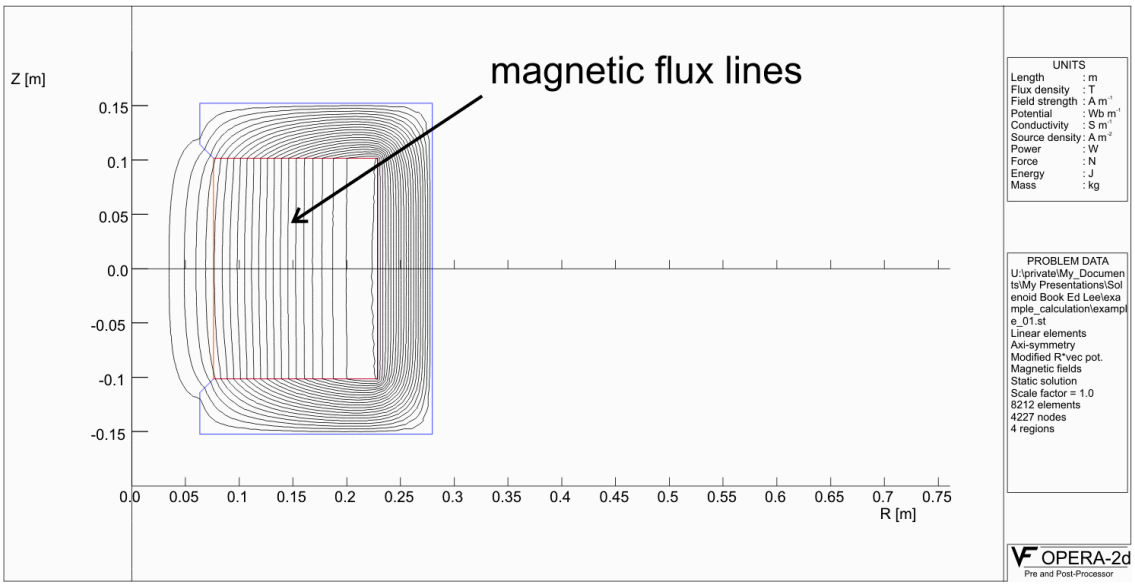

Figure 6: Model geometry with the magnetic flux lines displayed.

Computation of the vector potential proceeds iteratively for each mesh point. The computation proceeds in the iron region with the determination of vector potential, magnetic induction, and permeability at each mesh point. The vector potentials A are first computed at all points by assuming a constant value of permeability, then the components of the induction B are determined as partial derivatives of A, and the permeability values as a function of the absolute values of B are read from a B-H curve table. Then the whole process is repeated with adjusted permeability values: cycling is continued until the changes in permeability are all below a specified value.

Once the field computation has been performed the database is read into a post-processor for further evaluation. Figure 6 shows the model geometry with the magnetic flux lines displayed. Figure 7 shows contour zones of the total magnitude of the magnetic flux density, and figure 8 shows a read out of the magnetic field on axis.

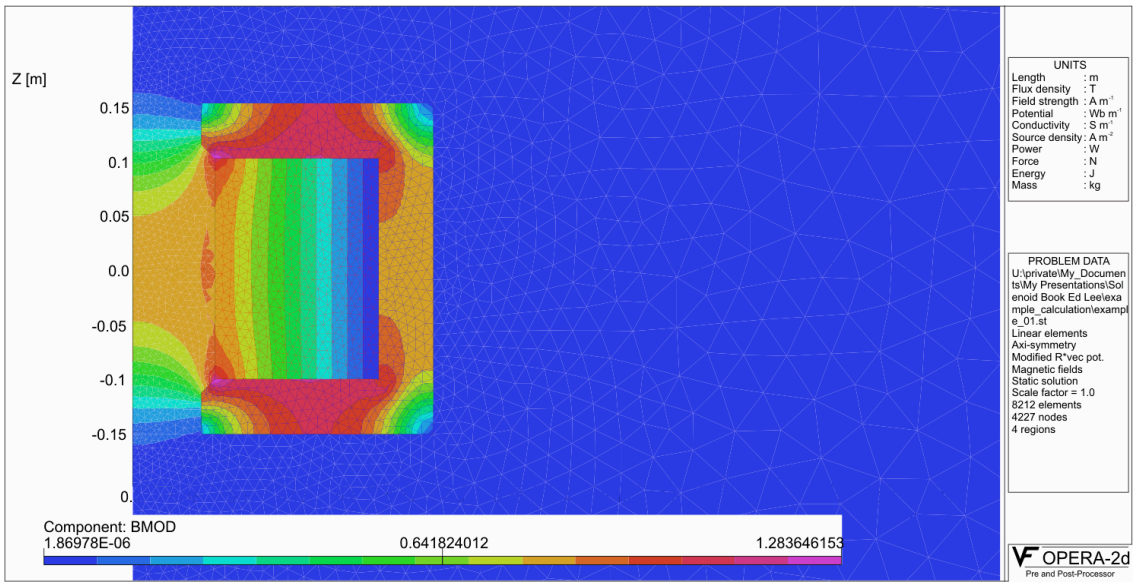

Figure 7: Colored contour zones of the absolute magnitude of the magnetic flux density. As can be clearly seen, most of the magnetic return flux is concentrated in the iron yoke, which starts to saturate. Finite element analysis is best suited for predicting the magnetic field distribution in cases saturated materials with non-linear magnetic properties are present.

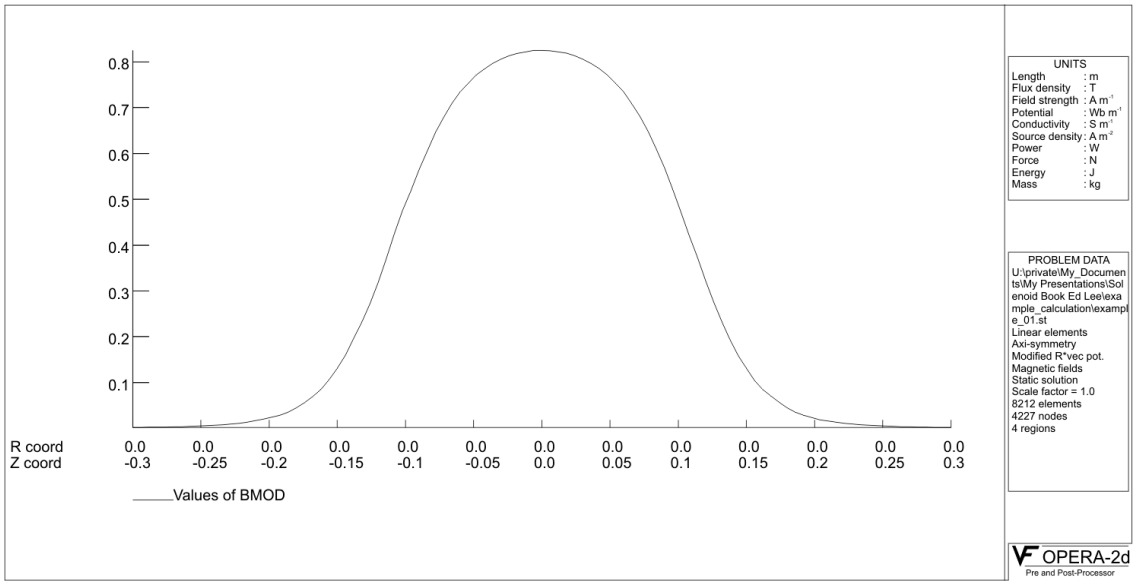

Figure 8: Magnetic flux density in Tesla along the solenoid axis.

20. Application of Tosca© to Induction Linac Design

20.1 Introduction

Recently there has been renewed interest in relatively low energy modular induction accelerators to drive close-coupled HIF targets (~75 MV acceleration voltage of Ar^{8+}, corresponding to 600 MeV kinetic energy). Similar, smaller-scale designs are suggested for a possible facility to perform high energy density physics experiments. These designs utilize solenoid beam transport because of its favorable scaling at the desired ion mass and kinetic energy.

An example "modular solenoid driver" [20-1] would consist of 40 beamlines (20 on each side of the final focus chamber). Each beamline would have a high current Ar^{8+} injector and a pre-bunch section to compress the beam for injection into a solenoid-based modular induction linac. The total linac length would be only 75 meters. The accelerated beams, which have an approximately 15% energy tilt imposed, compress in a neutralized drift section (~260 meters long) before final radial compression inside a liquid-vortex flibe chamber with a solenoid focusing magnet set.

Figure 1 shows the mechanical layout of the high-energy end of such a modular solenoid linac. The main dimensions of a linac cell are given in figure 2. The transport solenoids are superconducting Nb_3Sn magnets producing 12 Tesla peak axial magnetic field. Finite-element based electromagnetic simulation tools are utilized in several design aspects of the linear accelerator:

1. The solenoids are embedded inside induction cores of high permeability. To shield the solenoid return flux from the induction cores, the superconducting winding structure is enclosed by a thick, soft-magnetic steel shell. Finite element codes are reliable tools for calculating the effects of the permeable materials and allow optimization of the acceleration cell geometry.
2. The ion beams exiting the 20 modular solenoid linacs must be matched into the focusing system leading to the fusion target. Three-dimensional finite element codes can reliably calculate the dipole and higher-order field contributions of the solenoid magnetic fields at the end of the linac structure, especially if permeable materials are present to channel the linac fields' return flux.
3. Finite element codes are used to design the superconducting winding pack. They allow the exact coil dimensioning using critical current load lines.
4. If one solenoid along a linac string quenches, the forces on the neighboring solenoids will be imbalanced. Finite element codes allow one to calculate these forces and to dimension a sufficient support system. The electromagnetic simulation models are directly linked with structural models to design the solenoid clamping structure.

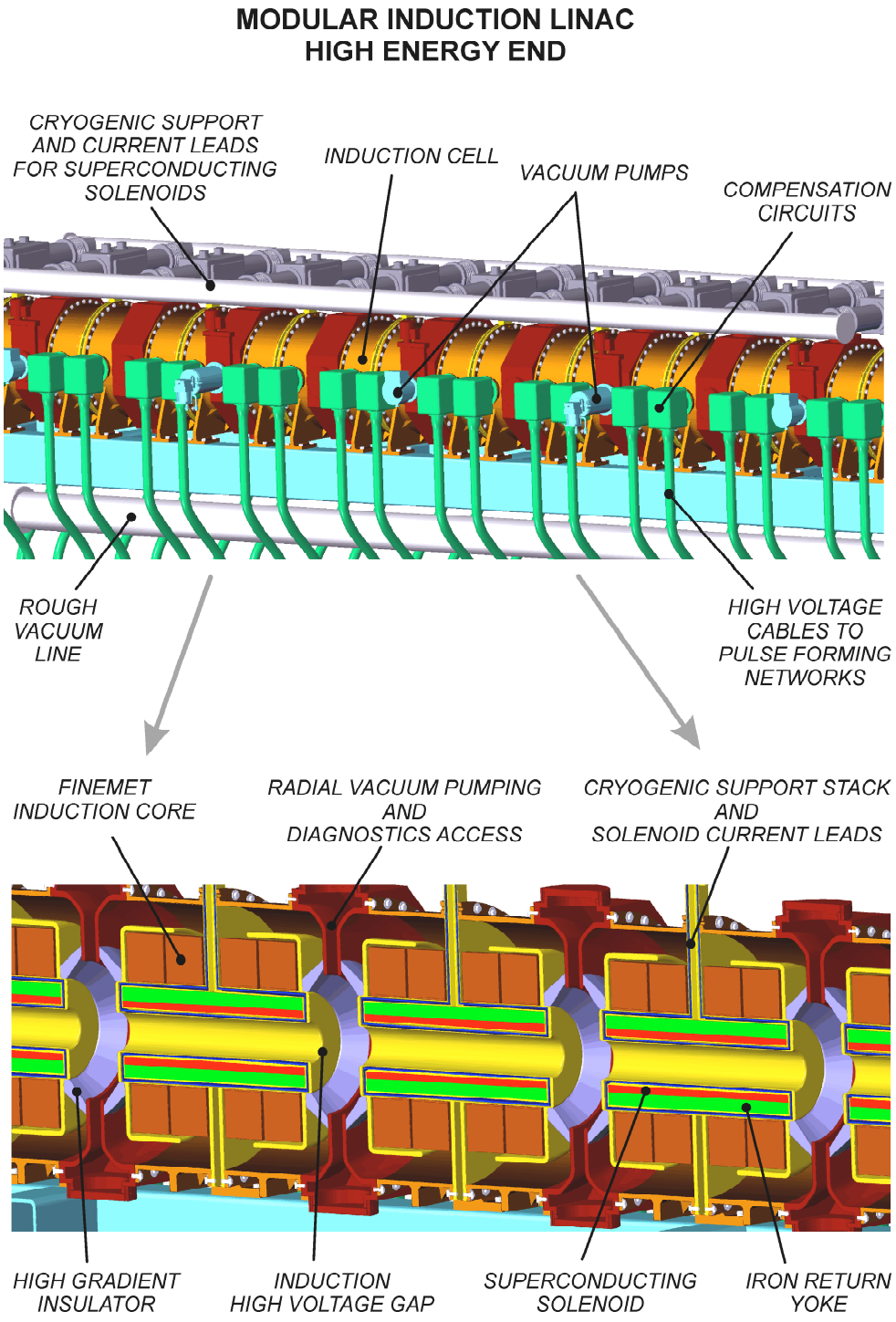

Figure 1: A modular solenoid driver would use strong solenoids for focusing the heavy ion beam.

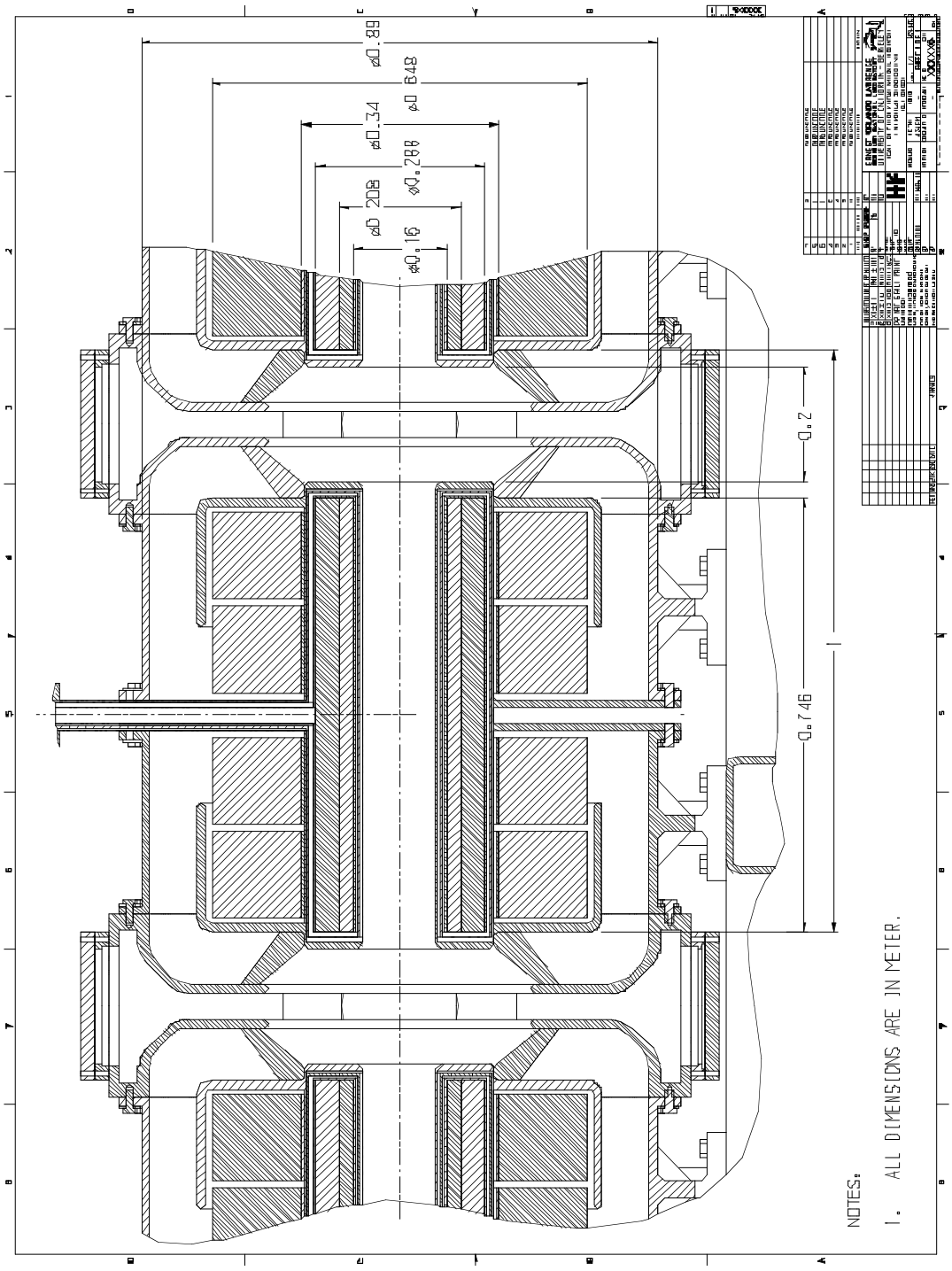

Figure 2: 2D drawing showing the main dimension of the driver induction cell.

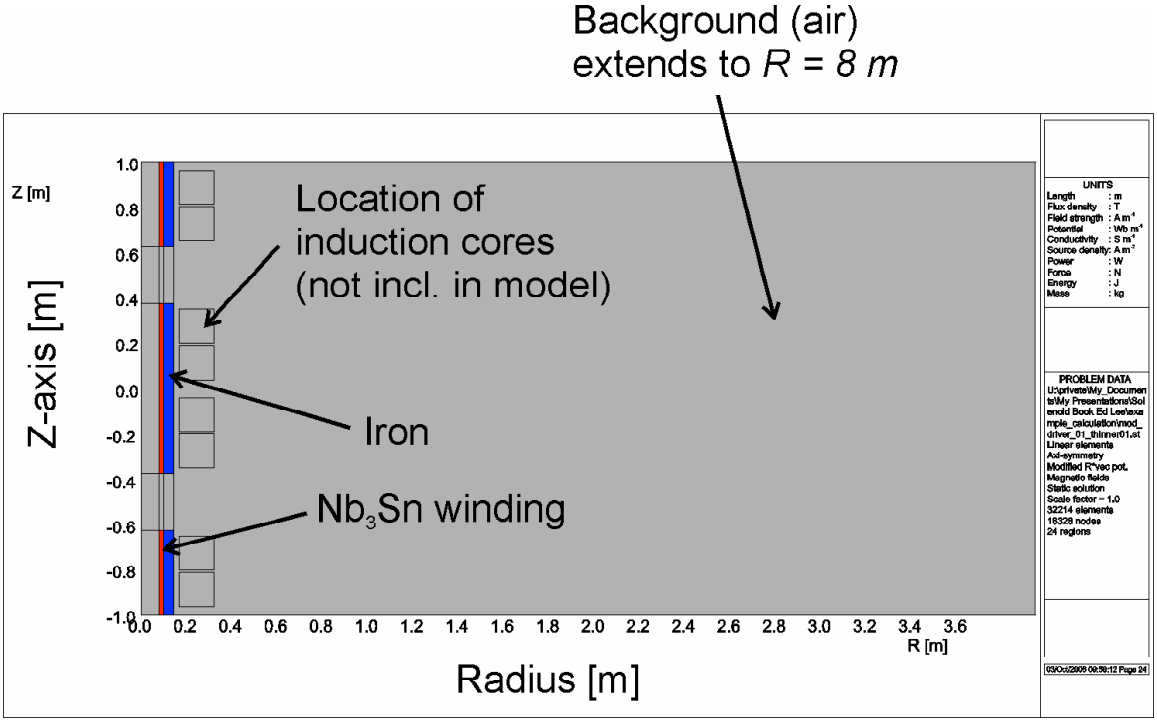

Figure 3: Example FEA setup of a modular solenoid driver.

20.2 Example

As an example of how electromagnetic modeling can be utilized to optimize the modular solenoid driver architecture, we look at the effect of adding iron outside the superconducting solenoid winding. We will also discus how to specify the superconducting winding structure.

Figure 3 shows a simulation setup for an infinitely long solenoid string consisting of a (thin) superconducting wire pack surrounded by an iron cylinder. The rest of the model consists of air with a relative permeability equal to 1 the location of the induction cells is indicated, but we will not include their material properties in this example. The beam travels along the vertical axis, and the radial coordinate is the horizontal axis.

Such a simulation should strongly take advantage of the model symmetry. First of all the simulation is 2D axisymmetric with the beam axis as symmetry axis. Second, because of the infinite nature of the problem the top and bottom model boundaries are symmetry planes through the centers of the solenoids. The correct numerical boundary conditions are shown in figure 4. The background air (vacuum) volume extends radially far outside to minimize the influence of the far field boundary condition, which was set to tangential $B_r = 0$.

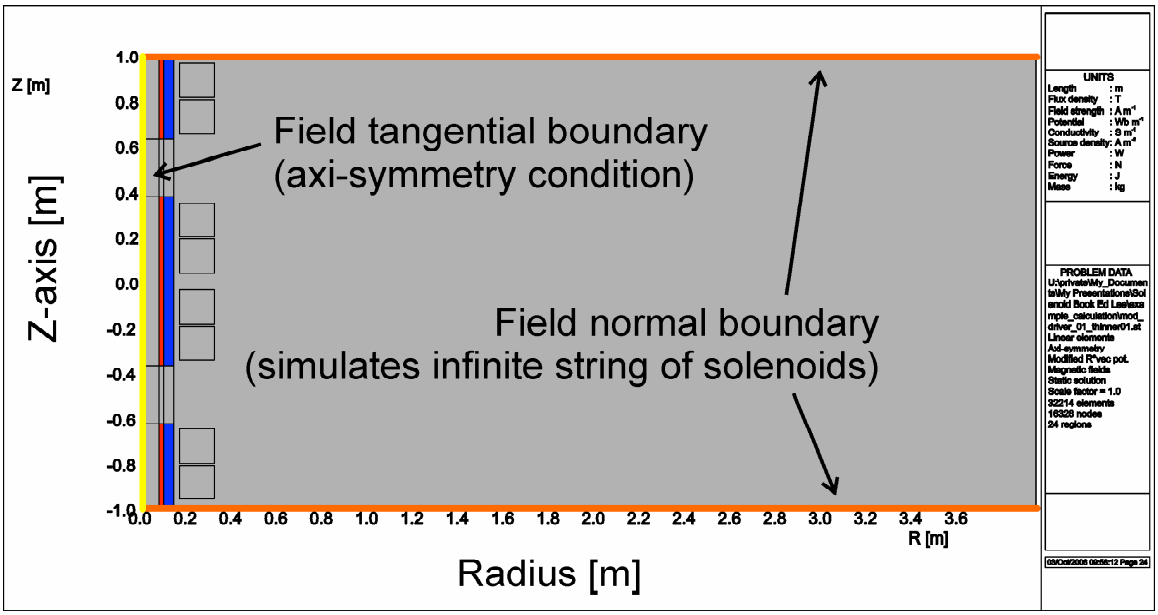

Figure 4: The FEA boundary conditions are set to simulate an infinite string of solenoids. A 2D simulation is sufficient because of the axisymmetric nature of the problem.

Figure 5 shows in more detail the region around one single solenoid and the finite element grid generated by the Tosca© 2D simulation code. To enhance the accuracy of the simulation model, regions close to the beam axis - including the solenoid winding and the iron regions - are modeled using mapped hexagonal finite elements. The background air model uses tetragonal elements, which allow gradually increasing element sizes. In that way the model can have a very fine grid around the areas of interest and a coarser grid at the far field boundaries.

After meshing the problem geometry the material and conductor properties have to be defined. Figure 6 shows the permeability curve for 1010 steel, a soft magnetic steel used for building electromagnets.

Figure 7 shows a graph of critical current densities for different superconducting cable materials [*2*]. The blue curve with blue squares shows the critical current line for Nb_3Sn at a temperature of 4.2 Kelvin, the temperature of the liquid helium coolant. The critical current density is the maximum current density a superconducting wire can transport without loosing its superconductivity, which is dependent on the applied magnetic field. The higher the magnetic field the lower the critical current density. Nb_3Sn has similar critical current densities as NbTi but can be operated at much higher applied magnetic fields.

It is important to realize that the critical current densities are shown for single stranded superconducting wire. The actual current densities used as input in the simulations to define the conductor regions are significantly lower. Figure 8 shows a

cross sections of a few actual superconducting wires. It shows the superconducting wire strands embedded inside a copper matrix whose purpose is two-fold.

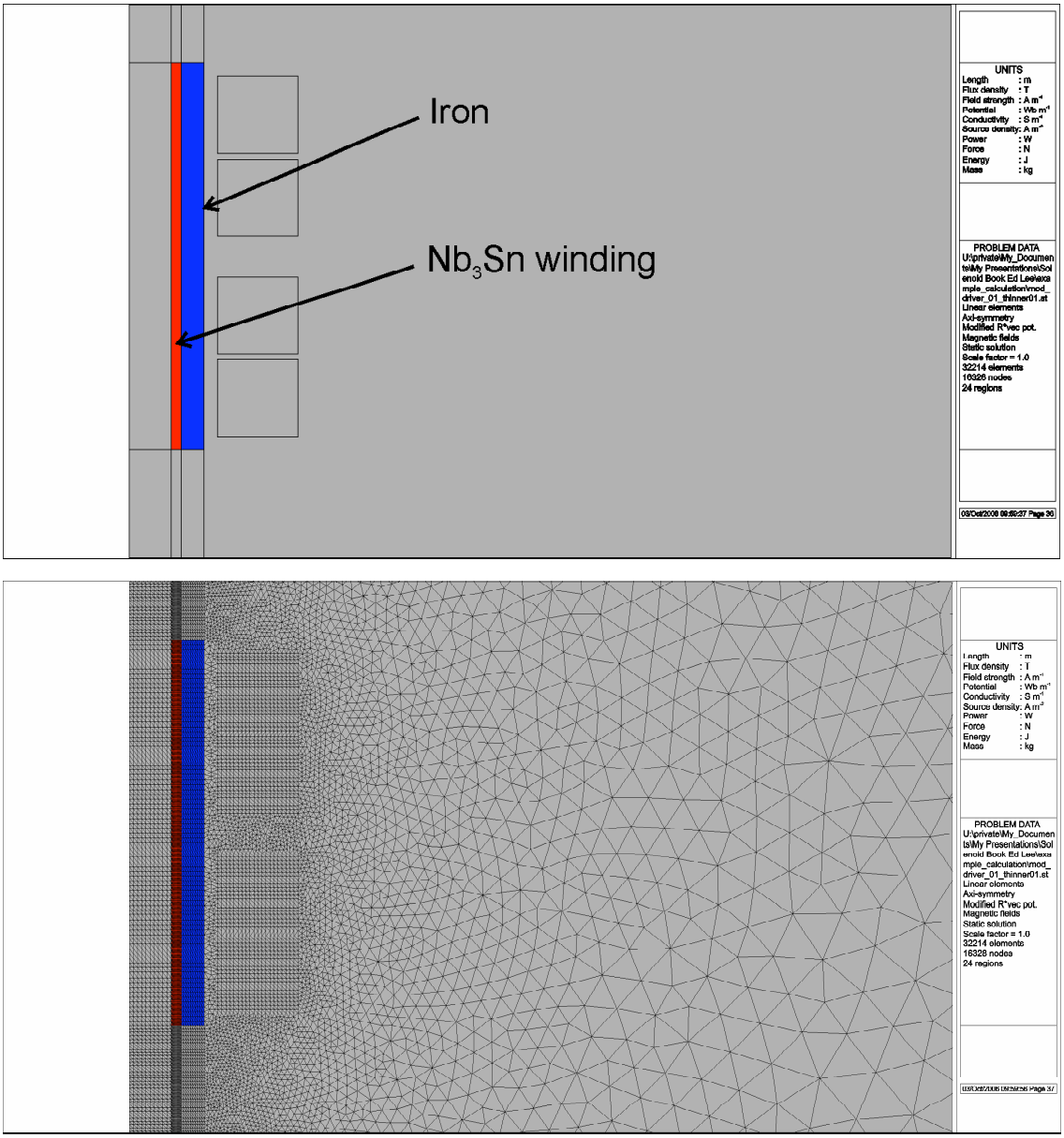

Figure 5: Example 2D FEA grid of a solenoid magnet.

First it helps to locally stabilize the superconducting wire. On a microscopic scale, the superconducting state is fluctuating, and a sufficiently sized copper matrix helps to stabilize the superconducting condition. Second, the wire has to be able to transport all the current in cases where the wire quenches and superconductivity is lost entirely. Enough copper must be available to transport the current without melting the wire.

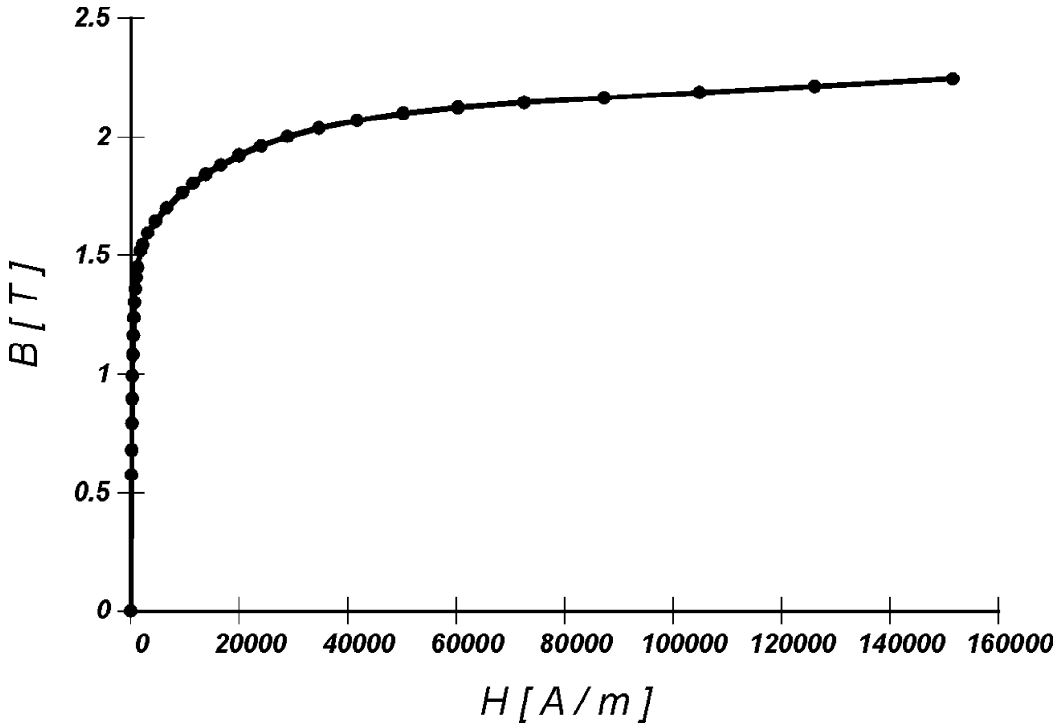

Figure 6: BH curve for 1010 steel, a soft magnetic steel used for building electromagnets.

In designing a magnet, what really matters is the overall "engineering current density". It is given by the superconducting strand critical current density times the superconducting material to copper ratio times the packing factor of the actually wound superconducting wire. Figure 8 demonstrates the packing of commercial round wires in a magnet winding.

$$J_{overall} = packing\,factor \cdot J_{wire} = packing\,factor \cdot \frac{1}{Cu/SC\ ratio} J_c$$

with

$J_{overall}$ ...	"engineering current density"
packing factor ...	takes account of space occupied by insulation, eventual cooling channels, mechanical reinforcement, epoxy, etc.
Cu/Sc ratio ...	ratio of copper to superconducting material Table 1 determines the maximum Cu/SC ratio by limiting the maximum current density to be carried by the copper matrix to 1500 A/mm@ in case of a complete quench.
J_c ...	critical current density for single superconducting strand

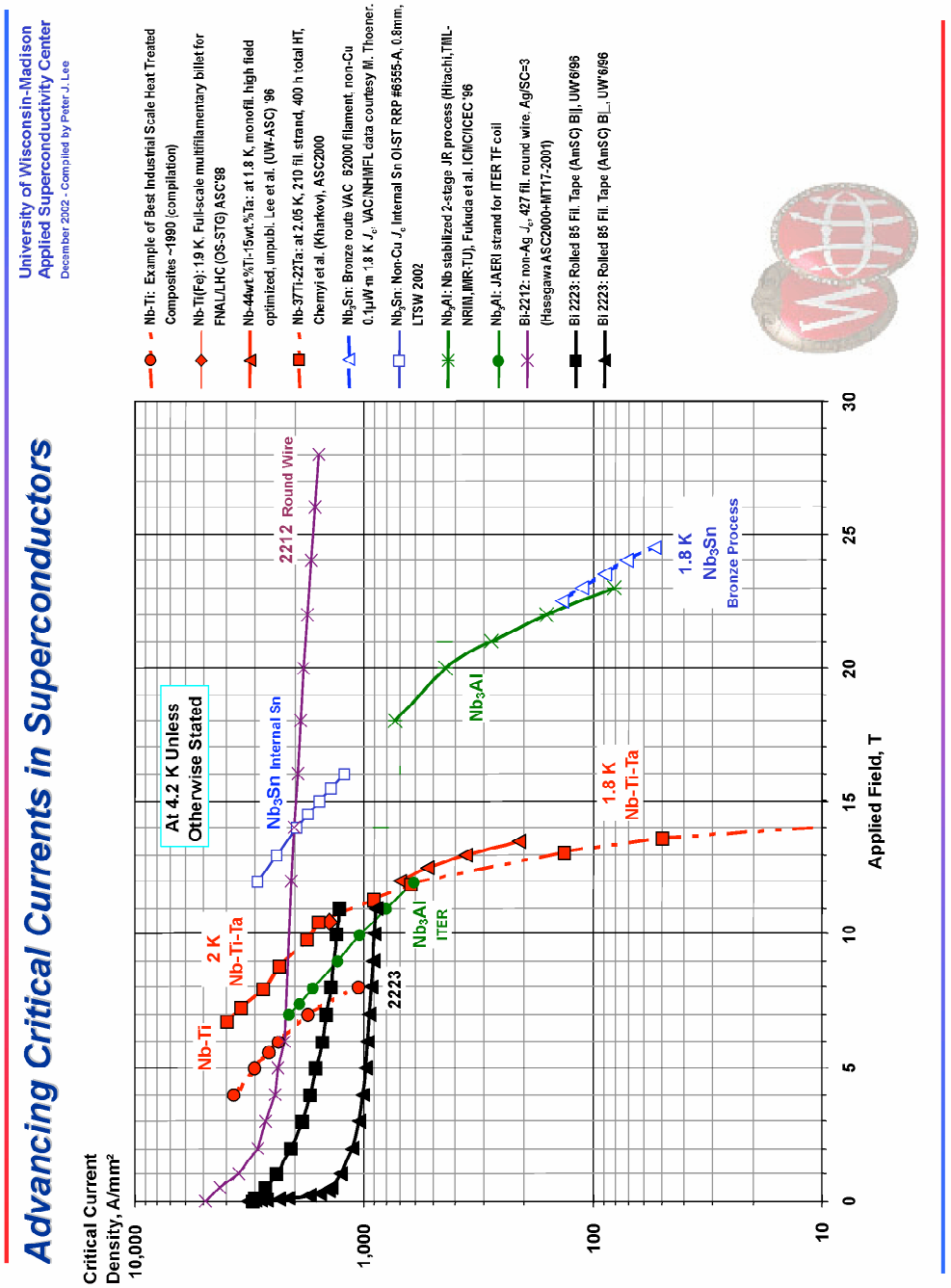

Figure 7: Critical current densities for commercial superconducting wires [2]. The blue curve with blue squares shows the critical current line for Nb_3Sn at 4.2K.

Table 1 summarizes the actual "engineering current densities used to specify the conductors in the simulations dependent on the applied magnetic field. An additional

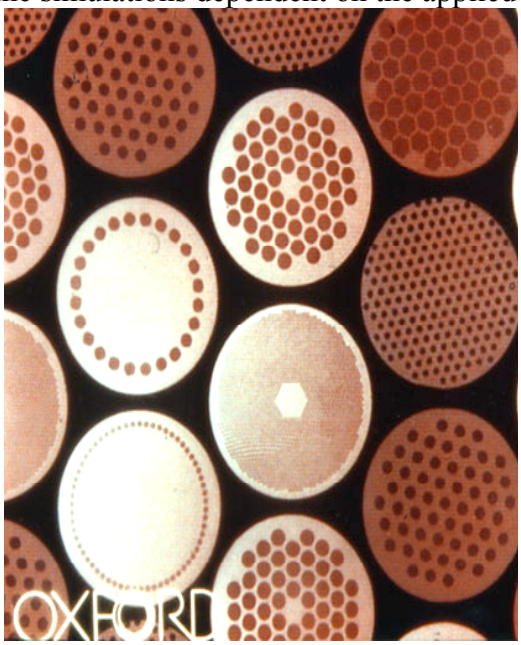

Figure 8: Cross section of various actual superconducting wires. The superconducting filaments, which are actually twisted, are embedded inside a copper matrix. Additional space around the wires is needed for insulation, structural epoxy, or cooling channels.

30% safety margin is applied to the engineering current densities to account for winding strain and temperature fluctuations. Depending on the actual mechanical solenoid design an even larger temperature safety margin may be necessary at higher applied magnetic fields.

Figure 9 displays the field lines of the resulting solenoid beam transport channel. Figure 10 shows the axial magnetic field strength along the beam center axis. The field ripple due to the fairly large magnet spacing, which is necessitated by the wide induction acceleration gap (1 MV/m gradient), is clearly visible.

B [T]	**J_c [A / mm^2]**	**Cu/SC Ratio (*)**	**J_{wire} [A / mm^2]**	**$J_{overall}$ [A / mm^2]**	**with 30% margin (**) [A / mm^2]**
5	9454	6.30	1295	906	634
6	7766	5.18	1257	880	616
7	6431	4.29	1216	851	596
8	5347	3.56	1171	820	574
9	4446	2.96	1122	785	550
10	3689	2.46	1066	746	523
11	3048	2.03	1005	704	493
12	2500	1.67	938	656	459
13	2031	1.35	863	604	423
14	1631	1.09	781	547	383
15	1289	0.86	693	485	340

(*) for a maximum current density of 1500 A/mm^2 in the copper matrix

(**) margin for winding strain and temperature fluctuations

Table 1: Engineering current densities ($J_{overall}$) for Nb_3Sn at different magnetic fields.

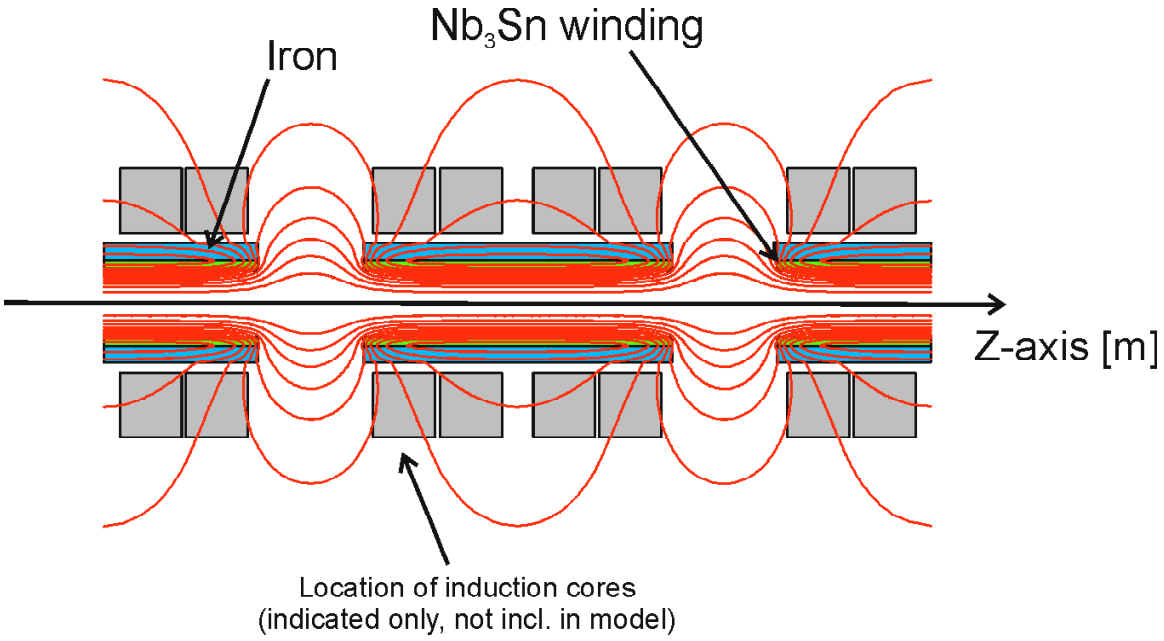

Figure 9: Magnetic flux lines for a string of solenoids.

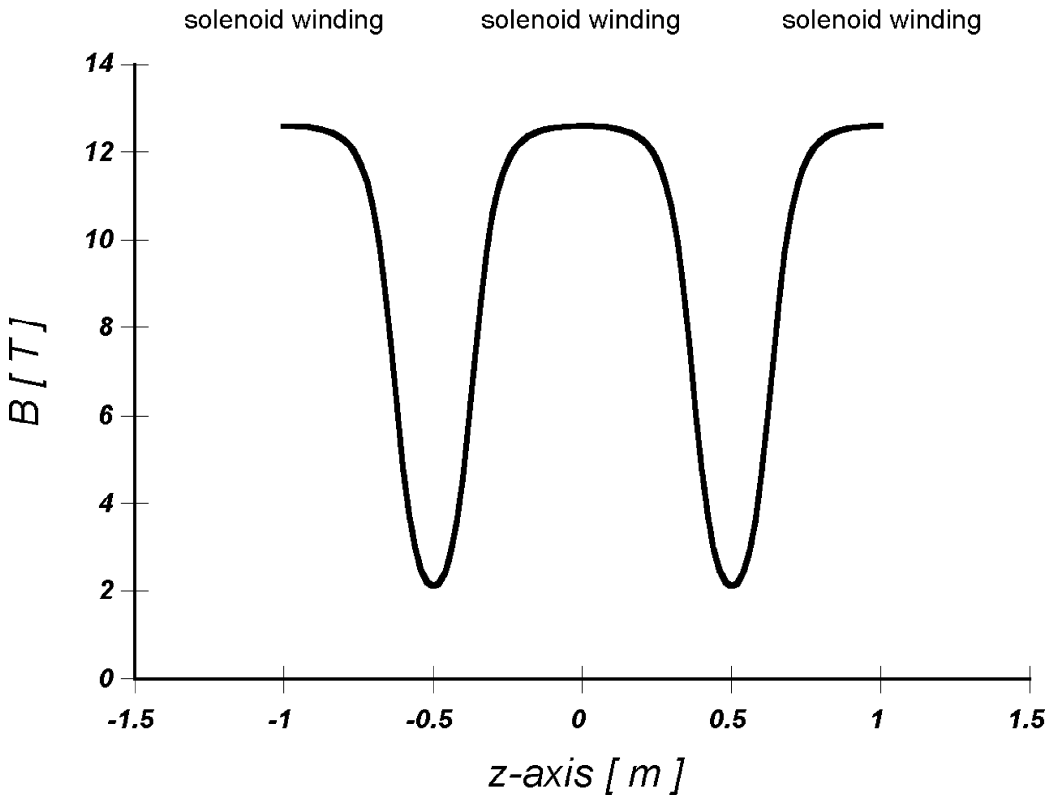

Figure 10: Magnetic field along the beam center axis.

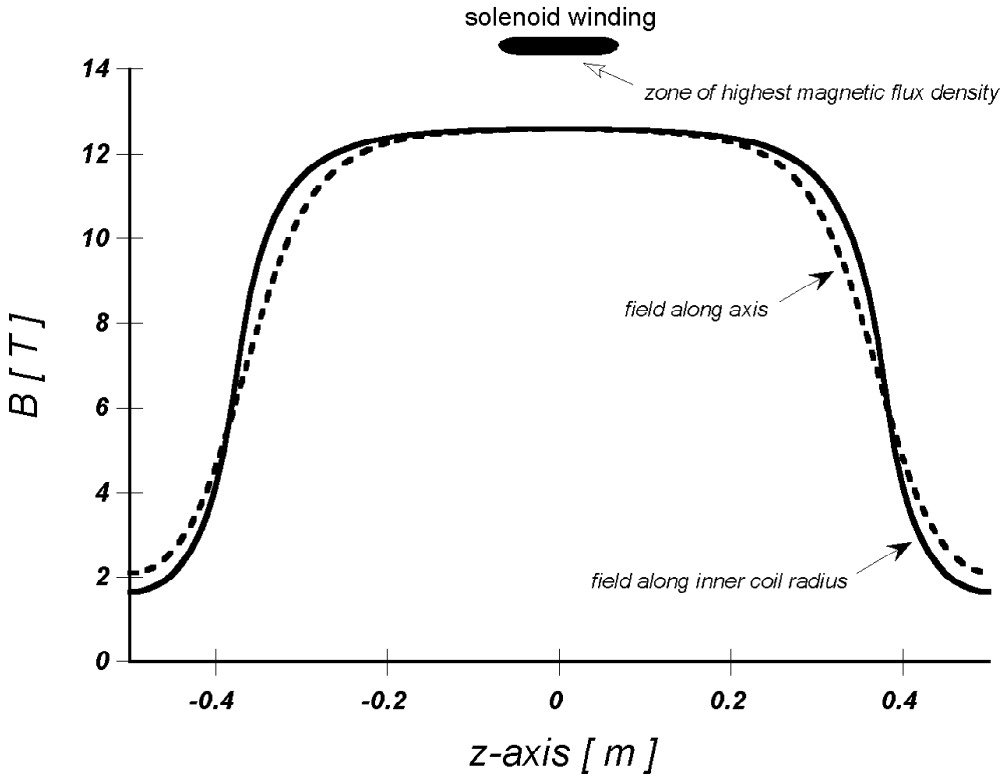

Figure 11: Comparison of |B| along the beam center axis and along the solenoid inner radius Indicated is the zone of highest magnetic field inside the solenoid winding.

Figure 11 shows B along the beam center axis and along the inner coil radius. The field non-uniformity must be included in ion optics simulations. Indicated in figure 11 is the location of the maximum magnetic field for a long solenoid. The solenoid current density must be below the "engineering" critical current density for the magnetic field encountered in that region.

Finite element analysis plays an important role in reliably predicting magnetic fields inside permeable materials. In the above design the iron region around the magnet winding is fully saturated (magnetic field > 2 Tesla), as can be seen in figure 12. Plotted in figure 13 is the magnetic field versus radius (at z=0.0, the middle of the solenoid, see figure 12) for different iron thicknesses. The magnetic field is constant within the solenoid bore, drops within the winding pack, and reverses its direction in the iron and the surrounding air. Since the iron is fully saturated it cannot completely shield the magnetic field return flux from the induction cells and the adjacent structures. With a 4cm return iron yoke the air magnetic field at the location of the induction cells would be around 0.2 Tesla (see figure 14).

Increasing the iron thickness is the only option to further reduce the return field. That effect can be seen in figure 14. A significant thickness is required to shield a 12 Tesal solenoid field from the induction cells. Currently it is not clear if total shielding is

required to maintain the full flux swing inside the induction cells since the induction cell magnetization is perpendicular to the solenoid magnetization direction. In addition, the induction cell magnetization is a transient effect compared to the DC magnetization caused by the solenoid.

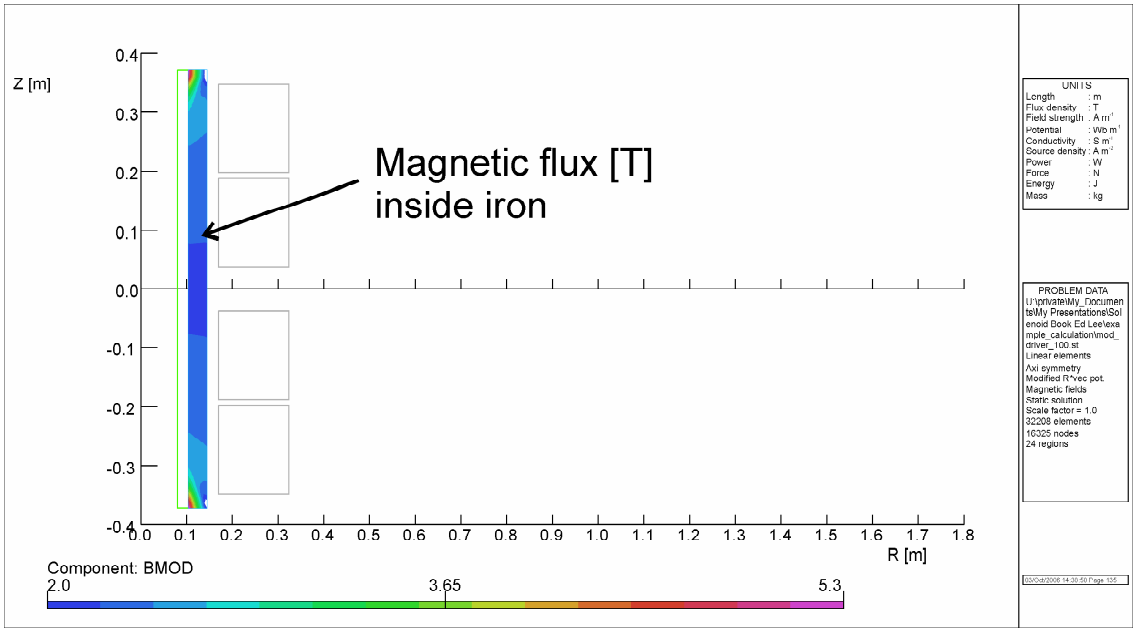

Figure 12: The solenoid iron return yoke is fully saturated.

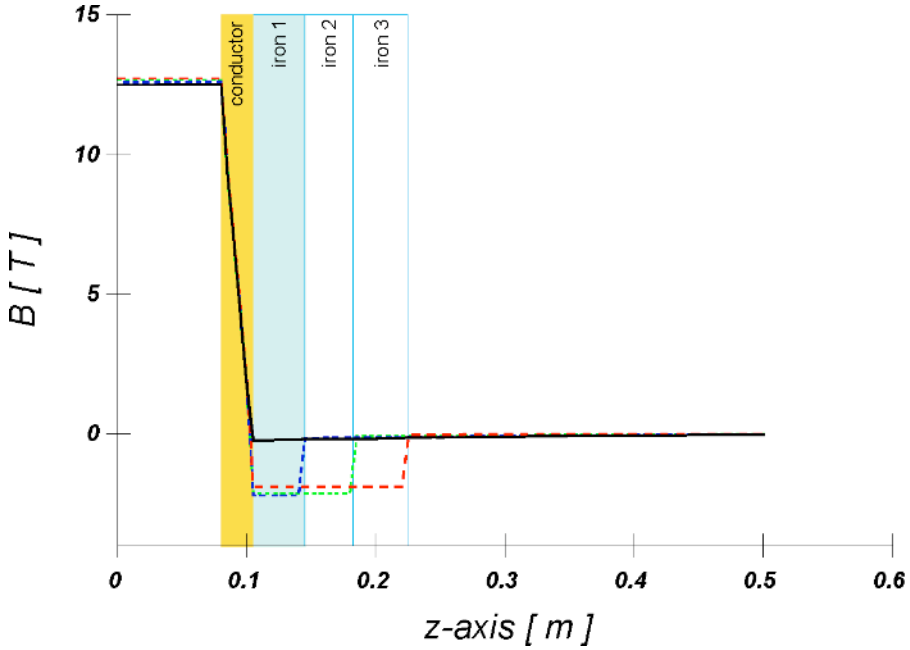

Figure 13: Magnetic field (in solenoid center) versus radius for different iron thicknesses. See figure 14 for more details.

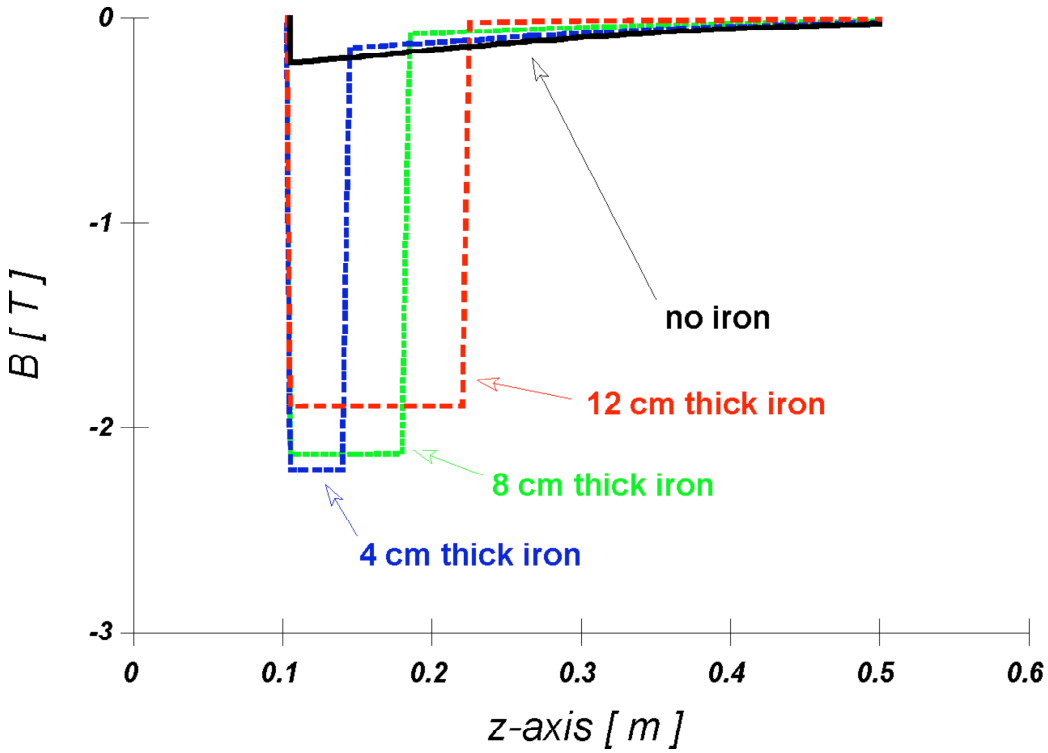

Figure 14: Solenoid return field in the vicinity of the induction cells for different iron return yoke thicknesses.

References

20-1 Grant Logan: "What product might a renewal of Heavy Ion Fusion development offer that competes with methane microbes and hydrogen HTGRs?" internal HIF-VNL report, May 1, 2006, LBNL-61905.

20-2 Applied Superconductivity Center, University of Wisconsin-Madison, http://www.asc.wisc.edu/ or http://magnet.fsu.edu/~lee/plot/plot.htm\

21. Biot-Savart Formula

The Biot-Savart formula in its generalized form is an integration along the wire path, and is therefore an attractive tool when the path is mathematically characterized and there are no permeable materials. It may be used with a CAD program that lays out the wire path, which in general is a vector position $\vec{R}(s)$, where s is path length measured along the wire. This is a good way to compute the fields of magnet leads and other deviations from ideal solenoidal symmetry. The Biot-Savart formula is often presented in

texts as an experimental result for a straight wire and then generalized for an arbitrary wire path. Here we briefly derive it from the magnetostatic Maxwell's eqns. (2.1a,b). It is then used to obtain the fields of a straight wire segment of finite length and of a helix.

21.1 General formula

In the absence of magnetic materials the Cartesian components of a static magnetic field satisfy

$$\nabla^2 \vec{B} = \cancel{\vec{\nabla}\vec{\nabla}\cdot\vec{B}} - \vec{\nabla} x \left(\vec{\nabla} x \vec{B} \right) = -\mu_0 \vec{\nabla} x \vec{J} \ , \tag{21.1}$$

so the Green function solution is

$$\vec{B} = \frac{\mu_0}{4\pi} \int d^3 r' \frac{\vec{\nabla}' x \vec{J}'}{\left| \vec{r} - \vec{r}' \right|} \ . \tag{21.2}$$

An integration by parts gives

$$\vec{B} = \frac{\mu_0}{4\pi} \int d^3 r' \vec{J}' x \vec{\nabla}' \frac{1}{\left| \vec{r} - \vec{r}' \right|}$$

$$= \frac{\mu_0}{4\pi} \int d^3 r' \ \ \vec{J}' x \frac{\left(\vec{r} - \vec{r}' \right)}{\left| \vec{r} - \vec{r}' \right|^3} \ . \tag{21.3}$$

For a wire (of infinitesimal thickness) with path $\vec{R}(s)$ carrying current I, this may be written (Generalized Biot-Savart formula)

$$\vec{B} = \frac{\mu_0 I}{4\pi} \int ds \ \ \hat{e}(s) x \frac{\left(\vec{r} - \vec{R}(s) \right)}{\left| \vec{r} - \vec{R}(s) \right|^3}, \tag{21.4}$$

where $\hat{e}(s)$ is the unit vector along the wire in the direction of the current:

$$\hat{e}(s) = \frac{d\vec{R}(s)}{ds} \ . \tag{21.5}$$

That $\hat{e}$ is a unit vector is apparent from the definition of arc length,

$$(ds)^2 = \left|d\vec{R}\right|^2 = (dR_x)^2 + (dR_y)^2 + (dR_z)^2. \tag{21.6}$$

21.2 Straight wire field

First we recover the original result of Biot and Savart for an infinitely long wire along the z- axis. In this case we have simply

$$\hat{e}(s) = \hat{e}_z, \quad \vec{R}(s) = s\hat{e}_z. \tag{21.7a,b}$$

Eqn. (21.4) becomes

$$\vec{B} = \frac{\mu_0 I}{4\pi}\hat{e}_z x\vec{r}\int_{-\infty}^{+\infty} ds \frac{1}{\sqrt{r^2 + (z-s)^2}^3}\ , \tag{21.8}$$

where as usual $r^2 = x^2 + y^2$. The integration is elementary in this case:

$$\vec{B} = \frac{\mu_0 I}{4\pi}\frac{\hat{e}_z x\vec{r}}{r^2}\frac{(s-z)}{\sqrt{r^2 + (s-z)^2}}\Bigg|_{-\infty}^{+\infty} = \frac{\mu_0 I}{2\pi}\frac{\hat{e}_z x\vec{r}}{r^2} = \frac{\mu_0 I}{2\pi r}\hat{e}_\theta\ . \tag{21.9}$$

For a semi-infinite wire running from $-\infty$ to 0 we have

$$\vec{B} = \frac{\mu_0 I}{4\pi}\frac{\hat{e}_\theta}{r}\left(1 - \frac{z}{\sqrt{r^2 + z^2}}\right), \tag{21.10}$$

reminiscent of the on-axis field of the semi-infinite thin-layer solenoid treated in section 4. However in this case there must be an additional current path (unspecified here) leading away from the wire end at $z = 0$ to avoid a non-zero divergence of $\vec{J}$.

A useful generalization of the above example is a straight wire segment between arbitrary points $\vec{r}_1$ and $\vec{r}_2$; we define

$$\vec{C} = \frac{\vec{r}_1 + \vec{r}_2}{2} = \text{wire center}, \tag{21.11a}$$

$$L = \left|\vec{r}_2 - \vec{r}_1\right| = \text{wire length,} \tag{21.11b}$$

$$\hat{e} = \frac{\vec{r}_2 - \vec{r}_1}{L} = \text{wire direction.} \tag{21.11c}$$

Then the wire path is

$$\vec{R}(s) = \vec{C} + s\hat{e} \ , \tag{21.11d}$$

with $-L/2 < s < L/2$. Eqn. (21.4) becomes

$$\vec{B} = \frac{\mu_0 I}{4\pi}\int_{-L/2}^{L/2} ds \ \ \hat{e}x\frac{\left[\vec{r} - \left(\vec{C} + s\hat{e}\right)\right]}{\left|\vec{r} - \left(\vec{C} + s\hat{e}\right)\right|^3} \ . \tag{21.12}$$

The integration is again elementary, but it helps to employ the definitions

$$\alpha = \hat{e}\cdot\left(\vec{r} - \vec{C}\right) \ , \ \ \vec{\beta} = \hat{e}x\left(\vec{r} - \vec{C}\right) , \tag{21.13}$$

with $\left|\vec{r} - \vec{C}\right|^2 = \alpha^2 + \left|\vec{\beta}\right|^2$. Making the change of variable $t = s - \alpha$, we get from eqn. (21.12)

$$\begin{aligned}\vec{B} &= \frac{\mu_0 I}{4\pi}\frac{\vec{\beta}}{\left|\vec{\beta}\right|^2}\frac{t}{\sqrt{\left|\vec{\beta}\right|^2 + t^2}}\Bigg|_{-L/2-\alpha}^{L/2-\alpha} \\ &= \frac{\mu_0 I}{4\pi}\frac{\vec{\beta}}{\left|\vec{\beta}\right|^2}\left[\frac{\left(L/2-\alpha\right)}{\sqrt{\left|\vec{\beta}\right|^2 + \left(L/2-\alpha\right)^2}} + \frac{L/2+\alpha}{\sqrt{\left|\vec{\beta}\right|^2 + \left(L/2+\alpha\right)^2}}\right] .\end{aligned} \tag{21.14}$$

This formula may be used for the field from a straight magnet lead. Also, the field of a complete circuit with curved wired sections can be computed as the sum of fields from short straight sections, each with specified endpoints and defined quantities $\left(\vec{C}, L, \hat{e}, \alpha, \vec{\beta}\right)$.

21.3 Helix field

The path representation of a helix is more complicated; let ρ be its radius (wire distance from z-axis), p is the helix pitch angle restricted to $\left(0 < p < \pi/2\right)$, and τ is a variable proportional to s such that $0 \le \tau \le 2\pi$ gives one loop. Then we may write

$$R_x = \rho\cos(\tau),\ \ R_y = \rho\sin(\tau),\ \ R_z = \rho\tau\tan(p). \tag{21.15}$$

We have $(ds)^2 = \left|d\vec{R}\right|^2 = \rho^2\left[1+\tan^2(p)\right](d\tau)^2$, so we set

$$\tau = \frac{s}{\rho\sqrt{1+\tan^2(p)}} \ = \ \frac{s\ \cos(p)}{\rho}\ , \tag{21.16}$$

and $R_z = s\ \sin(P)$, as expected from the definition of P.

The helix period length is $2\pi\rho\tan(p) = 1/N$, where N is the number of turns per meter, so the mean θ-component of surface current density is

$$\langle S\rangle = NI\ , \tag{21.17}$$

while the total z-current equals I.

For an infinitely long helix, the on-axis z component of the field is by symmetry

$$B_0(z) = \mu_0\langle S\rangle = \mu_0 NI. \tag{21.18}$$

For $r >> \rho$ we also have

$$B_\theta \to \frac{\mu_0 I}{2\pi r}. \tag{21.19}$$

Close to the wire, which has infinitesimal thickness, the field diverges strongly. The on-axis transverse field does not vanish, but has a constant absolute value with direction rotating 90° out of phase from the wire path. It is an interesting exercise to visualize the field lines.

To proceed with the helix field calculation, first note that

$$\hat{e}(s) = \frac{d\vec{R}}{ds} = \frac{d\tau}{ds}\frac{d\vec{R}}{d\tau} = \cos(p)\left[-\hat{e}_x \sin(\tau) + \hat{e}_y \cos(\tau) + \hat{e}_z \tan(p)\right] ,$$

$$\hat{e}(s)x\left(\vec{r} - \vec{R}(s)\right) = \cos(p)\left\{\hat{e}_x\left[(z - R_z)\cos(\tau) - (y - R_y)\tan(p)\right]\right.$$
$$\left.+\hat{e}_y\left[(x - R_x)\tan(p) + (z - R_z)\sin(\tau)\right] - \hat{e}_z\left[(y - R_y)\sin(\tau) + (x - R_x)\cos(\tau)\right]\right\}. \quad (21.20)$$

Each Cartesian field component may be projected from eqn. (21.4); for example

$$B_z = \vec{B}\cdot\hat{e}_z = -\frac{\mu_0 I}{4\pi}\int ds \frac{\cos(p)\left[(y - R_y)\sin(\tau) + (x - R_x)\cos(\tau)\right]}{\sqrt{(x - R_x)^2 + (y - R_y)^2 + (z - R_z)^2}^3} \quad . \quad (21.21)$$

This may be evaluated by a numerical integration package, using the given definitions of $\vec{R}(s)$. It helps to use $\tau = s\ \cos(p)/\rho$ as the integration variable. A helix might have for example m periods with $0 \le \tau \le 2\pi m$ and longitudinal dimension running from z=0 to z= $2\pi m\rho\tan(p)$. The components B_x and B_y are found in similar fashion.

For an infinite helix the on-axis longitudinal field is

$$B_{zo} = \frac{\mu_0 I}{4\pi}\cos(p)\int_{-\infty}^{+\infty} ds \frac{\left[R_y \sin(\tau) + R_x \cos(\tau)\right]}{\sqrt{R_x^2 + R_y^2 + (z - R_z)^2}^3} \quad (21.22)$$

$$= \frac{\mu_0 I}{4\pi}\cos(p)\int_{-\infty}^{+\infty} \frac{du}{\sin(p)} \frac{\rho}{\sqrt{\rho^2 + u^2}^3} , \quad (21.23)$$

where $u = R_z - z = s\ \sin(p) - z$. The integration is elementary:

$$B_{z_o} = \frac{\mu_0 I\rho}{4\pi\ \tan(p)}\frac{1}{\rho^2}\frac{u}{\sqrt{\rho^2 + u^2}}\Bigg|_{-\infty}^{+\infty} = \frac{\mu_0 I}{2\pi\rho\ \tan(p)} = \mu_0 NI , \quad (21.24)$$

as advertised in eqn. (21.18).

The transverse fields of a finite or infinite helix are

$$B_x = \vec{B}\cdot\hat{e}_x = \frac{\mu_0 I}{4\pi}\int ds\ \frac{\cos(p)\left[(z-R_z)\cos(\tau)-(y-R_y)\tan(p)\right]}{\sqrt{(x-R_x)^2+(y-R_y)^2+(z-R_z)^2}^3}, \tag{21.25}$$

$$B_y = \vec{B}\cdot\hat{e}_y = \frac{\mu_0 I}{4\pi}\int ds\ \frac{\cos(p)\left[(x-R_x)\tan(p)+(z-R_z)\sin(\tau)\right]}{\sqrt{(x-R_x)^2+(y-R_y)^2+(z-R_z)^2}^3}. \tag{21.26}$$

These components may also be evaluated numerically using τ as the variable of integration.

The on-axis transverse fields for an infinite helix are

$$B_{xo} = \frac{\mu_0 I\cos(p)}{4\pi}\int_{-\infty}^{+\infty} ds\ \frac{\left[\rho\sin(\tau)\tan(p)+(z-\tau\rho\tan(p))\cos(\tau)\right]}{\sqrt{\rho^2+(z-\tau\rho\tan(p))^2}^3}, \tag{21.27}$$

$$B_{yo} = \frac{\mu_0 I\cos(p)}{4\pi}\int_{-\infty}^{+\infty} ds\ \frac{\left[(z-\tau\rho\tan(p))\sin(\tau)-\rho\cos(\tau)\tan(p)\right]}{\sqrt{\rho^2+(z-\tau\rho\tan(p))^2}^3}. \tag{21.28}$$

Making the change of variable $u = R_z - z = s\ \sin(p) - z$ we get

$$B_{xo} = \frac{\mu_0 I}{4\pi\ \tan(p)}\int_{-\infty}^{+\infty} du\frac{\left[\rho\tan(p)\sin\left(\frac{u+z}{\rho\ \tan(p)}\right)-u\cos\left(\frac{u+z}{\rho\ \tan(p)}\right)\right]}{\sqrt{\rho^2+u^2}^3}, \tag{21.29}$$

$$B_{yo} = \frac{-\mu_0 I}{4\pi\ \tan(p)}\int_{-\infty}^{+\infty} du\frac{\left[u\sin\left(\frac{u+z}{\rho\tan(p)}\right)+\rho\tan(p)\cos\left(\frac{u+z}{\rho\tan(p)}\right)\right]}{\sqrt{\rho^2+u^2}^3}. \tag{21.30}$$

It is seen that B_{x_0} vanishes at $z = 0$, $\pm\pi\rho\ \tan(p)$, $\pm 2\pi\rho\ \tan(p)$, … , consistent with the helical symmetry. At the coordinate origin we have, setting $u = \rho\upsilon$,

$$B_{y_0}(0) = -\frac{\mu_0 I}{2\pi\rho\ \tan(p)} \int_0^\infty d\upsilon \left[\frac{\upsilon \sin\left(\frac{\upsilon}{\tan(p)}\right)}{\sqrt{1+\upsilon^2}^3} + \frac{\tan(p)\cos\left(\frac{\upsilon}{\tan(p)}\right)}{\sqrt{1+\upsilon^2}^3} \right] \tag{21.31}$$

$$= -\frac{\mu_0 I}{2\pi\rho\ \tan(p)} \left[\frac{\mathrm{K}_0\left(1/\tan(p)\right)}{\tan(p)} + \mathrm{K}_1\left(1/\tan(p)\right) \right] , \tag{21.32}$$

where K_0 and K_1 are the modified Bessel functions. Setting $1/\tan(p) = 2\pi\rho N$ we have

$$B_{y_0}(0) = -\mu_0 IN\left[(2\pi\rho N)\mathrm{K}_0(2\pi\rho N) + \mathrm{K}_1(2\pi\rho N) \right] . \tag{21.33}$$

Invoking periodicity yields

$$\vec{B}_{\perp_0} = B_{y_0}(0)\left[\hat{e}_y\ \cos(\tau) - \hat{e}_x\ \sin(\tau) \right] . \tag{21.34}$$

Generally the parameter $2\pi\rho N$ is much larger that unity, and the Bessel functions may be expanded; the leading terms gives

$$B_{y_0}(0) \approx -(\mu_0 IN)\sqrt{\frac{\pi}{2}}\left(\sqrt{2\pi\rho N} + \frac{7}{8\sqrt{2\pi\rho N}} \right) e^{-2\pi\rho N} , \tag{21.35}$$

which is usually a very small on-axis effect. For an concrete example set $(N = 20\,\mathrm{turn/m},\ \rho = .1\mathrm{m})$, then $2\pi\rho N = 12.566$, and

$$\frac{B_{y_0}(0)}{-\mu_0 IN} \approx \sqrt{\frac{\pi}{2}}\left(\sqrt{12.566} + \frac{7}{8\sqrt{12.566}} \right) e^{-12.566} \cong .000017 . \tag{21.36}$$

22. Single Particle Equations of Motion in an Arbitrary Electromagnetic Field

Although the topic of this report is the calculation of fields, we also include this brief section on the particle equations of motion. The goal is to have a convenient reference where these equations are written using longitudinal distance z as the independent variable instead of time t. This form displays the geometric aberrations, which are mixed with field aberrations and are hidden in the more compact time-dependent formulation.

22.1 Time as the independent variable

With time as the independent variable, an ion's velocity $\vec{v}$ satisfies the Lorentz equation

$$\frac{d\left(\gamma\vec{v}\right)}{dt} = \frac{qe}{M}\left(\vec{E} + \vec{v}x\vec{B}\right), \tag{22.1}$$

with relativistic factor

$$\gamma = \left(1 - v^2/c^2\right)^{-1/2} = \left(1 + \gamma^2 v^2/c^2\right)^{1/2} . \tag{22.2}$$

Here q is the ion's charge state, M is its mass, $v = \left|\vec{v}\right|$, and we use the natural constants

$$e = 1.6022...x10^{-19} C, \;\; c = 2.9979...x10^{8}\, m/s .$$

The electric and magnetic fields, $\vec{E}\left(\vec{r},t\right)$ and $\vec{B}\left(\vec{r},t\right)$, are assumed to be known or are computable.

22.2 Longitudinal distance as the independent variable

For time-dependent, multi-particle simulations it is convenient to use eqn. (22.1) as it stands, or with $\gamma = 1$ for non-relativistic cases. However there are situations where it is preferable to use the longitudinal position z as the independent variable. One example is the simulation of an ion source operating in steady state. In principle we may always use z instead of t if there is no turning back of ion orbits. In addition to the particle variables $\left\{x(z), y(z), v_x(z), v_y(z), v_z(z), v(z), \gamma(z)\right\}$ we also calculate $t(z)$, the time when an ion is at z. The fields the ion experiences are then

$$\vec{B} = \vec{B}\left(\vec{r}(z), t(z)\right), \qquad \vec{E} = \vec{E}\left(\vec{r}(z), t(z)\right). \tag{22.3a,b}$$

The time derivative in eqn. (22.1) is converted to a z-derivative by the relation

$$\frac{d}{dt} = v_z \frac{d}{dz} . \tag{22.4}$$

Derivatives with respect to z are denoted here by a "prime", i.e. $x'(z) = dx/dz$, etc. Then we get

$$v_x = \frac{dx}{dt} = v_z \frac{dx}{dz} = v_z x', \qquad v_y = \frac{dy}{dt} = v_z \frac{dy}{dz} = v_z y'. \tag{22.5a,b}$$

The absolute velocity is

$$v(z) = \sqrt{v_x^2 + v_y^2 + v_z^2}, \tag{22.6}$$

so substituting from eqn. (22.5) (assuming $v_z > 0$):

$$v_z = \frac{v(z)}{\sqrt{1 + x'^2 + y'^2}} \ . \tag{22.7}$$

The time derivative may therefore be written

$$\frac{d}{dt} = \frac{v(z)}{\sqrt{1 + x'^2 + y'^2}} \frac{d}{dz} \ . \tag{22.8}$$

The factor $\sqrt{1 + x'^2 + y'^2}$ in eqns. (22.7, 22.8), which we will denote by $\sqrt{...}$, is the cause of the geometric aberrations for transport close to the z axis.

Eliminating time, eqn. (20.1) yields

$$\frac{v}{\sqrt{...}} \frac{d}{dz} \frac{\gamma v}{\sqrt{...}} \frac{dx}{dz} = \frac{qe}{M} \left(E_x + \frac{v y'}{\sqrt{...}} B_z - \frac{v}{\sqrt{...}} B_y \right) \ , \qquad \frac{v}{\sqrt{...}} \frac{d}{dz} \frac{\gamma v}{\sqrt{...}} \frac{dy}{dz} = \frac{qe}{M} \left(E_y + \frac{v}{\sqrt{...}} B_x - \frac{v x'}{\sqrt{...}} B_z \right) \ . \tag{22.9a,b}$$

We also need an equation for γ (or equivalently v or γv). From eqns. (22.1) and (22.2) we derive

$$\frac{d}{dt} \gamma = \frac{qe}{Mc^2} \vec{v} \cdot \vec{E}, \tag{22.10}$$

which becomes

$$\frac{d\gamma}{dz} = \frac{qe}{Mc^2} \left(x' E_x + y' E_y + E_z \right) \ , \tag{22.11a}$$

or equivalently

$$\frac{dv}{dz} = \frac{qe}{M}\frac{1}{\gamma^3 v}\left(x'E_x + y'E_y + E_z\right) \ ,$$
$$\frac{d\gamma v}{dz} = \frac{qe}{M}\frac{1}{v}\left(x'E_x + y'E_y + E_z\right) \ . \qquad (22.11b,c)$$

The equation for time is simply

$$\frac{dt}{dz} = \frac{1}{v_z} = \frac{\sqrt{...}}{v} \ . \qquad (22.12)$$

Eqns. (22.9a.b) are of an awkward form since, due to the differentiation of $\sqrt{...}$, the second derivatives x'' and y'' appear together. A simplification is realized when these equations are combined linearly to place these second derivatives in separate equations. It also helps to eliminate $d(\gamma v)/dz$ using eqn. (22.11c). These steps finally yield after some algebra:

$$x'' = \frac{qe}{M}\frac{1}{\gamma v^2}\left\{\sqrt{...}^2\left(E_x - x'E_z\right) + v\sqrt{...}\left[x'y'B_x - \left(1 + x'^2\right)B_y + y'B_z\right]\right\}, \quad (22.13a)$$

$$y'' = \frac{qe}{M}\frac{1}{\gamma v^2}\left\{\sqrt{...}^2\left(E_y - y'E_z\right) + v\sqrt{...}\left[-x'y'B_y + \left(1 + y'^2\right)B_x - x'B_z\right]\right\}. \quad (22.13b)$$

Eqns. (22.11), (22.12), and (22.13) are valid as long as $dz/dt > 0$; they contain all aberrations and may be used with tilted system axes and non-solenoidal fields.

22.3 Paraxial approximation

Often a set of equations is used, in which terms such as x'^2 are known to be small and are dropped. This is the "paraxial approximation", with formal ordering $d/dz \sim \varepsilon << 1$ and $(x, y) \sim 1$:

$$\frac{qe}{M}\frac{1}{\gamma v^2}\left(E_z, vB_z\right) \sim \varepsilon \ , \qquad (22.14)$$

$$\frac{qe}{M}\frac{1}{\gamma v^2}\left(E_x, E_y, vB_x, vB_y\right) \sim \varepsilon^2 \ . \qquad (22.15)$$

Dropping terms which are explicitly small of order ε^2, gives

$$c^2 \frac{d\gamma}{dz} = \gamma^3 v \frac{dv}{dz} = v \frac{d\gamma v}{dz} = \frac{qe}{M} \mathrm{E}_z \,, \tag{22.16}$$

$$\frac{dt}{dz} = \frac{1}{v} \,, \tag{22.17}$$

$$x'' = \frac{qe}{M} \frac{1}{\gamma v^2} \left[\left(\mathrm{E}_x - x' \mathrm{E}_z \right) + v \left(y' B_z - B_y \right) \right] , \tag{22.18a}$$

$$y'' = \frac{qe}{M} \frac{1}{\gamma v^2} \left[\left(\mathrm{E}_y - y' \mathrm{E}_z \right) - v \left(x' B_z - B_x \right) \right] . \tag{22.18b}$$

Field aberrations are still present in eqns. (22.16, 22-17, 22.18) and these include terms, which are small in powers of ε, so the paraxial approximation by itself is not a consistent ordering.